Extensions to the characteristic basis function method, for antenna array analysis

by

Keshav Sewraj

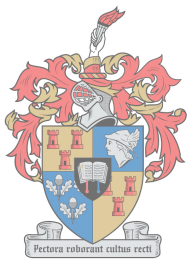

Thesis presented in partial fulfilment of the requirements for the degree of Master of Engineering (Electronic) in the Faculty of Engineering at Stellenbosch University

Supervisor: Prof. M. M. Botha

March 2018

Declaration

By submitting this thesis electronically, I declare that the entirety of the work contained therein is my own, original work, that I am the sole author thereof (save to the extent explicitly otherwise stated), that reproduction and publication thereof by Stellenbosch University will not infringe any third party rights and that I have not previously in its entirety or in part submitted it for obtaining any qualification.

Date: March 2018

Abstract

Extensions to the characteristic basis function method, for antenna array analysis

K. Sewraj

Department of Electrical and Electronic Engineering,
University of Stellenbosch,
Private Bag X1, Matieland 7602, South Africa.

Thesis: MEng (Elec)

December 2017

The focus of this work is to solve for the electromagnetic problem of large linear antenna arrays efficiently and accurately within the context of two-dimensional (2D), transverse magnetic (TM) Method of Moments (MoM). Provided that the meshing size is small enough, the MoM can provide accurate results for electromagnetic simulations. However, the memory storage and computational time scale as $\mathcal{O}(N^2)$ and $\mathcal{O}(N^3)$ respectively, where N is the number of basis functions. The electrical size solvable with given computational resources is therefore limited. To analyze large antenna arrays, the Characteristic Basis Function Method (CBFM) is employed. This technique decomposes the entire geometry into subdomains, over which, physics-based macro basis functions called CBFs are defined. By using macro basis functions, the aim is to define the same electromagnetic problem using fewer degrees of freedom as compared to the standard MoM. Firstly, a CBFM code where a subdomain is defined to be an antenna element is implemented. The results of CBFM using up to quaternary CBFs (higher-order CBFs) are compared to that of the MoM. Secondly, CBFM with larger overlapping subdomains which span multiple antenna elements in an array is defined, so as the mutual coupling in dense antenna arrays is better represented. To generate higher-order CBFs, the distance-based criterion is proposed which is found to be a more efficient procedure than the conventional tree-based approach, for larger subdomain CBFM. The results for larger subdomain CBFM including the distance-based criterion are compared to the conventional single antenna subdomain CBFM over a range of frequencies.

Opsomming

Uitbreidings tot die karakteristieke basisfunksie metode, vir antenna samestelling analise

K. Sewraj

Departement van Elektriese en Elektroniese Ingenieurswese,
Universiteit van Stellenbosch,
Privaat Sak X1, Matieland 7602, Suid-Afrika.

Tesis: MIng (Elek)

Desember 2017

Die fokus van hierdie werk is om die elektromagnetiese probleem van groot, liniêre antenna samestellings effektief en akkuraat op te los, binne die konteks van die tweedimensionele (2D), transversaal-magnetiese (TM) Moment Metode (MoM). Indien die maas-grootte klein genoeg is, dan lewer die MoM akkurate elektromagnetiese simulasie resultate, maar die rekenaargeheue en berekeningstyd skaleer as $\mathcal{O}(N^2)$ en $\mathcal{O}(N^3)$, onderskeidelik, waar N die aantal basisfunksies verteenwoordig. Die oplosbare elektriese grootte met gegewe rekenaarkrag, is dus beperk. Die Karakteristieke Basisfunksie Metode (KBFM) word gebruik om groot antenna samestellings te analiseer. Hierdie tegniek breek die geometrie op in sub-strukture, waaroor fisies-gefundeerde makro basisfunksies genaamd KBFs, gedefinieer word. Die doel van makro basisfunksies is om die gegewe elektromagnetiese probleem se oplossing met minder vryheidsgrade voor te stel, in vergelyking met die standaard MoM. 'n KBFM kode waar die sub-strukture ooreenstem met die antenna elemente, is eerstens geïmplementeer. KBFM resultate met tot vierde-orde KBFs word vergelyk met die MoM. Tweedens word die KBFM met groter, oorvleuelende sub-strukture wat oor verskeie antenna elemente strek, gedefinieer, sodat wedersydse koppeling in digte antenna samestellings beter in ag geneem word. Om hoër-orde KBFs te skep, word 'n afstand-gebaseerde kriterium voorgestel, en daar word bepaal dat dit 'n meer effektiewe prosedure is as die konvensionele boomstruktuur gebaseerde benadering, vir groter sub-struktuur KBFM. Resultate vir groter sub-struktuur KBFM met afstand-gebaseerde kriterium, word vergelyk met die konvensionele, enkel-antenna sub-struktuur KBFM, oor 'n wye frekwensiebereik.

Acknowledgements

I am grateful to my supervisor, Prof. Matthys Botha, for his support and guidance throughout my master's degree at Stellenbosch University and for his contribution to my education. During the last two years, I have had the opportunity to learn from his expertise in computational electromagnetics, and also to enhance my research skills. Prof. Botha has made himself available to helping me at every stage of this thesis and also reviewing the draft of this document.

I would like to thank all colleagues at the Radar Lab for the very pleasant and supportive working environment.

My deepest gratitude goes towards my parents who have been extremely supportive at every step in my life and for giving much importance to my education and well-being. I would also like to thank my sister, Deeya, for all her support, advice, guidance and friendship since childhood. My aunty (Poupou), Neelam, who has spent countless afternoons and Sundays helping me with mathematics and sciences during my school days. To all my friends and teachers who have had a positive contribution to my betterment, thank you. To my cousin, Shyamal, who is no longer among us. Thank you for your friendship and time spent together, you are being missed.

Finally, I would like to thank the Square Kilometre Array (SKA) – South Africa (SA) for their financial support during my master's thesis and giving me the opportunity to work on this interesting project.

Dedications

This thesis is dedicated to my parents.

Contents

List of Figures

List of Tables

Nomenclature

Constants

$\epsilon_0 \approx$	$8.854 \times 10^{-12}\,\mathrm{F/m}$
$\mu_0 =$	$4\pi \times 10^{-7}\,\mathrm{H/m}$

Vectors, Scalars and Symbols

$\boldsymbol{E}$	Electric field intensity
$\boldsymbol{H}$	Magnetic field intensity
$\boldsymbol{D}$	Electric flux density
$\boldsymbol{B}$	Magnetic flux density
$\boldsymbol{J}$	Electric current density
$\boldsymbol{A}$	Magnetic vector potential
q_e	Electric charge density
ϕ_e	Electric scalar potential
$\hat{x}$	Unit vector
∇	Delta operator
x, y, z	Cartesian coordinates
j	Unit imaginary number
$\boldsymbol{r}, \boldsymbol{r}'$	Position vectors in 3D space
$\boldsymbol{\rho}, \boldsymbol{\rho}'$	Position vectors in 2D space
$\langle \cdot \rangle$	Inner product
δ	Dirac delta function
$\in$	Element of

Abbreviations

2D	Two-Dimensional
3D	Three-Dimensional
CBFM	Characteristic Basis Function Method
EFIE	Electric Field Integral Equation
FDTD	Finite Difference Time Domain
FEM	Finite Element Method
MBF	Macro Basis Function
MFAA	Mid Frequency Aperture Array
MFIE	Magnetic Field Integral Equation
MLFMM	Multilevel Fast Multipole Method
MoM	Method of Moments
PEC	Perfect Electric Conductor
SED	Sub Entire Domain
SFX	Synthetic-Function Approach
SKA	Square Kilometre Array
SVD	Singular Value Decomposition
TE	Transverse Electric
TM	Transverse Magnetic

Chapter 1

Introduction

1.1 Motivation

The accidental discovery of cosmic radio signals [1] by Karl Jansky in 1932 began the era of radio astronomy. Since then, every major step in astronomical instrumentation has opened new doors for scientific discoveries. There is a constant urge to built more sensitive radio telescopes to have a more detailed view of the sky. An increased sensitivity can be achieved either by using larger reflectors, which becomes impractical after a certain size or by using interferometry techniques [2]. For this reason, the Square Kilometre Array (SKA) [3] project is currently being built in South Africa and Western Australia. A large number of antennas will be built which can be connected through interferometry to act as one large radio telescope. For mid-range frequency radio astronomy, 400MHz to 1500MHz, dense antenna aperture array consisting of complex shaped antennas, namely the Mid Frequency Aperture Array (MFAA) [4] will be built.

To meet the specifications during the antenna array design process, it is of utmost importance to have a good understanding of the surface current distribution over the antenna elements. Since no analytical formulation is available for complex geometries, there is the need to develop accurate and efficient numerical electromagnetic solvers.

1.2 Numerical Electromagnetic Solvers

The Method of Moments [5, 6] is a full wave integral equation technique used to solve radiation problems. An integral equation based solver is suitable for solving antenna (including antenna array) problems since the field at any point in space can be computed once the surface current is available. Moreover, unlike differential equation solvers, such as the Finite Element Method (FEM) [7] or the Finite Difference Time Domain (FDTD) method [8], MoM only requires surface discretization, which is valid for metallic structures as in this study. However, one major drawback is the need to invert a fully populated impedance matrix, which grows very rapidly with the electrical size of the geometry. Thus, direct application of the MoM is computationally very expensive both in terms of memory storage and computational time for the modeling of extremely large arrays such as the MFAA.

Fast algorithms based on the MoM need to be developed in order to reduce the computational burden. In this thesis, the Macro Basis Function (MBF) [9] class of techniques, more specifically, the Characteristic Basis Function Method (CBFM) [10] is considered to reduce the computational burden for large arrays. The CBFM is a 'divide and conquer' approach where the entire geometry is divided into subdomains. Higher-order physics based functions, called Characteristic Basis Functions (CBFs), are defined over each subdomain. The aim is to use fewer degrees of freedom to define the same electromagnetic problem. In literature, variants of MBFs have been applied to analyze large arrays for radio astronomy purposes, for instance in [11, 12].

1.3 Stages of the Research Work

This research work towards a memory efficient solver for linear antenna arrays consisted of various tasks, namely

- Firstly, a two-dimensional (2D), transverse magnetic (TM) MoM solver is implemented for a linear antenna array.
- A CBFM routine is then implemented to improve the computational cost of the solver. A subdomain is considered as an antenna element in the array.
- A generalized CBFM routine is proposed and implemented where larger overlapping subdomains are defined, with distance-based criterion to generate higher-order CBFs.

When dense antenna arrays are considered, a large number of higher-order CBFs in conventional CBFM is required to model accurately the effect due to mutual coupling among antenna elements. The use of a high number of CBFs prevents the compression of the impedance matrix as desired. Thus, by defining larger overlapping CBFs, the effect of mutual coupling is better incorporated, leading to a further reduction in the number of degrees of freedom for similar accuracy.

1.4 Outline of Thesis

A brief outline of the rest of this thesis is as follows:

Chapter 2: Electromagnetic equations which are essential to the Method of Moments are discussed. The Electric Field Integral Equation (EFIE) for the 2D, TM case is derived.

Chapter 3: The EFIE is discretized and the MoM matrix equation is formulated. The choices for basis and testing function, and numerical integration scheme used in the MoM solver are discussed. Results from the MoM solver are compared to that of the commercial EM software, FEKO [13].

Chapter 4: The background and formulation of the CBFM are discussed. Results of the CBFM using up to quaternary CBFs is presented and compared to the MoM results.

Chapter 5: CBFs are defined over larger overlapping subdomain. Motivations for the choice of larger subdomains are discussed. Results with larger subdomain CBFM are compared to those with single antenna subdomains.

Chapter 6: A distance-based criterion to generate higher order CBFs is introduced, and results are compared to the conventional tree structure for the generation of CBFs.

Chapter 7: Results from the different methods explored throughout this thesis are compared to both the case of linear antenna arrays in the 2D context.

Chapter 8: Conclusions are drawn, and further possible research avenues are discussed.

Chapter 2

Electromagnetic Field Theory

2.1 Introduction

In this chapter, a brief description regarding the background of electromagnetic theory relevant to this thesis is given. Beginning with Maxwell's set of equations for electromagnetism together with the equations for the electromagnetic boundary conditions, the electric field integral equation (EFIE) is derived. The numerical technique, the Method of Moments (MoM), which is used to solve for radiation problems in this thesis, is obtained after the discretization of the EFIE. Since this work is based on two-dimension (2D) MoM, the formulation of 2D, transverse magnetic (TM), EFIE is derived. In this chapter, only Perfect Electric Conductor (PEC) objects in free space are considered.

2.2 Maxwell's Equations in Frequency Domain

Electromagnetic phenomena are governed by Maxwell's set of equations, which describes the generation and interaction between electric and magnetic field. Maxwell's equations in the frequency domain [14] for free-space are given as in (2.1) to (2.4).

$$\nabla \times \boldsymbol{E} = -j\omega\mu_0 \boldsymbol{H} \tag{2.1}$$
$$\nabla \times \boldsymbol{H} = \boldsymbol{J} + j\omega\epsilon_0 \boldsymbol{E} \tag{2.2}$$
$$\nabla \cdot \boldsymbol{D} = q_e \tag{2.3}$$
$$\nabla \cdot \boldsymbol{B} = 0 \tag{2.4}$$

The field quantities, $\boldsymbol{E}$, $\boldsymbol{H}$, $\boldsymbol{D}$, $\boldsymbol{B}$, $\boldsymbol{J}$ and q_e are assumed to be time-varying throughout the text. The field quantities are phasors, and their time dependence, $e^{j\omega t}$, is omitted for simplicity. The definitions of the field quantities in (2.1) to (2.4) are listed in the nomenclature.

The electric and magnetic field constitutive relations for free space are given in (2.5) and (2.6) respectively.

$$\boldsymbol{D} = \epsilon_0 \boldsymbol{E} \tag{2.5}$$
$$\boldsymbol{B} = \mu_0 \boldsymbol{H}, \tag{2.6}$$

where ϵ_0 and μ_0 throughout denote the free space electric permittivity and magnetic permeability respectively.

2.3 Boundary Conditions at an Interface between PEC and Free Space

Boundary conditions describe how electromagnetic fields behave at interfaces between regions of different dielectric parameters, be it dielectrics, free space or PEC. Boundary conditions (in addition to radiation conditions) are required so as Maxwell's set of equations has a unique solution in order construct the EFIE. Equations (2.7) to (2.10) describe the boundary condition between a PEC region and on the free space side.

$$-\hat{n} \times \boldsymbol{E} = 0 \tag{2.7}$$
$$\hat{n} \times \boldsymbol{H} = \boldsymbol{J}_s \tag{2.8}$$
$$\hat{n} \cdot \boldsymbol{D} = q_e \tag{2.9}$$
$$\hat{n} \cdot \boldsymbol{B} = 0 \tag{2.10}$$

where $\boldsymbol{J}_s$ is the electric surface current and $\hat{n}$ is the normal vector at the interface pointing into the free space region. Equations (2.7) to (2.10) have high importance since the metallic surfaces are regarded to be a PEC in the formulation of the integral equation for the Method of Moments.

2.4 Vector Wave Equation

The EFIE can be formulated by directly using the wave equation (A.4) as derived in Appendix A which relates the electric field intensity, $\boldsymbol{E}$, to the surface current density, $\boldsymbol{J}$, or indirectly by using the magnetic vector potential as intermediate [14]. The latter is often preferred due to a simpler integration process, and thus, this is the approach considered to derive the EFIE in this thesis.

Since the magnetic flux density, $\boldsymbol{B}$, is solenoidal, that is, $\nabla \cdot \boldsymbol{B} = 0$, it can be represented by the following vector identity

$$\nabla \cdot (\nabla \times \boldsymbol{A}) = 0. \tag{2.11}$$

$\boldsymbol{A}$ is referred to as the **magnetic vector potential**. By substituting $\boldsymbol{H} = \frac{1}{\mu_0}\boldsymbol{B}$ (from (2.6)) in Faraday's law (2.1), and then replacing $\boldsymbol{B}$ by the curl of the vector magnetic potential, $\boldsymbol{A}$, as in (2.11), we obtain

$$\nabla \times \boldsymbol{E} = -j\omega\mu_0\boldsymbol{H} = -j\omega\nabla \times \boldsymbol{A}. \tag{2.12}$$

Rearranging (2.12) gives

$$\nabla \times (\boldsymbol{E} + j\omega\mathbf{A}) = 0. \tag{2.13}$$

Since a curl-free vector field can be represented as the gradient of a scalar field, we can write

$$\boldsymbol{E} + j\omega\boldsymbol{A} = -\nabla\phi_e \tag{2.14}$$

where ϕ_e is a scalar referred to as the **electric scalar potential**. Electric field intensity, $\boldsymbol{E}$, can thus be expressed using the scalar electric potential, ϕ_e, and vector magnetic potential, $\boldsymbol{A}$, as

$$\boldsymbol{E} = -\nabla\phi_e - j\omega\boldsymbol{A} \tag{2.15}$$

Since only the curl of $\boldsymbol{A}$ is defined so far, we are free to define the divergence of $\boldsymbol{A}$. To simplify, the *Lorenz gauge condition* is used, that is

$$\nabla \cdot \boldsymbol{A} = j\omega\epsilon_0\mu_0\phi_e. \tag{2.16}$$

The relationship between the electric field intensity, $\boldsymbol{E}$ and magnetic vector potential, $\boldsymbol{A}$ is obtained by substituting ϕ_e from (2.16) into (2.15), leading to

$$\boldsymbol{E} = -j\omega\boldsymbol{A} - j\frac{1}{\omega\epsilon_0\mu_0}\nabla(\nabla \cdot \boldsymbol{A}) \tag{2.17}$$

By taking the curl on both side of $\mu_0\boldsymbol{H} = \nabla \times \boldsymbol{A}$ (from (2.12)) and using the vector identity in (2.18)

$$\nabla \times \nabla\boldsymbol{A} = \nabla(\nabla \cdot \boldsymbol{A}) - \nabla^2\boldsymbol{A}, \tag{2.18}$$

leads to (2.19)

$$\mu_0\nabla \times \boldsymbol{H} = \nabla(\nabla \cdot \boldsymbol{A}) - \nabla^2\boldsymbol{A}. \tag{2.19}$$

Equating (2.19) to Maxwell-Ampere's law (2.2), leads to

$$\mu_0\boldsymbol{J} + j\omega\mu_0\epsilon_0\boldsymbol{E} = \nabla(\nabla \cdot \boldsymbol{A}) - \nabla^2\boldsymbol{A}. \tag{2.20}$$

By substituting $\boldsymbol{E}$ in (2.20) by (2.15) and using the Lorenz gauge condition (2.16), a relation between the magnetic vector potential, $\boldsymbol{A}$, and electric current density, $\boldsymbol{J}$, is obtained as

$$\nabla^2\boldsymbol{A} + \omega^2\mu_0\epsilon_0\nabla\boldsymbol{A} = -\mu_0\boldsymbol{J}. \tag{2.21}$$

The solution to the partial differential equation (wave equation) [14] in (2.21) over a volume, V, assuming that $\boldsymbol{J}$ is an infinitesimal point, is given as

$$\boldsymbol{A} = \frac{\mu_0}{4\pi}\iiint_V \boldsymbol{J}(x', y', z')\frac{e^{-jk_0|\boldsymbol{r}-\boldsymbol{r}'|}}{|\boldsymbol{r}-\boldsymbol{r}'|}dv' \tag{2.22}$$

where, $k_0 = \omega\sqrt{\mu_0\epsilon_0}$ is the wavenumber and $\boldsymbol{r}'$ and $\boldsymbol{r}$ are the source and observer points respectively in the euclidean space. The relation between the electric field intensity, $\boldsymbol{E}$, and electric current density, $\boldsymbol{J}$, to formulate the electric field integral equation in section 2.5 is obtained by the combination of (2.17) and (2.22).

2.5 Formulation of the EFIE

Integral equations can be classified as either Magnetic Field Integral Equation (MFIE) or Electric Field Integral Equation (EFIE). EFIE can be applied to a broader application since it can be used for both open and closed surface which is not the case for MFIE [6]. For this reason, in this thesis, the EFIE has been used to formulate the MoM. In this section, the EFIE is derived using the auxiliary magnetic vector potential in the three-dimensional (3D) context for an arbitrary current distribution in free

space. The EFIE is the relation between the electric field intensity, $\boldsymbol{E}$ and the electric current density, $\boldsymbol{J}$. The unknown current density, $\boldsymbol{J}$, to be solved for is part of the integrand.

Equation (2.17) can be re-written as

$$\boldsymbol{E} = -j\frac{1}{\omega\mu_0\epsilon_0}[\omega^2\mu_0\epsilon_0\boldsymbol{A} + \nabla(\nabla\cdot\boldsymbol{A})] \tag{2.23}$$

and by substituting (2.22) into (2.23), an integral equation relating the electric field and the current density is obtained as

$$\boldsymbol{E}(\boldsymbol{r}) = -j\frac{\eta_0}{k_0}[k_0^2\iiint_V \boldsymbol{J}(\boldsymbol{r}')G(\boldsymbol{r},\boldsymbol{r}')dv' + \nabla\iiint_V \nabla'\cdot\boldsymbol{J}(\boldsymbol{r}')G(\boldsymbol{r},\boldsymbol{r}')dv'], \tag{2.24}$$

where $\eta_0 = \sqrt{\frac{\mu_0}{\epsilon_0}}$ is the intrinsic impedance and $G(\boldsymbol{r},\boldsymbol{r}')$ is the Green's function [15] for a 3D electromagnetic field and can be expressed as

$$G(\boldsymbol{r},\boldsymbol{r}') = \frac{e^{-jk_0|\boldsymbol{r}-\boldsymbol{r}'|}}{4\pi|\boldsymbol{r}-\boldsymbol{r}'|}. \tag{2.25}$$

2.6 EFIE in 2D TM Polarization

As mentioned in Chapter 1, this work is based on 2D, TM, MoM, hence the need for a 2D EFIE formulation. EFIE in 2D can be classified as Transverse Magnetic (TM) (perpendicular polarization) or Transverse Electric (TE) (parallel polarization) field [6]. The focus of this work will only be on TM polarization.

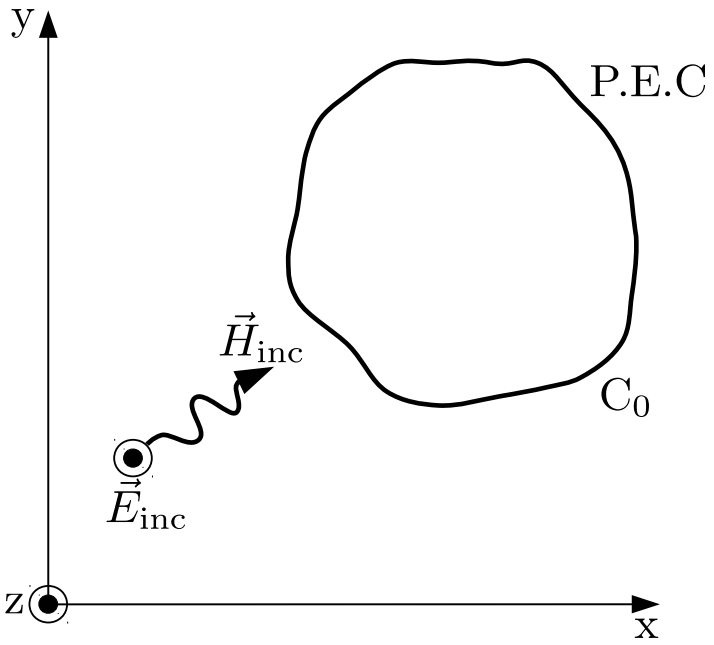

Figure 2.1: PEC Structure in xy plane.

In the 2D, TM case, a cross-section of an infinitely long (in the z-axis) PEC structure is considered in the xy plane as shown in Figure 2.1. The electric field intensity (both incident and scattered field) has only a z-component whereas the magnetic field intensity has x and y-components. Since $\boldsymbol{A}$ also only has z-component and therefore $\nabla \cdot [A_z(x,y)\hat{z}] = 0$, (2.17) is reduced to (2.26).

$$\boldsymbol{E}^{\text{total}} = -j\omega A_z \hat{z} \tag{2.26}$$

$\boldsymbol{E}^{\text{total}}$ is the sum of the incident and scattered electric field. Since the A_z is independent of z-axis variations, it can be simplified as

$$\begin{aligned} A_z &= \frac{\mu_0}{4\pi} \iiint_V J_z(\boldsymbol{r}') \frac{e^{-jk_0|\boldsymbol{r}-\boldsymbol{r}'|}}{|\boldsymbol{r}-\boldsymbol{r}'|} dv' = \frac{\mu_0}{4\pi} \iint_S J_z(\boldsymbol{\rho}') \int_\infty^\infty \frac{e^{-jk_0|\boldsymbol{r}-\boldsymbol{r}'|}}{|\boldsymbol{r}-\boldsymbol{r}'|} dz' ds' \\ &= -j\frac{\mu_0}{4} \iint_S J_z(\boldsymbol{\rho}') H_0^{(2)}(k_0|\boldsymbol{\rho}-\boldsymbol{\rho}'|) ds' \end{aligned} \tag{2.27}$$

where S is a surface over the xy plane, and $\boldsymbol{\rho}'$ and $\boldsymbol{\rho}$ are the source and observer position vectors respectively in the xy plane. $H_0^{(2)}(k_0|\boldsymbol{\rho}-\boldsymbol{\rho}'|)$ is the Green's function in 2D, TM polarization. Finally, the 2D EFIE for any observation point in the xy plane can be written as

$$E_z^{\text{total}}(\boldsymbol{\rho}) = -\frac{k_0\eta_0}{4} \iint_S J_z(\boldsymbol{\rho}') H_0^{(2)}(k_0|\boldsymbol{\rho}-\boldsymbol{\rho}'|) ds' \tag{2.28}$$

2.7 Conclusion

In this chapter, a general EFIE has been derived for any point in the 2D context from the wave equation formulated in terms of the magnetic vector potential starting from Maxwell's set of equations. The EFIE for the specialized case due to the current only on a PEC structure is presented in Chapter 3. The EFIE in 2D will be discretized to solve for radiation problems numerically using the Method of Moments in subsequent chapters.

Chapter 3

Method of Moments

3.1 Introduction

In this chapter, the theory of Method of Moments (MoM) [5] will be presented. MoM is a full wave technique to solve electromagnetic radiation and scattering problems. The MoM matrix equation can be obtained after the discretization of an integral equation. In this thesis, EFIE in 2D, TM MoM context is considered. Moreover, the implementation of the MoM solver in this work will be discussed in this chapter.

3.2 Electric Field Integral Equation

In this section, (2.28) is applied to the specialized case where the current is only present on the surface of the PEC structure. Since the tangential component of the $\boldsymbol{E}$ vanishes on the surface of a PEC, E_z^{total} can be expressed as

$$E_z^{\text{total}} = E_z^{\text{inc}} + E_z^{\text{scat}} = 0. \tag{3.1}$$

E_z^{inc} is the z-component incident electric field as shown in Figure 2.1. The incident field induces a current on the surface of the PEC structure, which in turn, creates a scattered electric field, E_z^{scat}. The scattered field at any point can be computed using the induced current as

$$E_z^{\text{scat}}(\boldsymbol{\rho}) = -\frac{k_0\eta_0}{4}\int_{C_0} J_z(\boldsymbol{\rho}')H_0^{(2)}(k_0|\boldsymbol{\rho}-\boldsymbol{\rho}'|)dc' \quad \boldsymbol{\rho}\in C_0, \tag{3.2}$$

where C_0 refers to the surface of the structure as depicted in Figure 2.1.

A relation between the incident field and surface current is desired since both the E_z^{scat} and J_z are unknowns. Substituting (3.1) into (3.2) leads to

$$E_z^{\text{inc}}(\boldsymbol{\rho}) = \frac{k_0\eta_0}{4}\int_{C_0} J_z(\boldsymbol{\rho}')H_0^{(2)}(k_0|\boldsymbol{\rho}-\boldsymbol{\rho}'|)dc' \quad \boldsymbol{\rho}\in C_0. \tag{3.3}$$

3.3 Formulation of the MoM Matrix Equation

To solve the electromagnetic problem numerically, the EFIE must be discretized to have a finite degrees of freedom. This is done by subdiving the 2D structure into

substructures called elements as in Figure 3.1. On each element, a basis function is used to approximate the induced current distribution onto that cell such that,

$$J_z(\boldsymbol{\rho}') = \lim_{N\to\infty} \sum_{n=1}^{N} j_n f_n, \tag{3.4}$$

where j_n is the unknown current coefficient and f_n is the predefined basis function. Substituting (3.4) into (3.3) leads to

$$E_z^{\text{inc}}(\boldsymbol{\rho}) \approx \frac{k_0\eta_0}{4} \sum_{n=1}^{N} j_n \int_{C_n} f_n H_0^{(2)}(k_0|\boldsymbol{\rho} - \boldsymbol{\rho}'|)dc', \tag{3.5}$$

where C_n is the source element. For boundary conditions to be satisfied, that is zero tangential electric field on the surface of the PEC, the fields are tested such as

$$\sum_{n=1}^{N} j_n \frac{k_0\eta_0}{4} \int_{C_m} f_m \int_{C_n} f_n H_0^{(2)}(k_0|\boldsymbol{\rho} - \boldsymbol{\rho}'|)dc'dc = \int_{C_m} f_m E_z^{\text{inc}} dc, \tag{3.6}$$

where f_m is the testing function, and C_m is the observer element. Following (3.6), the method of moments yields the following equation [5]

$$\sum_{n=1}^{N} j_n \left\langle f_m, \mathcal{L}(f_n) \right\rangle = \left\langle f_m, E_z^{inc} \right\rangle. \tag{3.7}$$

$\mathcal{L}$ is the inner integral on the left hand side of (3.6) and $\langle\cdot\rangle$ represents the inner product which is a line integral over the observer element for the case of 2D MoM.

The set of N linear equations in (3.7) can be written in the MoM matrix form as

$$\begin{bmatrix} Z_{11} & Z_{12} & \dots & Z_{1N} \\ Z_{21} & Z_{22} & \dots & Z_{2N} \\ \vdots & \vdots & \ddots & \vdots \\ Z_{N1} & Z_{N2} & \dots & Z_{NN} \end{bmatrix} \begin{bmatrix} I_1 \\ I_2 \\ \vdots \\ I_N \end{bmatrix} = \begin{bmatrix} V_1 \\ V_2 \\ \vdots \\ V_N \end{bmatrix}, \tag{3.8}$$

and succinctly as

$$ZI = V, \tag{3.9}$$

where Z is the impedance matrix, V is the excitation vector, and I is the unknown current coefficient vector to be solved.

The entries of impedance matrix hold the information about the interaction between source and observer elements in the geometry. The diagonal entries of the impedance matrix are the self-interaction of elements, whereas non-diagonal entries are the mutual interactions among different elements. A discretized PEC structure in the xy plane is shown in Figure 3.1, with the arrow demonstrating interaction between a source and observer domain.

The interaction between a source and an observer element can be expressed as

$$Z_{mn} = \frac{k_0\eta_0}{4} \int_{C_m} f_m \int_{C_n} f_n H_0^{(2)}(k_0|\boldsymbol{\rho} - \boldsymbol{\rho}'|)dc'dc. \tag{3.10}$$

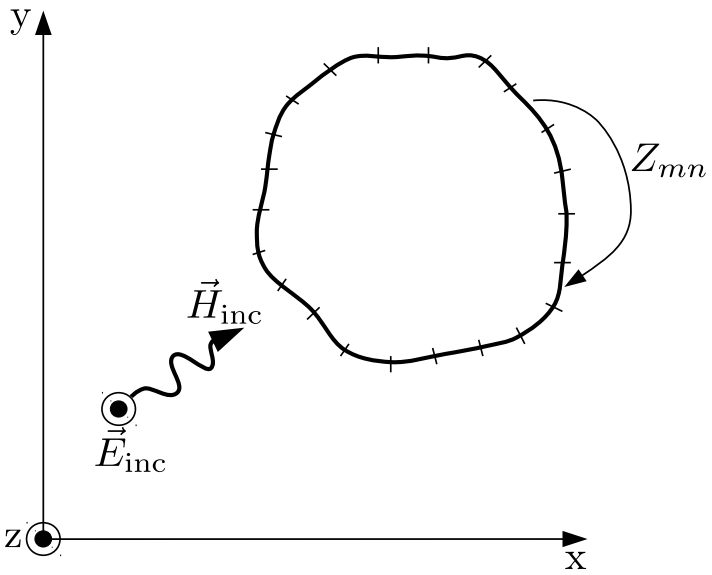

Figure 3.1: Discretized PEC Structure in the xy plane.

Accurate evaluation of the impedance matrix entries for both self and non-self interactions will be discussed in later sections. For self-interaction, a semi-analytical approximation needs to be used because of the singularity of the Green's function at the point where the distance between the source and observation element is near or equal to zero.

The entries of the excitation vector, V, in (3.9) can be expressed as

$$V_m = \int_{C_m} f_m E_z^{inc} dc. \tag{3.11}$$

All the entries of excitation vector are zero for an antenna problem, except for the entries which correspond to the feed.

3.4 Basis and Testing Functions

A piecewise constant pulse basis function has been used in this thesis. If the elements are small enough, it can be approximated that the current distribution over an element is constant. The pulse basis function is defined as

$$f_n(\boldsymbol{\rho}') = \begin{cases} 1, & (\boldsymbol{\rho}') \in C_n \\ 0, & (\boldsymbol{\rho}') \notin C_n \end{cases}, \tag{3.12}$$

where C_n is the n-th element.

A testing function is used to test the incident field onto an observer element due to the induced current on the source element.

The two types of testing functions to be discussed here lead to the **collocation method** and **Galerkin method** respectively.

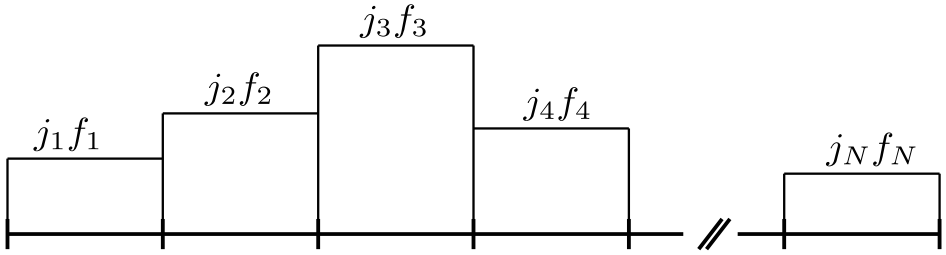

Figure 3.2: Pulse basis function.

3.4.1 Collocation Method

In point collocation [6], the electromagnetic boundary condition is satisfied only at discrete points. In other words, the tangential electric fields on the surface of the PEC is tested to be zero at only a distinct location on the observer's element (e.g., mid-point of the observer element).

A Dirac delta function (zeroth order function) is used as testing function, that is,

$$f_m = \delta(\boldsymbol{\rho} - \boldsymbol{\rho}_m), \tag{3.13}$$

where $\boldsymbol{\rho}_m$ is the midpoint of the m-th element.

Equation (3.10) for non-self interactions using pulse basis function and delta testing function can be written as

$$Z_{mn} = \frac{k_0\eta_0}{4}\int_{C_n} H_0^{(2)}(k_0|\boldsymbol{\rho}_m - \boldsymbol{\rho}'|)dc'. \tag{3.14}$$

Despite the simplicity of the point collocation, the boundary condition is not satisfied on other points except at the midpoint of an element.

3.4.2 Galerkin Method

More accurately, subdomain testing functions can be used. In this way, the boundary condition is tested over the whole subdomain by averaging throughout the domain.

The Galerkin method [6] is commonly used, in which the same basis and testing functions are used. In this work, Galerkin method has been used, which is a piecewise constant pulse basis and testing function. The non-self interaction using pulse basis and testing function (Galerkin method) can thus be written as

$$Z_{mn} = \frac{k_0\eta_0}{4}\int_{C_m}\int_{C_n} H_0^{(2)}(k_0|\boldsymbol{\rho} - \boldsymbol{\rho}'|)dc'dc. \tag{3.15}$$

Apart from the fact that the boundary condition is enforced on average throughout the observer domain, the other advantage of using Galerkin method is that a symmetrical impedance matrix is obtained. Thus reducing the number of inner products that need to be computed for the entries of the impedance matrix. The Galerkin approach with pulse basis functions will be used throughout the rest of this thesis.

3.5 Numerical Integration

To evaluate the entries of the impedance matrix, numerical integration [16] is used to approximate the inner product between the basis and testing functions. A definite integral can be approximated by the summation of the value of the function and its corresponding weight at discrete points on the element, such as

$$I = \int_a^b f(x)dx \approx \sum_{i=1}^{N} w(x_i)f(x_i). \tag{3.16}$$

The accuracy of a MoM solver is directly dependent on how accurate the numerical integration is computed, especially for the case of near-elements since they have large values in the impedance matrix.

3.5.1 Evaluation of Non-Self Terms

The most straightforward numerical integration scheme that can be used to evaluate the inner product between the basis and testing function is using the **midpoint integration**. In this technique, the Green's function is only evaluated at the midpoint of each element, and the value is averaged out over the element. If midpoint integration is used to compute the non-self interaction matrix entries, this will result as

$$Z_{mn} = \frac{k_0\eta_0}{4} l_m l_n H_0^{(2)}(k_0|\boldsymbol{\rho}_m - \boldsymbol{\rho}'_m|), \tag{3.17}$$

where l_n and l_m are the widths of the source and observer elements respectively. Midpoint integration can be accurate only if the integrand varies slowly through the element, which is often not the case in numerical electromagnetics.

Since the value of the Green's function varies rapidly, especially for near interactions, the function needs to be evaluated at several points on the element to obtain adequate accuracy. The use of multiple points on the element can also be motivated for the case where the source and observer elements are non-parallel, as shown in Figure 3.3, in which the distance between the two element varies dramatically from point to point. In techniques such as trapezoidal integration and Simpson's rule [16], the function is evaluated at multiple and equally spaced points.

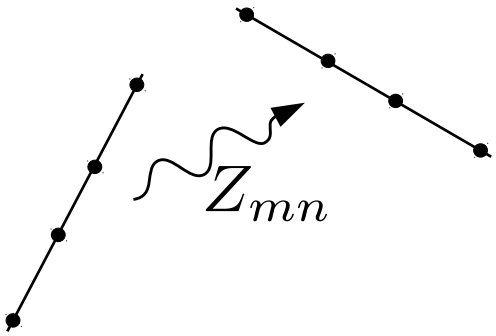

Figure 3.3: Interaction between non-parallel source and observer elements.

A better suited technique for the application of MoM is the **Gauss-Legendre quadrature** [6]. In this technique, the points at which the function is evaluated, are not regularly spaced, but rather at optimal points obtained using the Legendre polynomial [17].

The Gauss-Legendre quadrature usually evaluates functions through an interval of 0 to 1 as

$$\int_0^1 f(a)dx = \sum_{i=1}^{K} w(a_i)f(a_i) \tag{3.18}$$

where K is the number of quadrature points, $w(a_i)$ and $f(a_i)$ are the weight and the value of the function at point i respectively. The points on any arbitrary element in a MoM problem need to be mapped onto an interval from 0 to 1 for the inner product to be computed using the Gauss-Legendre quadrature.

The first and last point on the element are denoted as $\boldsymbol{\rho}_1$ and $\boldsymbol{\rho}_2$ respectively. $l = |\boldsymbol{\rho}_2 - \boldsymbol{\rho}_1|$ is the length of an element. And, l_i is the distance from $\boldsymbol{\rho}_1$ to any point i on the element. Next, normalized coordinates are defined such as $x_1 = 1 - \dfrac{l_i}{l}$ and $x_2 = \dfrac{l_i}{l}$.

Thus, an integral over an element of path C can be approximated [18] as

$$\int_C f(\boldsymbol{\rho})dc = l\int_0^1 f(\boldsymbol{\rho}_1 x_1 + \boldsymbol{\rho}_2 x_2)dx \approx l\sum_{k=1}^{K} w_k f(\boldsymbol{\rho}_1 x_1^{(k)} + \boldsymbol{\rho}_2 x_2^{(k)}). \tag{3.19}$$

Non-self term entries of the impedance matrix as in (3.15) can be evaluated using Gauss-Legendre quadrature (3.19) as

$$Z_{mn} = \frac{k_0\eta_0}{4} l_m l_n \sum_{j=1}^{K} w_j \sum_{i=1}^{K} w_i H_0^{(2)}(k_0|\boldsymbol{\rho}_1^m x_1^j + \boldsymbol{\rho}_2^m x_2^j - \boldsymbol{\rho}_1^n x_1^i - \boldsymbol{\rho}_2^n x_2^i|), \tag{3.20}$$

where i and j denotes the quadrature point on the source and observer element respectively.

3.5.2 Evaluation of Self Term

The self-interacting terms (the diagonal entries of the impedance matrix) have more significant values relative to non-diagonal entries as shown in Figure 3.4, in which, the magnitude of the impedance matrix entries for an antenna array of 10 antennas is shown in logarithmic scale. The disparity in magnitude between the diagonal and far-interacting entries in Figure 3.4 motivates the need to evaluate self-interacting entries accurately.

Because of the singularity of the Green's function for near interactions, (3.20) cannot be used to compute the self-interaction terms. A semi-analytical approximation is used. To increase the accuracy in evaluating self-interaction entries, each element is further divided into sub-elements as shown in Figure 3.5.

The self-interaction of each sub-element is then evaluated (at the mid-point of the sub-element) using the semi-analytical approximation [19] as in (3.21).

$$Z_{m_{\text{sub}}m_{\text{sub}}} \approx \frac{k_0\eta_0 l_{m_{\text{sub}}} l_{n_{\text{sub}}}}{4}\left\{1 - j\frac{2}{\pi}\left[\ln\left(\frac{\gamma k_0 l_{m_{\text{sub}}}}{4}\right) - 1\right]\right\}, \tag{3.21}$$

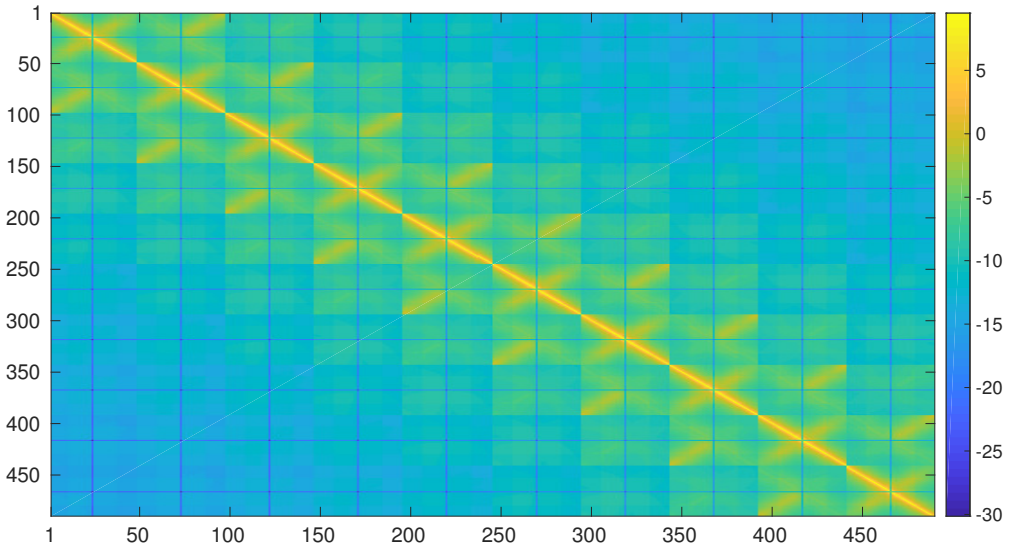

Figure 3.4: Magnitude (in logarithmic scale) of entries in an impedance matrix of an antenna array.

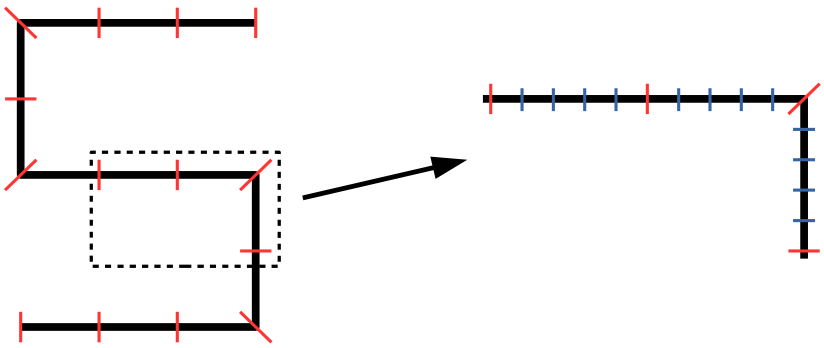

Figure 3.5: Sub-elements to compute self-interaction.

where $l_{n_{\text{sub}}}$ and $l_{m_{\text{sub}}}$ are the width of the source and observer sub-element, which is the same for the case of self-interaction. And, $\gamma \approx 1.7811$.

The interaction among non-self sub-elements are then evaluated using Gauss-Legendre quadrature (similarly to (3.20)) as

$$Z_{m_{\text{sub}}n_{\text{sub}}} = \frac{k_0\eta_0}{4} l_{m_{\text{sub}}} l_{n_{\text{sub}}} \sum_{j=1}^{Q} w_j \sum_{i=1}^{Q} w_i H_0^{(2)}(k_0|\boldsymbol{\rho}_1^{m_{\text{sub}}} x_1^j + \boldsymbol{\rho}_2^{m_{\text{sub}}} x_2^j - \boldsymbol{\rho}_1^{n_{\text{sub}}} x_1^i - \boldsymbol{\rho}_2^{n_{\text{sub}}} x_2^i|). \tag{3.22}$$

A larger number of quadrature points is used in (3.22), Q, as opposed to the one in (3.20), K, since sub-elements are extremely close to each other.

The self-interaction of an element is then accurately obtained by summing the interactions (self and non-self) of all the individual sub-elements.

3.6 Comparison of MoM code to FEKO

To validate the MoM solver, the magnitude of the radiated electric field intensity at a distance of 1000λ is compared to the results of the commercial electromagnetic software, FEKO. The magnitude of the radiated electric field intensity is computed by taking the absolute value of E_z^{scat} in (3.5). A 2D horn antenna structure [20] has been used as shown in Figure 3.6. In FEKO, the periodic boundary condition analysis is used to simulate the 2D structure.

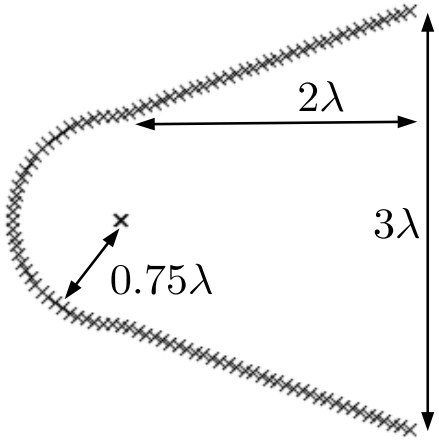

Figure 3.6: 2D Horn antenna structure.

3.6.1 Single Antenna Element

In Figure 3.7, midpoint integration technique is used for the inner and outer integration. The mesh size is varied from $\lambda/8$ to $\lambda/20$. It can be seen, even with a very fine mesh of $\lambda/20$, the MoM code is unable to provide accurate results since the function is evaluated only at the midpoint of each element.

To improve the accuracy of the solver, as in Figures 3.8 and 3.9, Gauss-Legendre quadrature has been employed to compute the inner product for non-diagonal entries in the impedance matrix as in Section 3.5.1. A mesh size of $\lambda/16$ is used. Each element is further divided into sub-elements while computing the self-interaction entries as in Section 3.5.2 and a large number of Gauss-Legendre points have been used for the interaction among sub-elements.

Four cases, as presented in Table 3.1, are compared to FEKO. An improvement compared to using midpoint integration can be seen in test cases (a) to (d). However, the difference in the radiated electric pattern compared to FEKO can still be seen in the test case (a) and (b).

By only increasing the accuracy of self-term evaluation from case (b) to case (c), a very good improvement in accuracy can be observed. A comparison of the test case (c) and FEKO in Figure 3.9 is visually identical. This demonstrates the importance to compute self-interactions accurately, as discussed in section 3.5.2. For the rest of

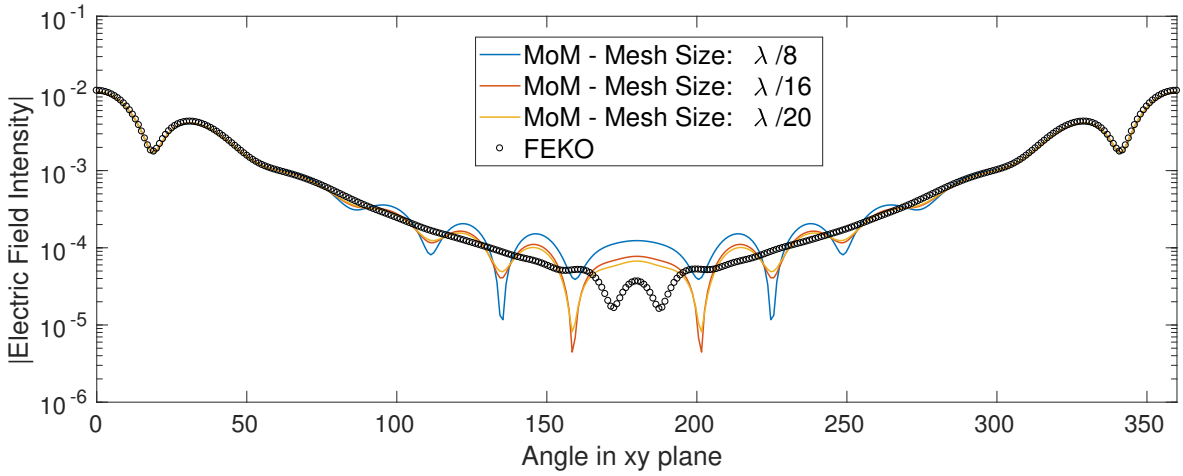

Figure 3.7: Comparison of MoM code and FEKO for radiated electric field of a single antenna element; using midpoint integration.

Test Case	(a)	(b)	(c)	(d)
No. of quadrature points (per element)	2	4	4	8
No. of sub-elements	2	4	10	10
No. of quadrature points (per sub-element)	2	4	8	16

Table 3.1: Quadrature points and number of sub-elements for test cases (a) to (d) in Figures 3.8 and 3.9.

the thesis, parameters mentioned in case (d) are used to assure that a high accuracy is obtained in any test scenario.

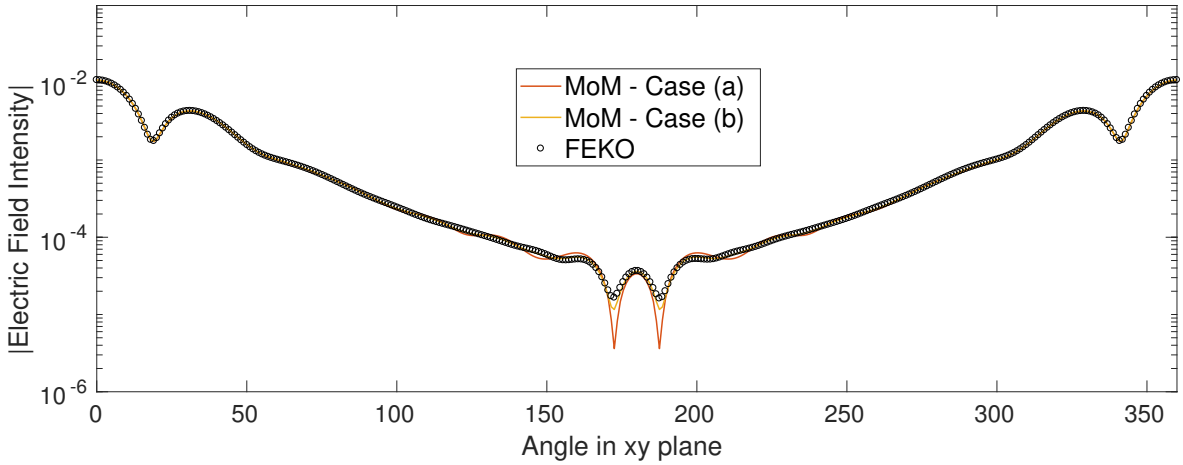

Figure 3.8: Comparison of MoM code and FEKO for radiated electric field of a single antenna element; using Gauss-Legendre quadrature.

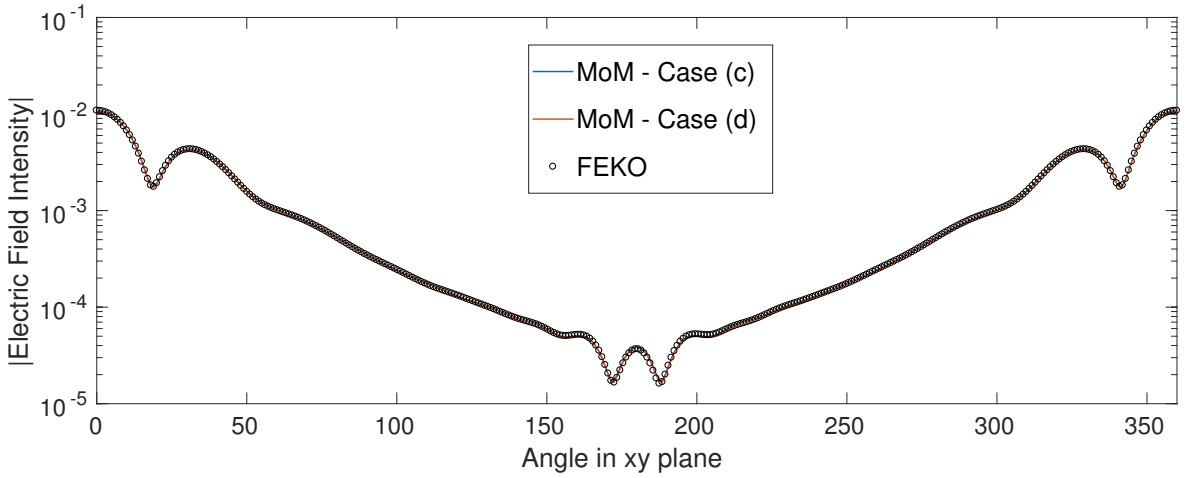

Figure 3.9: Comparison of MoM code and FEKO for radiated electric field of a single antenna element; using Gauss-Legendre quadrature with accurate self-term evaluation.

3.6.2 Antenna Array

Since, in later chapters, analysis of antenna array will be the main concern, the analysis of an antenna array of 3 active antenna elements (as in Figure 3.6) is compared to the results from FEKO. The inter-element distance in the array is 3.5λ and the parameters of test case (d) in Table 3.1 has been used. The result is shown in Figure 3.10, which is visually identical.

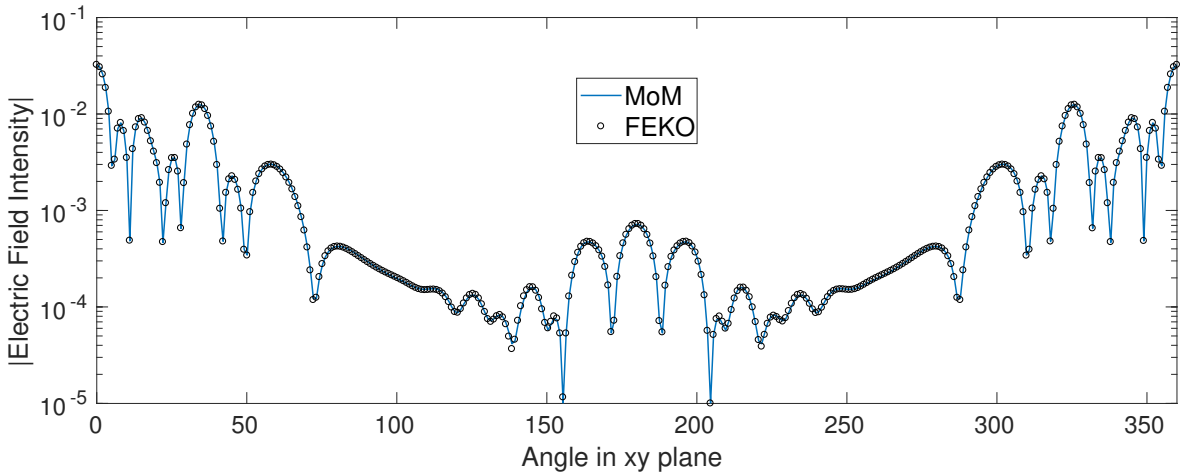

Figure 3.10: Comparison of MoM code and FEKO for radiated electric field of an antenna array; using Gauss-Legendre quadrature.

3.7 Conclusion

In this chapter, the formulation of a MoM solver using pulse basis and testing function from the EFIE has been discussed. Moreover, the Gauss-Legendre quadrature method for numerical integration has been found to produce accurate result while computing

the inner product to generate non-self entries in the impedance matrix. For the case of self-interaction entries, since higher accuracy is required, the element is further divided into sub-elements, and inter sub-elements interaction is computed using a large number of quadrature points and an analytical approximation.

For the rest of the thesis, the following parameters will used in the MoM solver:

- Mesh size : $\lambda/16$
- No. of quadrature points (per element) : 8
- No. of sub-elements : 10
- No. of quadrature points (per sub-element): 16.

Chapter 4

Characteristic Basis Function Method

4.1 Introduction

In Chapter 3, the formulation of 2D, TM MoM from the EFIE has been discussed. Very accurate results for electromagnetic problems can be obtained with MoM depending on the mesh size. However, MoM is computationally very expensive. The memory and computational cost scales as $\mathcal{O}(N^2)$ and $\mathcal{O}(N^3)$ respectively, where N is the number of basis functions. For this reason, the electrical size solvable with given computational resources can be quite limited.

For larger problems, fast techniques which are based on the MoM need to be employed. Fast integral equation techniques can be classified as iterative or direct solvers. Iterative solvers such as the Multilevel Fast Multipole Method (MLFMM) [21] have heavily been used as a fast integral equation technique since it reduces the computational cost to $\mathcal{O}(N \log N)$. However, to solve for antenna array problems, non-iterative (or direct) solvers are often preferred, since the simulation needs to start anew for each excitation scheme while using iterative solvers.

The Macro Basis Function [9] method is a non-iterative technique which is suitable to solve for finite antenna array problems. This method uses a 'divide and conquer' methodology to solve a large problem. That is, the entire geometrical domain is divided into subdomains, over which physics-based Macro Basis Functions (MBFs) are defined. MBFs are created by forming fixed linear combinations of low-order basis functions (e.g., pulse basis function) on an isolated subdomain or due to the effect of neighbouring subdomains. This technique therefore aims to improve the computational cost by reducing the total number of MoM degrees of freedom, to obtain a smaller system which can be directly solved.

Different variants of MBF methods have been developed over the years, namely the Characteristic Basis Function Method (CBFM) [10, 22], Synthetic-Function Approach (SFX) [23], the eigencurrent method [24], and the Sub Entire Domain (SED) basis function method [25]. The major differences among the methods are in the way the MBFs are created, interaction among MBFs and how subdomains are connected.

Since the CBFM is well suited and has been developed for antenna array problems [26, 27, 28] in recent years, it is the starting point of this work.

4.2 Formulation of CBFM

Similar to the description of MBF methods in Section 4.1, in CBFM also the first step is to decompose the entire geometry into subdomains. In this chapter and the literature [26, 27, 29], a subdomain is considered as an antenna element in the array since it is the most straightforward symmetry in the array. The schematic of the 2D antenna array to be used throughout this chapter is shown in Figure 4.1.

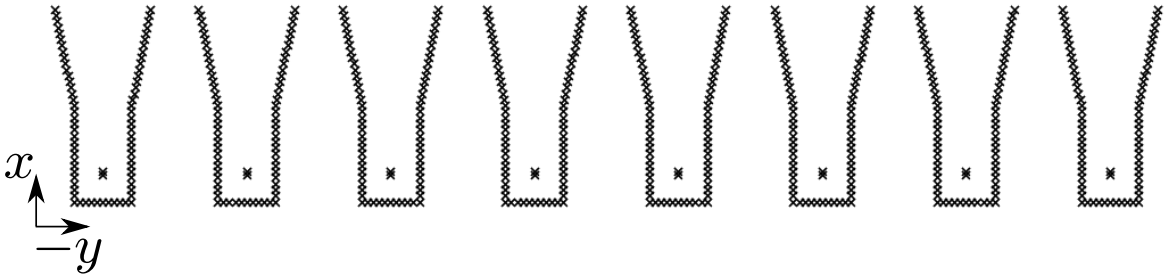

Figure 4.1: Schematic of the 2D antenna array used in this chapter.

Decomposing an antenna array of M antenna elements into subdomains would imply partitioning of the MoM matrix equation (3.8) such as

$$\begin{bmatrix} Z_{11} & Z_{12} & \dots & Z_{1M} \\ Z_{21} & Z_{22} & \dots & Z_{2M} \\ \vdots & \vdots & \ddots & \vdots \\ Z_{M1} & Z_{M2} & \dots & Z_{MM} \end{bmatrix} \begin{bmatrix} I_1 \\ I_2 \\ \vdots \\ I_M \end{bmatrix} = \begin{bmatrix} V_1 \\ V_2 \\ \vdots \\ V_M \end{bmatrix}. \tag{4.1}$$

The block-diagonal entries, Z_{aa}, in the partitioned impedance matrix (4.1) is the self interaction of an isolated subdomain. That is, Z_{aa} consists of interactions among pulse basis and testing functions within a single antenna element. Non block-diagonal entries, Z_{ab} (where a,b $\in$ {1,2,...,M}) are interaction among two antenna elements, where the basis functions lie on subdomain b and testing functions lie on subdomain a.

Over each subdomain, physics-based MBFs called Characteristic Basis Functions (CBFs) are defined. The number of CBFs is much less compared to the number of low-level basis functions (i.e., pulse basis functions). Moreover, if all the antenna elements are identical, then, CBFs can be defined only once and used for all subdomains.

4.3 Generation of CBFs

CBFs are generated to approximate the current distribution over a subdomain. Depending on the electromagnetic problem, there are several ways of generating CBFs. For instance, in scattering problems, a plane-wave spectrum method is used [30, 31].

For antenna array problems, CBFs are to be classified as primary, secondary [10] or even higher-order (e.g. tertiary [27] and quaternary [32]) scattering CBFs. The primary CBF takes into account the self-interaction of an isolated subdomain, whereas secondary and higher-order CBFs take mutual coupling among subdomains into account.

In Subsections 4.3.1 to 4.3.3, the generation of CBFs for radiation problems, more specifically for antenna arrays, is discussed.

4.3.1 Primary CBF

As mentioned in Section 4.3, the primary CBF takes into account the effect of self-interaction of a subdomain. This is performed by allowing an isolated subdomain (an antenna element) to radiate in free space, and the unknown current coefficients are computed such as

$$Z_{ii} I_{\text{prim}} = V_i, \tag{4.2}$$

where I_{prim} is the primary CBF, Z_{ii} is the impedance matrix of the isolated subdomain and V_i is the excitation vector where only the feed of the antenna is active.

Since the solver is in 2D, TM MoM context, the induced current is only in the z-axis and no current flows in the xy plane (Figure 3.1). Thus, cases for connected antennas need not be considered here. However, in 3D instances, an extended subdomain is used to deal with current continuity such as in [26] for CBFM. In the SFX method, a connection basis function is used for this purpose as in [23].

4.3.2 Secondary CBFs

Secondary CBFs are included to take into account the effect of mutual coupling due to neighbouring subdomains. Secondary current is the induced current due to the radiated field produced by primary CBFs belonging to neighbouring subdomains within a pre-defined **radius of influence**.

E_{ji}, the radiated field due to a primary CBF on subdomain i onto a secondary domain j can be written as

$$E_{ji} = -Z_{ji} I_{\text{prim}}, \tag{4.3}$$

where Z_{ji} is the interaction matrix between the source and observer subdomains.

The induced secondary CBF, I_{sec}, can then be computed by

$$Z_{jj} I_{\text{sec}} = E_{ji}. \tag{4.4}$$

A radius of influence needs to be defined within only which the influence of antennas are taken into consideration. The reason is that the intensity of the field decreases with distance, leading to distant subdomains having a small impact on each other, thus can be excluded to make the solver efficient.

4.3.3 Tertiary and Higher-Order CBFs

Higher-order scattering CBFs can be obtained similarly as secondary CBFs. For instance, tertiary CBFs [27, 33, 34] can be obtained by allowing secondary CBFs within the radius of influence to radiate onto an observer subdomain. This step can be repeated up to any CBF order to model the effect of mutual coupling among subdomains better, thus increasing the accuracy. However, generation and inclusion of higher-order CBFs increase the computational burden of the solver, therefore should be limited depending both on the accuracy required and the computational cost.

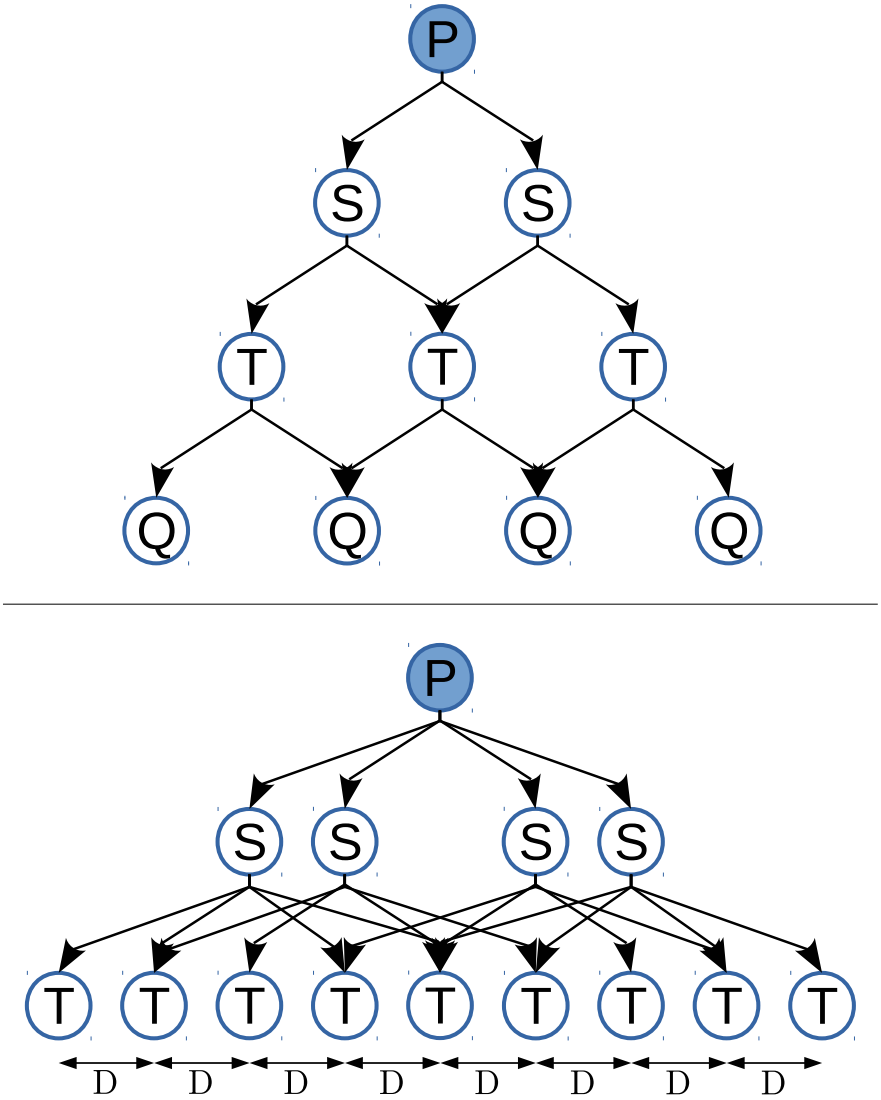

Figure 4.2: Tree structure to generate higher-order CBFs. Top Figure: Up to quaternary CBFs; radius of influence – D. Bottom Figure: Up to tertiary CBFs; radius of influence – $2D$.

Figure 4.2 shows the tree structure to generate higher-order CBFs using a radius of influence of one antenna element, D. The primary CBF radiates onto the closest neighbouring subdomain in each direction to generate secondary CBFs. In the case of a linear antenna array, this would imply two secondary CBFs (in each direction). The same procedure is repeated to generate higher-order CBFs. If a radius of influence of $2D$ (two closest antennas in each direction for a linear antenna array) is used instead, this will imply the generation of 4 secondary CBFs, 16 tertiary CBFs, and so forth. Increasing the radius of influence or the order of CBFs rapidly increases the total number of CBFs per subdomain. Depending on the accuracy required, the number of CBFs to be generated needs to be controlled to ensure sufficient improvement in computational cost. CBFs are generated for each antenna element (subdomain) in the array. However, for the case of a regular array, the generation of CBFs can be performed only once and be used for all the subdomains, with exceptions for antennas

close to edge of the array.

In the literature, the highest order of CBFs usually included is up to secondary or tertiary. However, in this thesis, results up to quaternary will be presented to show the convergence of accuracy using CBFM.

4.4 SVD operation on CBFs

After the generation of CBFs up to the desired order, a Singular Value Decomposition (SVD) [35] is performed to generate orthonormal basis functions. Moreover, the SVD operation also keep only a minimum number of CBFs in order to avoid ill-conditioning of the reduced impedance matrix and to be computationally efficient. This is possible since the CBFs generated for a subdomain in Section 4.3 might be linearly dependent, thus adding an insignificant contribution to creating the reduced system. By using a threshold value, only significant CBFs are retained.

The CBFs belonging to a subdomain are firstly grouped in a column augmented vector as

$$J^{\text{Pre-CBF}} = \begin{bmatrix} I_P & I_{S1} & I_{S2} & I_{T1} & I_{T2} & \dots \end{bmatrix}, \tag{4.5}$$

where each of the entries is a column vector representing a CBF. The size of the column augmented vector is $N_{\text{sub}} \times K_a$, where N_{sub} is the number of low-order basis function in the subdomain and K_a is the number of CBFs generated per subdomain. The augmented vector can be decomposed through the SVD operation as

$$J^{\text{Pre-CBF}} = UDV^H. \tag{4.6}$$

U is an orthogonal matrix $N_{\text{sub}} \times K_a$, V is a unitary matrix of size $K_a \times K_a$, and D is a diagonal matrix of size $K_a \times K_a$. The superscript H refers to the Hermitian transpose of a matrix. The diagonal entries of D are the singular values of the CBFs and are ordered in ascending order, such as $\sigma_1 > \sigma_2 > \dots \sigma_{k_a}$. Low singular value implies the corresponding CBF has a low contribution, thus can be discarded. The n-th column in the U matrix corresponds to the n-th diagonal entry in the matrix D. Only columns having corresponding normalized singular values greater than a pre-defined threshold value, τ, are retained. The n-th normalized singular value, λ_n, is given as

$$\lambda_n = \frac{\sigma_n}{\sigma_{\max}}, \tag{4.7}$$

where $\sigma_{max} = \sigma_1$. Typical threshold values lies between 10^{-3} to 10^{-5} [29] for CBFM depending on the desired accuracy. The first K-th columns having singular values greater than the threshold value are selected from the U matrix to form a new set of CBFs which are orthogonal and linearly independent, such as

$$J^{\text{CBF}} = \begin{bmatrix} CBF_1 & CBF_2 & CBF_3 & CBF_4 & \dots & CBF_K \end{bmatrix}. \tag{4.8}$$

4.5 Reduced Impedance Matrix

After having a set of CBFs per subdomain (which is the same for all subdomains in the case of a regular array except close to endpoints), a reduced impedance matrix is to be

created. The entries of the impedance matrix are obtained by pre and post-multiplying interaction matrices among subdomains with the corresponding CBF groups' column matrices. The reduced impedance matrix equation can be written as

$$\begin{bmatrix} \langle {J_1}^H, Z_{11} J_1 \rangle & \langle {J_1}^H, Z_{12} J_2 \rangle & \dots & \langle {J_1}^H, Z_{1M} J_M \rangle \\ \langle {J_2}^H, Z_{21} J_1 \rangle & \langle {J_2}^H, Z_{22} J_2 \rangle & \dots & \langle {J_2}^H, Z_{2M} J_M \rangle \\ \vdots & \vdots & \ddots & \vdots \\ \langle {J_M}^H, Z_{M1} J_1 \rangle & \langle {J_M}^H, Z_{M2} J_2 \rangle & \dots & \langle {J_M}^H, Z_{MM} J_M \rangle \end{bmatrix} \begin{bmatrix} {I_1}^{CBF} \\ {I_2}^{CBF} \\ \vdots \\ {I_M}^{CBF} \end{bmatrix} = \begin{bmatrix} {V_1}^{CBF} \\ {V_2}^{CBF} \\ \vdots \\ {V_M}^{CBF} \end{bmatrix}. \tag{4.9}$$

The impedance matrix and excitation vector entries can succinctly be expressed as in (4.10) and (4.11) respectively for the p-th observer subdomain and q-th source subomain.

$$Z_{pq}^{\text{CBF}} = \langle {J_p}^H, Z_{pq} J_q \rangle \tag{4.10}$$

$$V_p^{\text{CBF}} = \langle {J_p}^H, V_p \rangle \tag{4.11}$$

The size of the reduced matrix is $KM \times KM$, where K is the number of CBFs per subdomain after the SVD operation and M is the number of subdomains (or antenna elements). The computational cost still scales as $\mathcal{O}((KM)^3)$. However, since KM is much smaller than the total number of lower-order basis function (Pulse basis functions), N, the computational cost of inverting the reduced impedance matrix compared to a full MoM matrix is considerably cheaper.

The construction of the reduced matrix is the most expensive part of the CBFM method since the interaction matrix for each subdomain pair needs to be pre and post-multiplied. However, far interaction matrices have a low rank due to the increasingly slower radiated field magnitude variation, as distance increases. Thus, a low rank revealing technique such as the ACA has been employed in [26].

Once the coefficient from the reduced matrix equation is obtained, the final current coefficient on the p-th subdomain can be computed by multiplying the CBF coefficients with the set of CBFs in (4.8) and summing the columns such as

$$I_p = \sum_{i=1}^{K} I_p^{\text{CBF}} J_{p,i}^{\text{CBF}} \tag{4.12}$$

4.6 Comparison Between CBFM and MoM Numerical Results

In this section, numerical experiments are performed to compare the accuracy of the results obtained using MoM and CBFM codes. A threshold value for SVD of 10^{-5} is chosen. The problem to be solved is a linear horn antenna array in 2D context, where the dimensions are given in Figure 4.3. Only two antenna elements are shown here for brevity; however, larger arrays will be modeled. The mesh size used in the numerical experiments is as mentioned in Chapter 3 (i.e., $\lambda/16$) and the excitation frequency is 300 MHz.

In this numerical experiment, an antenna array of 10 elements is used, where only the first element is excited. In this configuration the capability of the CBFM to model

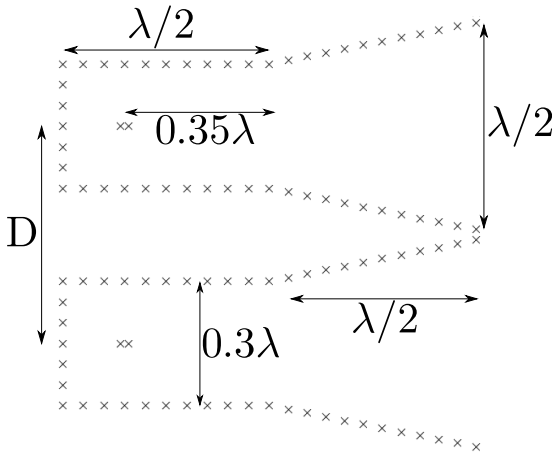

Figure 4.3: Structure of problems to be solved.

induced currents due to mutual coupling, can be studied well. The CBFM current error, ϵ, relative to the MoM current is measured as

$$\epsilon = \frac{||I_{\text{MoM}} - I_{\text{CBFM}}||_2}{||I_{\text{MoM}}||_2}. \tag{4.13}$$

The **radius of influence**, **order of CBFs** and the **distance between elements** are varied in the numerical examples. Figures 4.4 and 4.5 show the errors in the current coefficients of the low-level basis functions for the setup where the distance between two antenna elements, D (in Figure 4.3), is 0.525λ. That is, the distance between the tip of the flares of two adjacent antenna elements in the array is only 0.025λ, implying strong mutual coupling among antenna elements. From Figures 4.4 and 4.5, it can be seen that using higher-order CBFs (Tertiary and Quaternary CBFs) increases the accuracy of the solver. In Figure 4.5, since a larger radius of influence is used ($3D$ instead of D in Figure 4.4), the current error converges faster, that is, the inclusion of quaternary CBFs does not improve the accuracy compared to tertiary.

Using a lower SVD threshold value, e.g., $\tau = 10^{-6}$, including quaternary CBFs would further improve the current error even for a radius of influence of $3D$. The SVD threshold value limits the number of degrees of freedom to ensure a memory efficient solver.

Table 4.1 sums up the size of the reduced matrix and corresponding current error (as computed in (4.13)) for Figures 4.4 and 4.5. From Table 4.1, it is clear that the size of the reduced impedance matrix increases with the order of CBFs. For instance, using up to quaternary with a radius of influence of D, the size of the reduced matrix is 110×110 instead of 410×410 for a full MoM matrix, which means the number of CBFs used is 26.8% compared to the number of lower order basis functions. For a given array configuration, the extent of the reduction is dependent on the number of MoM degrees of freedom per array element, as the number of CBFs is dependent only on the CBF order and the array configuration. It is not dependent on the array element geometry. Moreover, the small increase in the reduced matrix size, in Table 4.1, when using up to tertiary and quaternary CBFs for a radius of influence of $3D$ is due to the limit imposed by the SVD threshold value.

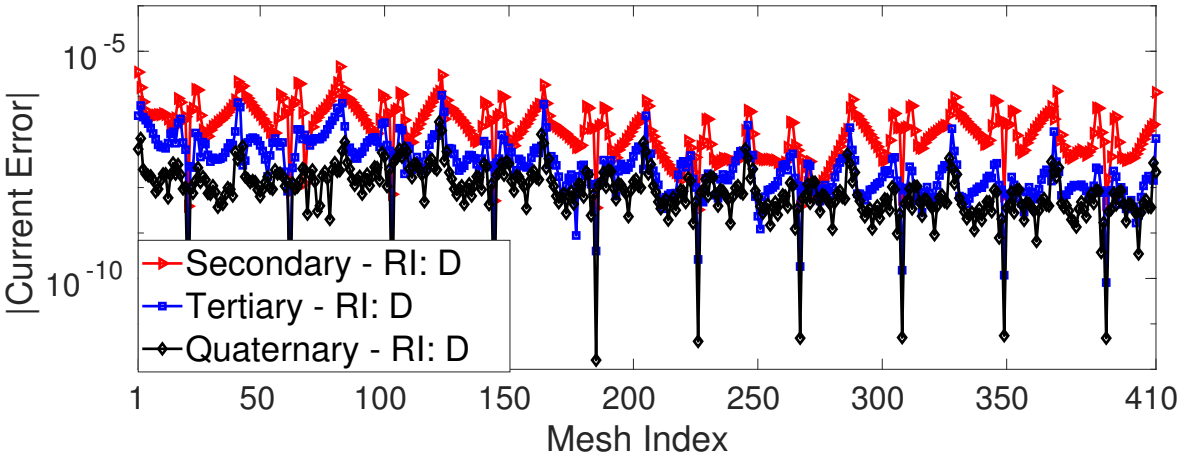

Figure 4.4: Current coefficient errors for antenna array of 10 elements with array spacing $D = 0.525\lambda$, using CBFM with up to quaternary CBFs. A radius of influence of D is used.

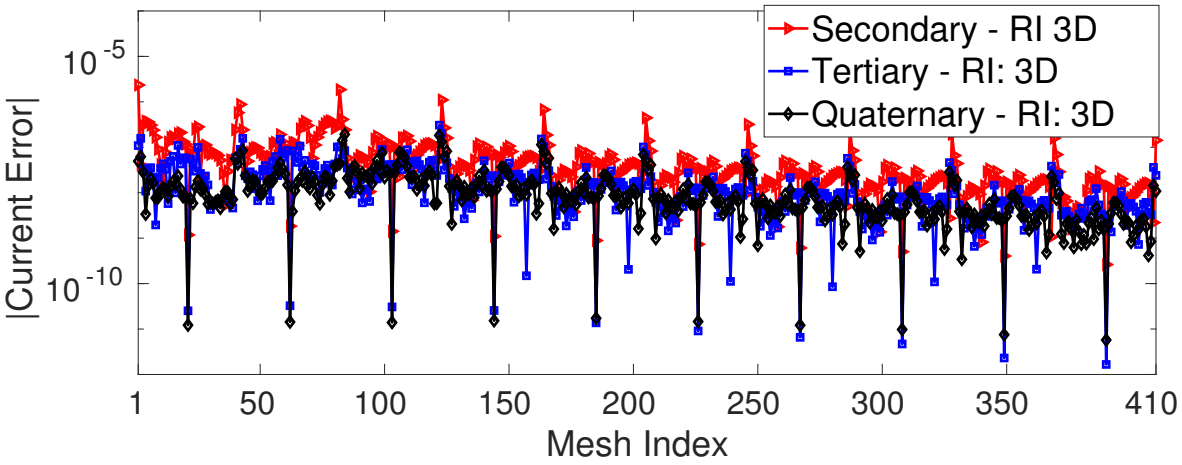

Figure 4.5: Current coefficient errors for antenna array of 10 elements with array spacing $D = 0.525\lambda$, using CBFM with up to quaternary CBFs. A radius of influence of $3D$ is used.

Figures 4.6 and 4.7, are similar numerical experiments except that the distance between two antenna elements (from Figure 4.3), D, is now 1.5λ, meaning the shortest distance between the tip of the flare of two adjacent antenna element is λ. As expected, the inclusion of tertiary CBF increases the accuracy compared to using only up to secondary CBF. However, the current coefficient error converges quicker, and the inclusion of quaternary CBFs does not improve the accuracy. The faster convergence can be attributed to weaker mutual coupling.

Table 4.2, summing up the reduced matrix size and current error for Figures 4.6 and 4.7, shows that a smaller number of CBFs is needed compared to Table 4.1. The reason being that, for dense antenna arrays, mutual coupling is higher, hence more degrees of freedom are required to model the current distribution accurately.

The far-field radiated electric field (z-component), computed using (4.14), is shown in Figures 4.8 to 4.11 corresponding to current error in Figures 4.4 to 4.7 respectively.

D	Radius of Influence	Order	Reduced Matrix Size	Current Error (ϵ)
0.525λ	D	Secondary	30	3.5851e-04
0.525λ	D	Tertiary	70	8.0164e-05
0.525λ	D	Quaternary	110	1.7187e-05
0.525λ	$3D$	Secondary	70	1.2129e-04
0.525λ	$3D$	Tertiary	110	2.2612e-05
0.525λ	$3D$	Quaternary	130	1.6003e-05

Table 4.1: Dimensions of reduced matrices for different orders of CBFs. The dimensions of the full MoM matrix is 410.

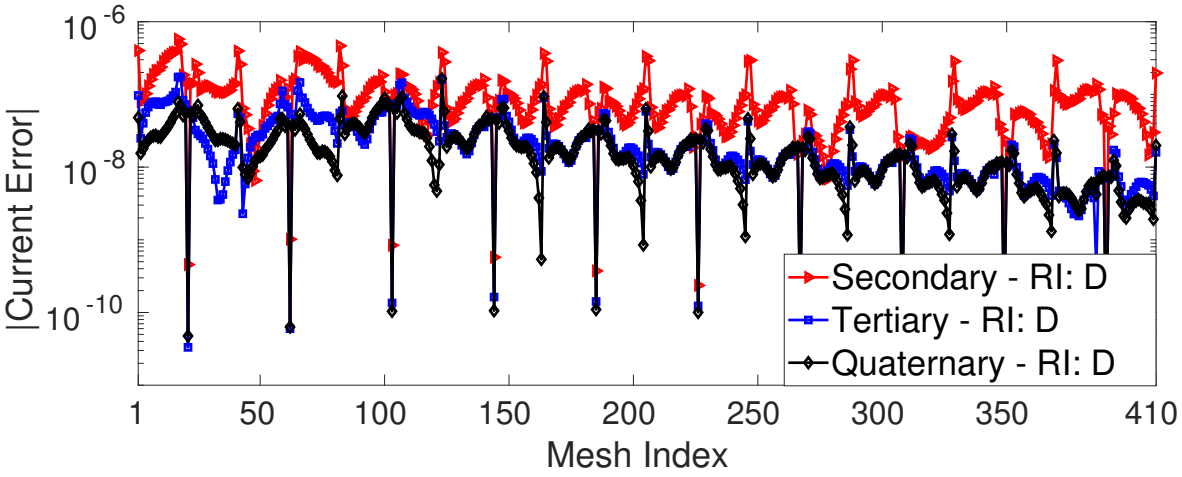

Figure 4.6: Current coefficient errors for antenna array of 10 elements with array spacing $D = 1.5\lambda$, using CBFM with up to quaternary CBFs. A radius of influence of D is used.

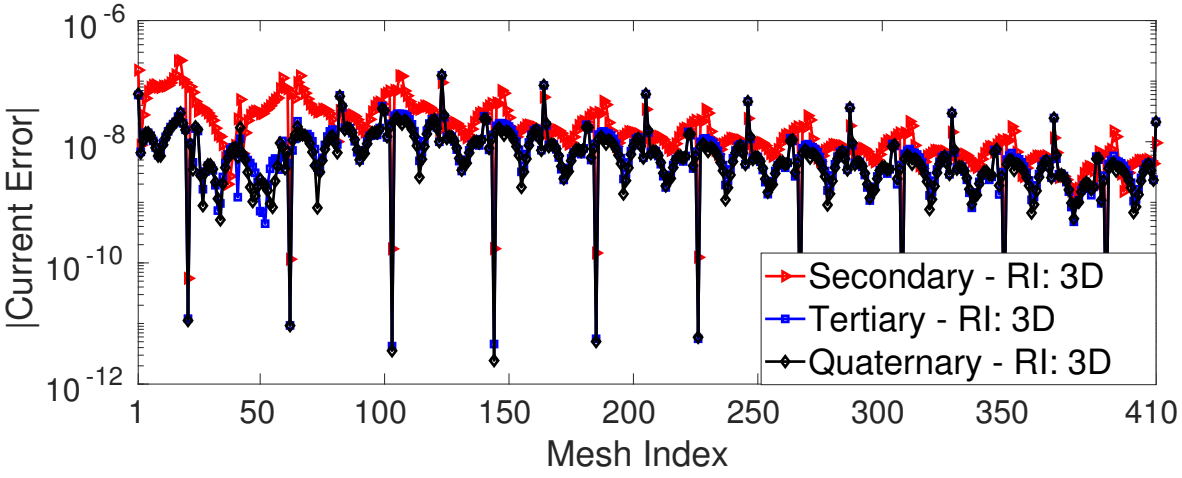

Figure 4.7: Current coefficient errors for antenna array of 10 elements with array spacing $D = 1.5\lambda$, using CBFM with up to quaternary CBFs. A radius of influence of $3D$ is used.

$$|F(\phi)| = \frac{|E(\phi, \rho)|}{\sqrt{\rho}} \tag{4.14}$$

D	Radius of Influence	Order	Reduced Matrix Size	Current Error (ϵ)
1.5λ	D	Secondary	30	8.0983e-05
1.5λ	D	Tertiary	50	2.3570e-05
1.5λ	D	Quaternary	60	1.7127e-05
1.5λ	$3D$	Secondary	50	2.2266e-05
1.5λ	$3D$	Tertiary	70	8.5798e-06
1.5λ	$3D$	Quaternary	70	8.2206e-06

Table 4.2: Dimensions of reduced matrices for different orders of CBFs. The dimensions of the full MoM matrix is 410.

The radiated field graphs are compared to the full MoM solution. For Figures 4.8 and 4.9, using only up to secondary CBFs fails to model the far field pattern accurately. Using higher-order CBFs (up to tertiary or quaternary), accurate comparison to the MoM solution has been obtained. For the case of using a larger radius of influence of $3D$, satisfactory results is obtained using only up to secondary CBFs. From Tables 4.1 and 4.2, it can be noted that the number of CBFs used relates strongly to the accuracy of the far field pattern, meaning that a large reduction in the impedance matrix can be obtained only at the expense of the final accuracy.

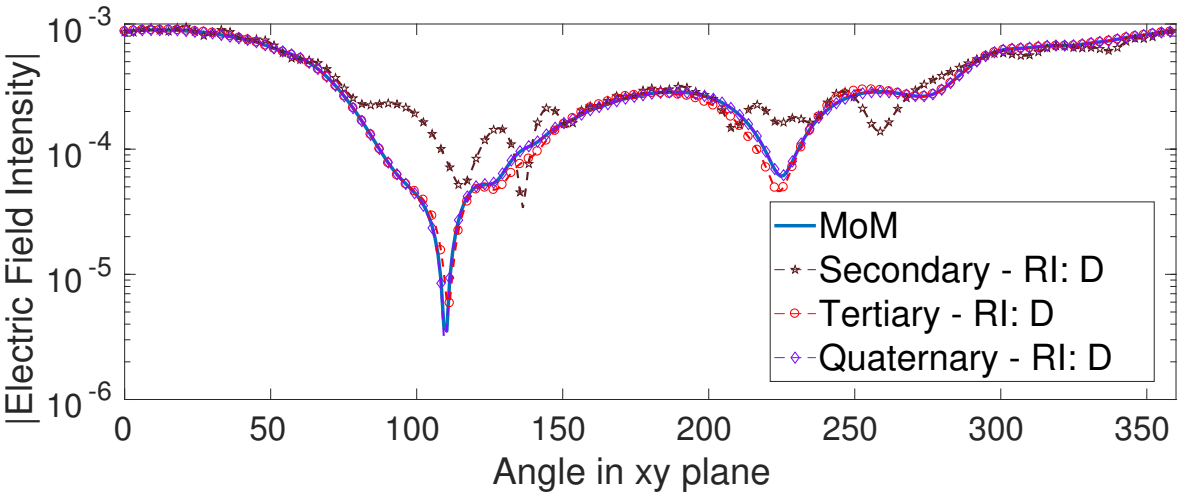

Figure 4.8: Magnitude of the radiated electric far field for array spacing $D = 0.525\lambda$, using the CBFM with up to quaternary CBFs. Radius of influence is D

4.7 Conclusion

In this chapter, the CBFM method has been discussed, in which, the entire geometry is divided into subdomains to generate CBFs (physics-based macro basis functions). A subdomain is considered as an antenna element in this chapter. Up to quaternary CBFs have been generated after SVD operation is performed. The results of a numerical experiment on a linear array, where only the first antenna element is excited have been

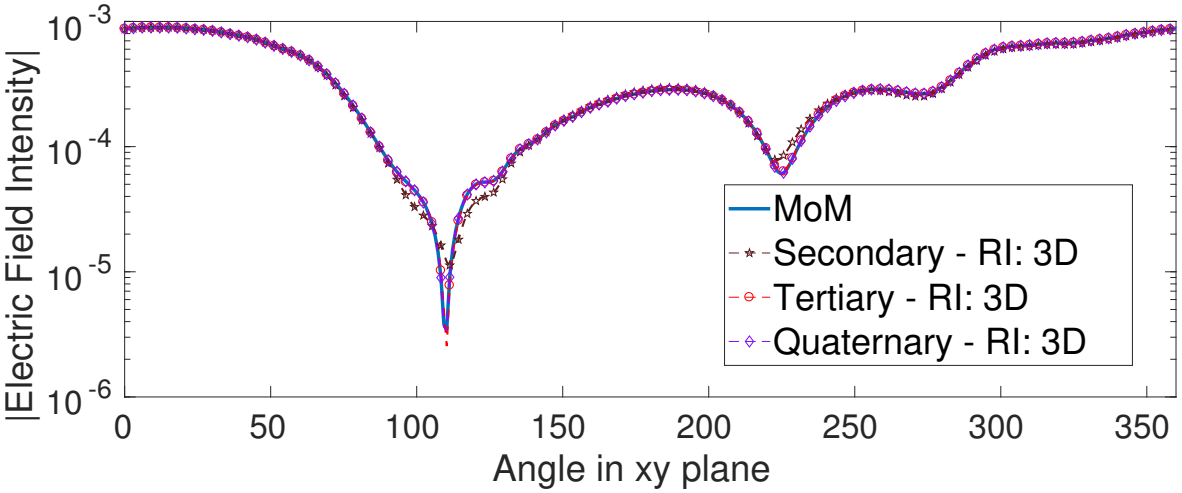

Figure 4.9: Magnitude of the radiated electric far field for array spacing $D = 0.525\lambda$, using the CBFM with up to quaternary CBFs. Radius of influence is $3D$

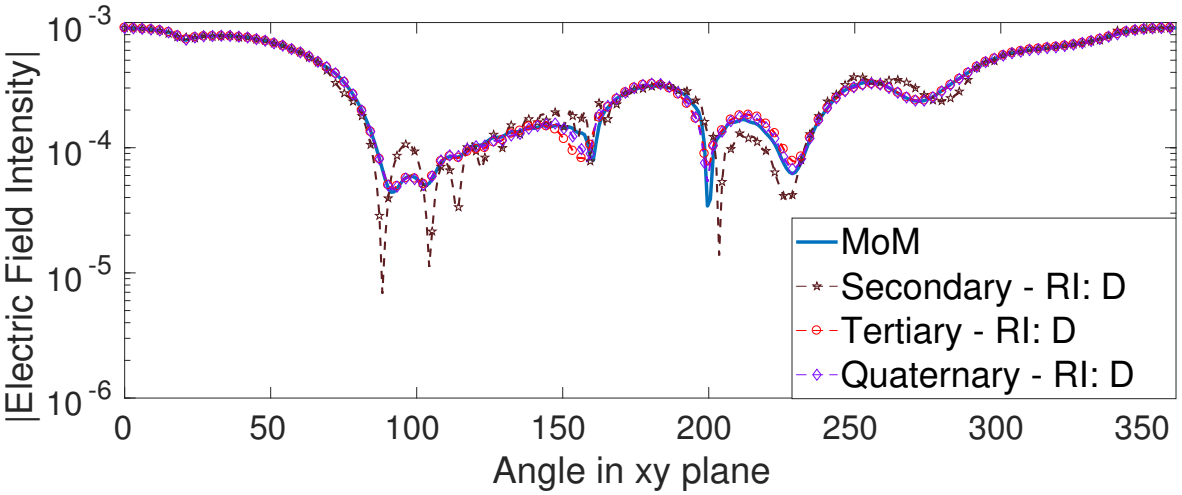

Figure 4.10: Magnitude of the radiated electric far field for array spacing $D = 1.5\lambda$, using the CBFM with up to quaternary CBFs. Radius of influence is D

considered. Increasing the order of CBF and radius of influence contributes to the improvement of the accuracy of the CBFM solver, however, at the expense of being computationally more expensive. That is, more degrees of freedom are required. In the later chapters, methods to obtain better accuracy using fewer CBFs will be investigated.

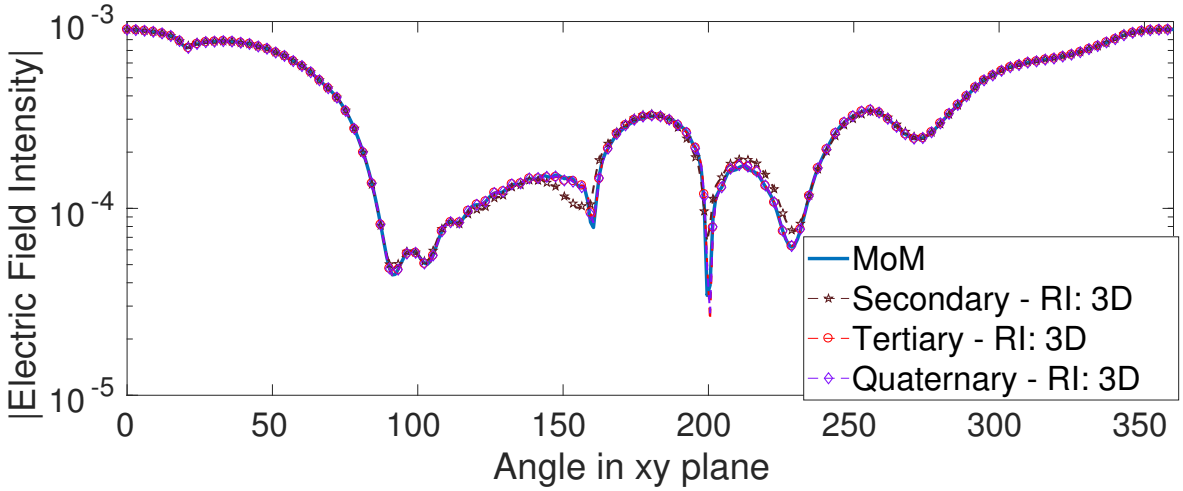

Figure 4.11: Magnitude of the radiated electric far field for array spacing $D = 1.5\lambda$, using the CBFM with up to quaternary CBFs. Radius of influence is $3D$

Chapter 5

CBFM with Larger Overlapping Subdomains

5.1 Introduction

In Chapter 4, the concept of CBFM has been established. As mentioned previously, in CBFM literature [29], it is usual practice to use an antenna element as a subdomain since it is the simplest symmetry in the array. However, when dense antenna arrays are considered, or any case of high mutual coupling, it can be difficult to obtain accurate results. In these cases, accurate results can be obtained by the inclusion of higher-order scattering CBFs. However, as mentioned earlier, using a larger number of CBFs increases the computational cost of the solver, hence less reduction in impedance matrix size is achieved.

To better take into account mutual coupling, in this chapter the idea of generating CBFs which span multiple antenna elements is explored [36]. It should be noted that the number of subdomains is still equal to the number of antenna elements to ensure that any excitation scheme can be modeled with the solver. The subdomains are bigger in size and overlap with the adjacent subdomain.

5.2 Larger Subdomain Primary CBFs

The size of the primary subdomain is defined by a **subdomain radius**. For instance, a subdomain radius, D, where D is the inter-element distance in a regular linear array, the primary domain includes an active antenna and the closest adjacent antenna in every direction to the excited one. Thus, a subdomain radius of nD consists of an active antenna in the domain and the n closest antenna in every direction. By this definition, the conventional CBFM discussed in the Chapter 4 has a subdomain radius zero.

The concept of larger subdomain size is shown in Figure 5.1, where each column represents a linear antenna array with a different subdomain configuration. Each circle in Figure 5.1 corresponds to an antenna element and the shaded circle is the active antenna in the subdomain. In Figure 5.1(b), a primary subdomain having a subdomain radius D is shown. The subdomains of the edge elements are shown in Figures 5.1(a) and 5.1(c) where the subdomain size is only two antenna elements.

To include the effects of antenna elements further away in the primary CBF, the case of subdomain radius $2D$ is shown in Figures 5.1(d) to 5.1(f). The cases of edge and pre-edge element are shown in Figures 5.1(d) and (e) respectively. It should be noted that since subdomains span over multiple antenna elements, adjacent or near subdomains can overlap with each other.

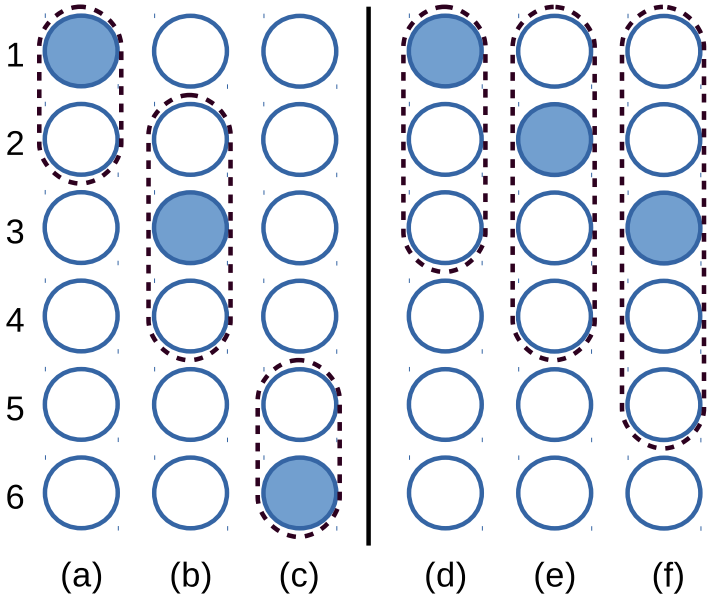

Figure 5.1: Multiple antenna elements subdomains for primary CBFs. (a)-(c): Subdomain radius D, (d)-(f): Subdomain radius $2D$

The primary CBF for a subdomain radius D, e.g., primary CBF, in Figure 5.1(b), can be computed as

$$\begin{bmatrix} I_{P1} \\ I_{P2} \\ I_{P3} \end{bmatrix} = \begin{bmatrix} Z_{11} & Z_{12} & Z_{13} \\ Z_{21} & Z_{22} & Z_{23} \\ Z_{31} & Z_{32} & Z_{33} \end{bmatrix}^{-1} \begin{bmatrix} 0 \\ V_2 \\ 0 \end{bmatrix}. \tag{5.1}$$

Since mutual coupling due to adjacent elements has the highest non-self contribution in the block MoM matrix equation, including the neighbouring antennas in the primary subdomain can allow for more accurate modeling of the surface current instead of using multiple higher-order CBFs with a single antenna subdomain.

Despite having an increase in accuracy, only primary CBFs cannot be used to correctly model the surface current over the array unless of course, when the subdomain size is equal to the array size. This would imply solving the MoM equation, which defies the purpose of using the CBFM technique.

Figure 5.2 shows the current over an array using only primary CBFs with subdomain radius D compared to a MoM solution. Using only large domain, primary CBFs, it is not possible to accurately model the current distribution of passive elements outside the subdomain. Moreover, at the end of the subdomain, the current distribution is inaccurate due to the edge effect of the subdomain. For these two reasons, there is the need to include higher-order CBFs which represent coupling.

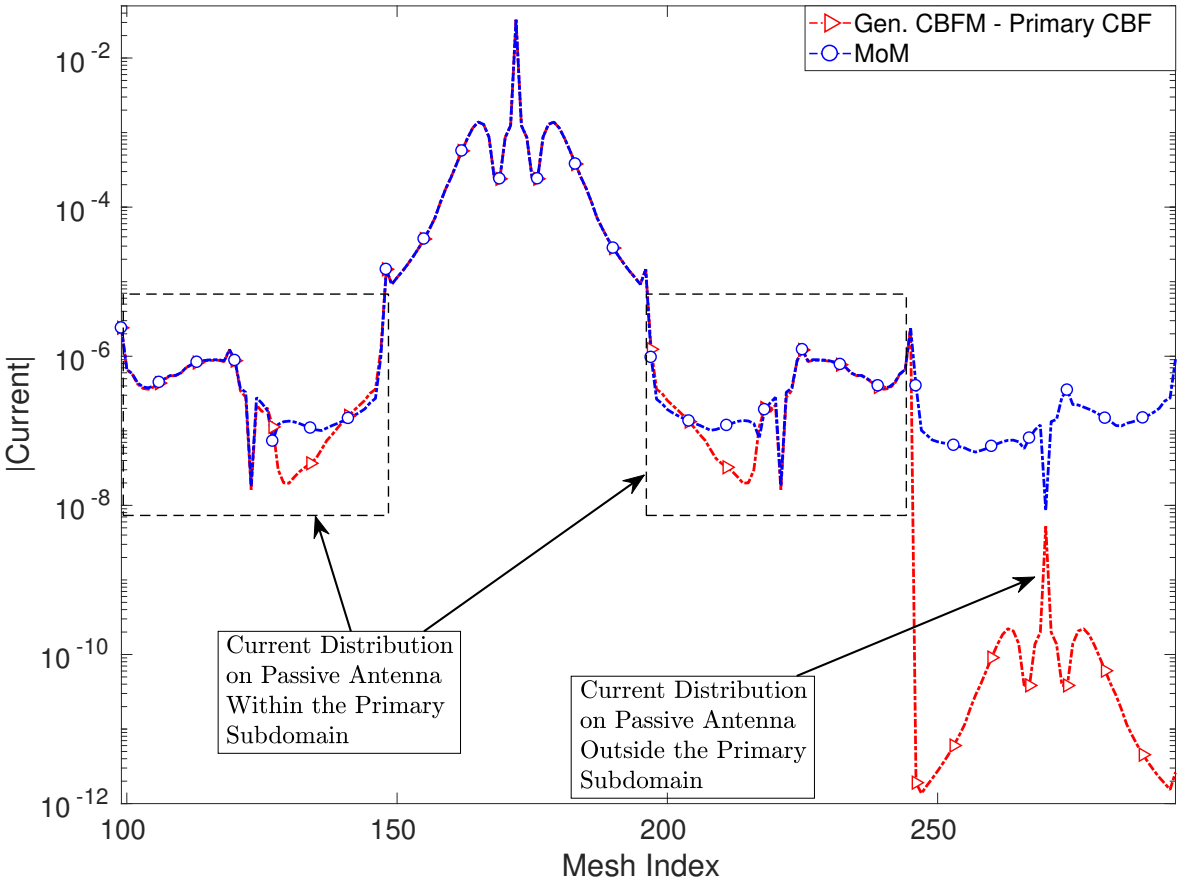

Figure 5.2: Comparison of current distribution on a linear array of 10 antenna elements where only the 4-th antenna is active using primary CBFs with subdomain radius of D and MoM. Only the 3-rd to 6-th antenna is shown.

5.3 Larger Subdomain Secondary CBFs

To improve the accuracy of the solver, secondary CBFs within the pre-defined radius of influence are included similarly as in Chapter 4. From the definition of secondary CBFs in CBFM, the primary current is imposed on a source domain and is allowed to be radiated onto an observer domain within the radius of influence, and the induced current is the secondary CBF. If the same definition is extended to CBFM with subdomain radius D, the schematic is as shown in Figure 5.3(a).

In Figure 5.3(a), a linear antenna array is shown, where each circle represents an antenna element and the dotted line indicates a subdomain. The arrows refer to the field being radiated onto the observer domain due to the impressed primary current on the source domain. The same linear array is shown in two different columns where the left and right columns are the source and observer domain respectively.

Antennas 2 and 3 are present both in the source and observer domain in Figure 5.3(a). Antenna 2 is the active antenna in the primary domain and is also duplicated in the secondary (observer) domain. The presence of the active antenna source in the observer domain creates an induced current which still represents the primary excitation effect, rather than a coupling effect. To mitigate this problem, the common active antenna element is removed from the observer domain as shown in Figure 5.3(b).

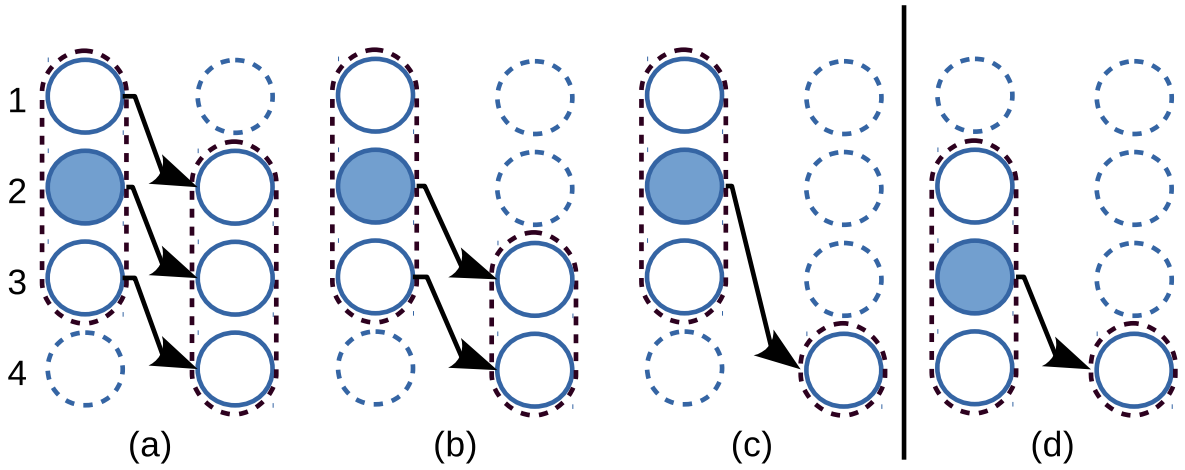

Figure 5.3: Larger subdomain secondary CBFs

The radiated field from the source to observer domain in Figure 5.3(b) can be expressed in a block matrix equation as

$$-\begin{bmatrix} Z_{31} & Z_{32} & Z_{33} \\ Z_{41} & Z_{42} & Z_{43} \end{bmatrix} \begin{bmatrix} I_{p1} \\ I_{p2} \\ I_{p3} \end{bmatrix} = \begin{bmatrix} 0 \\ E \end{bmatrix}. \tag{5.2}$$

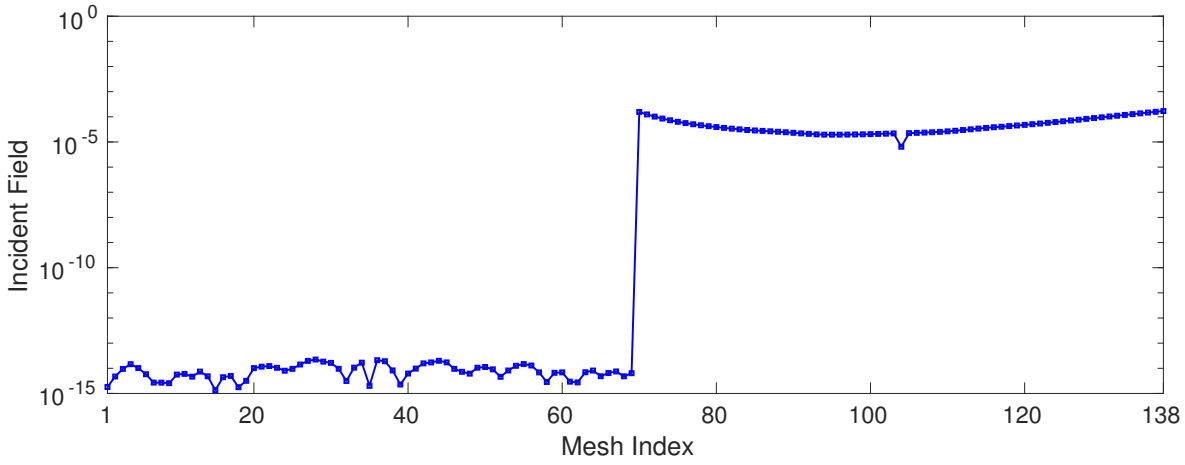

Figure 5.4: Incident field onto secondary domain

Since by the definition of the primary subdomain, only antenna 2 (in Figure 5.3(b)) in the array is active, the incident field onto antenna 3 is a zero vector field as in (5.2). Meaning that the field from the source domain is directed only on the fourth antenna element in Figure 5.3(b). Figure 5.4 is a graph of the incident field onto the observer subdomain. As described in (5.2), no field is incident on the common antenna.

Using the inversion property of block 2×2 matrix [37], the induced secondary current on the observer domain is expressed as

$$\begin{aligned}\begin{bmatrix} I_{s1} \\ I_{s2} \end{bmatrix} &= - \begin{bmatrix} Z_{33} & Z_{34} \\ Z_{43} & Z_{44} \end{bmatrix}^{-1} \begin{bmatrix} 0 \\ E \end{bmatrix} \\ &= - \begin{bmatrix} -Z_{33}^{-1} Z_{34} (Z_{44} - Z_{43} Z_{33}^{-1} Z_{34})^{-1} \\ (Z_{44} - Z_{43} Z_{33}^{-1} Z_{34})^{-1} \end{bmatrix} \begin{bmatrix} E \end{bmatrix}.\end{aligned} \tag{5.3}$$

Equation (5.3) shows the coupled reaction between the two antennas on the observer domain. Moreover, the current induced on the common antenna (Antenna 3 in Figure 5.3(b)) corrects the edge error of the primary CBF as discussed in Section 5.2.

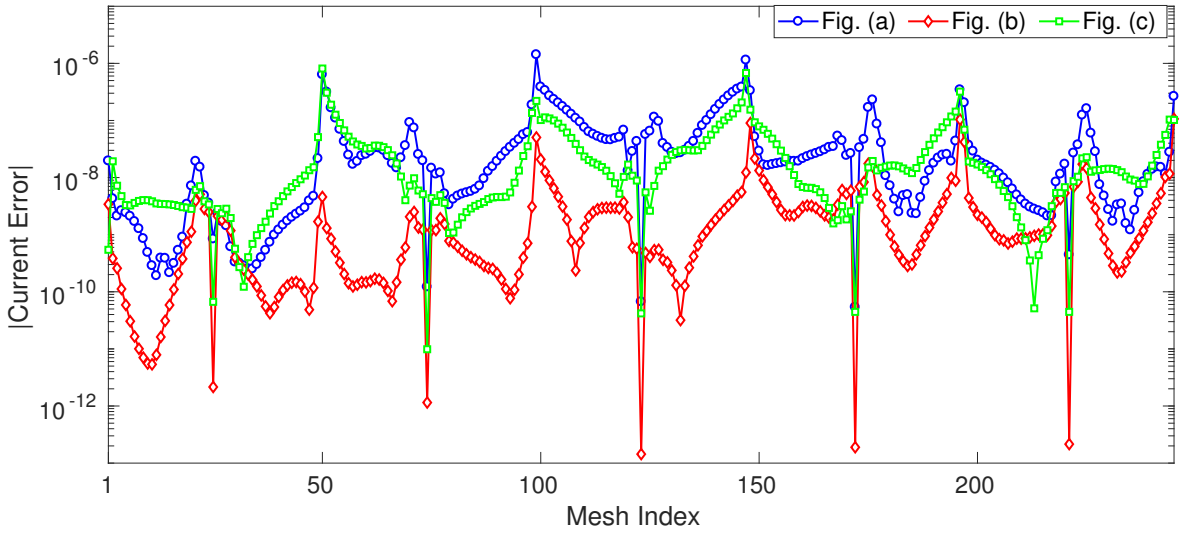

Figure 5.5: Accuracy of secondary CBFs (subdomain radius: D) for setups in Figures 5.3(a)-(c). Setup in Figure 5.3(b) demonstrates the best accuracy.

Figure 5.5 shows the current coefficient error due to the different variants of secondary CBFs discussed for an antenna array of 5 elements where only the first antenna is excited. It is clear that the option in Figure 5.3(b) is the right choice to generate a generalized secondary CBF. A poor accuracy due to the setup in Figure 5.3(a) is due to the presence of the artificial primary current as discussed. As for the secondary CBF in Figure 5.3(c), the absence of an overlapping antenna with the primary prevents any edge correction in the primary domain.

Finally, Figure 5.3(d) shows the secondary CBF due to the pre-edge antenna element using the same definition to generate the generalized secondary CBF as above. However, in this case, the observer domain is entirely overlapped by the source domain. The incident field onto the observer domain is zero, hence a zero vector secondary CBF is obtained, resulting in an ill-conditioned reduced matrix. Thus, all fully overlapped observer domains should be omitted. In other words, the effect is already included in the primary domain and needs not to be repeated. For subdomain radius of D, this happens to be the case only for the pre-edge antenna domain.

To increase the radius of influence, secondary subdomains of the same size are defined on neighbouring antennas. Adjacent secondary domains have an overlapping

antenna as shown in Figure 5.6. In this way, the antennas in the secondary domains are coupled, and every new secondary CBF corrects the edge error in the previous domain.

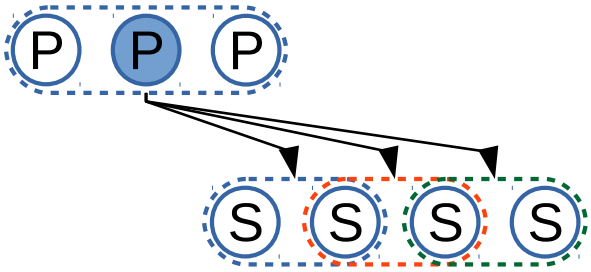

Figure 5.6: Secondary CBFs up to a radius of influence of $3D$; Subdomain radius: D.

The above concept of a secondary CBF for a subdomain radius of D can be extended to larger subdomain radius. For instance, considering a subdomain radius of $2D$ in Figure 5.1(f), the secondary CBF domain size is 3 antenna elements as shown in Figure 5.7. The secondary domain starts on the antenna adjacent to the active one in the primary subdomain and two antenna elements are overlapped in this case.

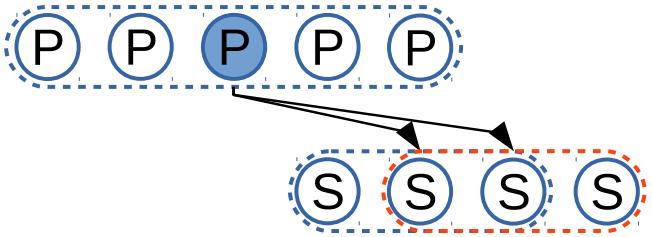

Figure 5.7: Secondary CBFs for subdomain radius: $2D$.

5.4 Larger Subdomain Higher-Order CBFs

Further improvement in accuracy is obtained by increasing the radius of influence, using higher-order CBFs, or a combination of both. Unfortunately, at the expense of an increase in computational cost.

Higher-order CBFs are obtained in a similar way to conventional CBFM, that is by allowing one lower order CBF to radiate onto an observer subdomain. The same size and shape as the secondary CBF have been chosen for higher-order CBFs.

Figure 5.8 shows the generation of a higher-order CBF, e.g., tertiary CBF due to the incident field from a secondary current source. Adjacent subdomains have overlapping antenna similarly as in Section 5.3 (i.e., adjacent primary and secondary subdomains overlap). The sizes of secondary and higher-order CBFs are smaller than primary CBFs for larger subdomain CBFM. For this reason, secondary and higher-order CBFs are zero-padded to be the same size as the primary CBFs, before being clustered together as a CBF group.

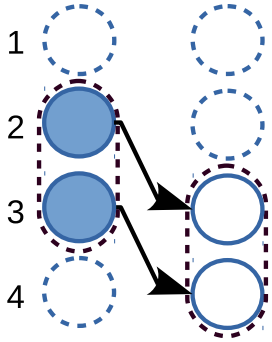

Figure 5.8: Generation of higher-order CBF

5.4.1 Tree like Structure to Generate Higher-Order CBFs

Higher-order CBFs are generated using the tree-like structure as discussed in Chapter 4. Primary CBFs radiate onto adjacent subdomains within a radius of influence to produce two secondary CBFs. Then each secondary CBF is radiated onto its neighbouring domain to produce tertiary CBFs again within the radius of influence. These steps can be repeated to the n-th order. The tree structure for higher-order CBF is demonstrated in Figure 5.9 for subdomain radius 0 and D.

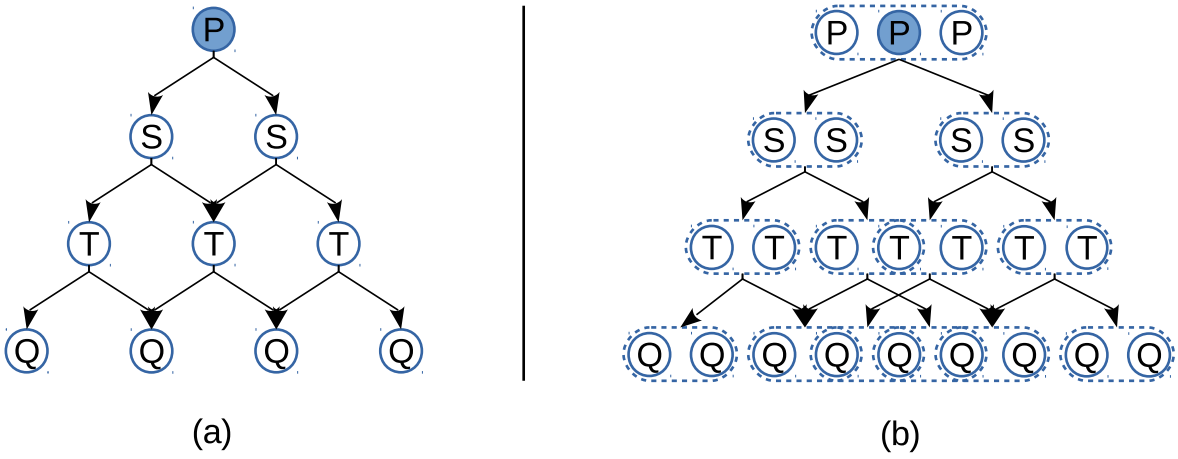

Figure 5.9: Higher-order CBF tree structure for (a) single antenna and (b) large subdomain.

5.5 Rank of Far Interaction Matrices for Larger Subdomain CBFM

The computational cost of a CBFM solver can be separated into 3 steps, namely:

Generation of CBFs

The computational cost in the generation of CBFs increases with the subdomain radius since the interaction matrices, Z_{ii} and Z_{ji} in (4.2) and (4.3) respectively, are

larger. However, in the case of regular array, this step is performed only once, hence is not dependent on the array size.

Creation of reduced matrix

Entries of the reduced impedance matrix are computed by pre and post-multiplying interaction matrices with CBF groups as discussed in Section 4.5. This step is the most computationally expensive part of a CBFM solver. However, when the source and observer subdomain are electrically far apart, the interaction matrix has a low-rank nature. This implies that the interaction can be computed with a lower number of degrees of freedom. The entries of the reduced matrix are often computed using fast low-rank factorization techniques, for instance, using the Adaptive Cross Approximation (ACA) [38] method in [26].

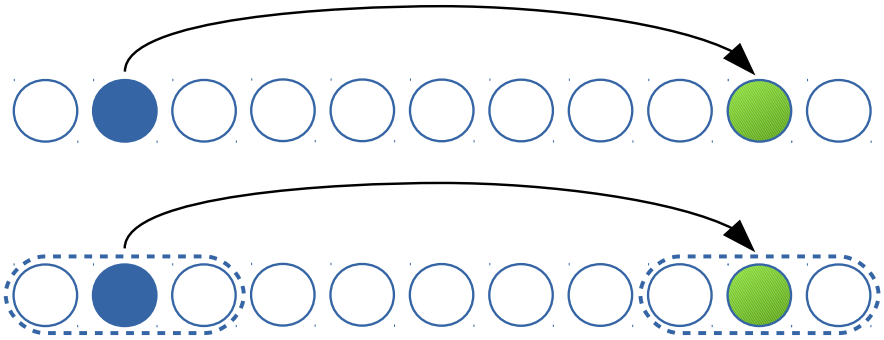

Figure 5.10: Far interaction between source and observer subdomain. Top Figure – Subdomain Radius: 0; Bottom Figure – Subdomain Radius: D.

The interaction between a distant source and observer subdomain is shown in Figure 5.10 for subdomain radius 0 and D. The observer is $8D$ subdomains away from the source subdomain.

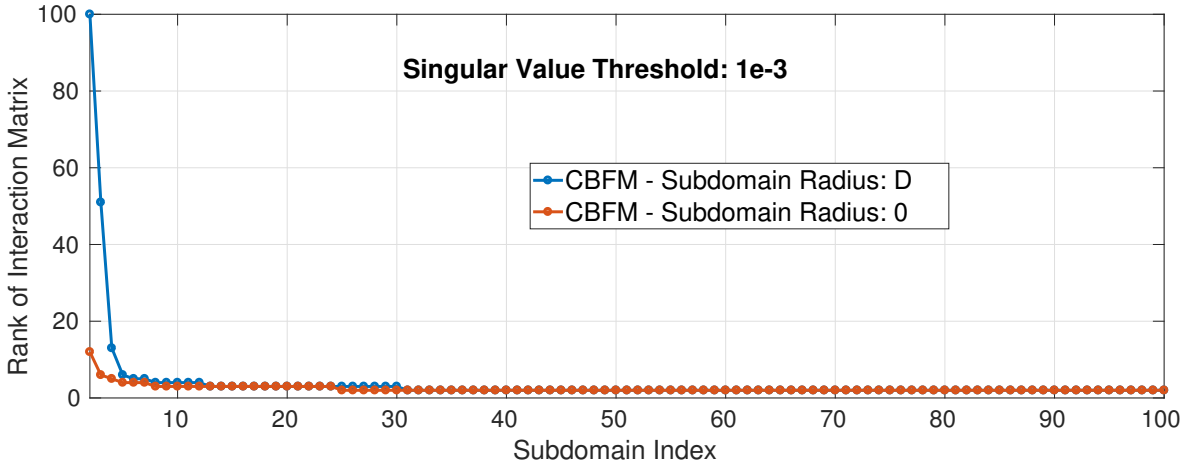

Figure 5.11: Rank of far-interaction impedance matrix.

The rank of interaction matrices, as depicted in Figure 5.10, is shown in Figure 5.11 where the distance between the source and observer subdomain ranges from D to $100D$. The rank is computed numerically using the SVD operation with a threshold value, $\tau = 1^{-3}$, to limit the singular values. Despite that the size of the interaction matrix for a subdomain with a radius of D is $3N \times 3N$ instead of $N \times N$ for a subdomain of radius 0, both interaction matrices have the same rank for distant subdomains.

If computed directly with MoM, the computational cost of entries for the reduced impedance matrix increases with the size of the subdomain; however, using a low-rank factorization technique, the increase in cost for this step is not significant.

Solving the reduced matrix

The number of CBFs for the same accuracy is expected to decrease when using a larger subdomain radius (as to be shown in Section 5.6). This implies that the reduced impedance matrix is smaller in size. Hence, a reduction in the computational cost is achieved, which becomes increasingly significant for larger arrays.

5.6 Comparison Between Conventional and Larger Subdomain CBFM

In this section, larger subdomain CBFM is compared to the conventional CBFM. Similar numerical experimentation is performed as in Chapter 4 with the 2D horn antenna's dimensions given in Figure 4.3. However, in this chapter, a linear antenna array of 25 antenna elements is considered instead of 10 antennas since the subdomains generated in this chapter span a larger number of antennas. Only the first antenna element in the array is active. The excitation frequency and the mesh size are still 300 MHz and $\lambda/16$ respectively. The inter-element distance in the array is 0.525λ. A very small inter-element distance is used so as the mutual coupling is strong, for the use of larger overlapping subdomain to be relevant. Moreover, for these subdomains tests, CBFs are not discarded through the SVD operation, and only orthogonalization of the CBFs is performed. This is the case since the aim is to demonstrate the accuracy by varying subdomain radii using all the generated CBFs.

Figure 5.12 shows the current coefficient error throughout the array using only secondary CBFs with a radius of influence D, that is, only 3 CBFs at most per subdomain. The 3 traces in Figure 5.12 correspond to subdomain radii ranging from 0 to $2D$ (labeled as S.R. in the graph). A direct relation between increasing the subdomain radius and the accuracy of the solution can be noted.

The same remark regarding accuracy can be made when tertiary CBFs are included in Figure 5.13. Tertiary CBFs have been generated within a radius of influence of D. The results presented in Figure 5.12 and 5.13 are shown again in Table 5.1 and 5.2 respectively. The number of CBFs used to model the 25 antenna array, and the corresponding current errors are shown for the subdomain radius ranging from 0 to $2D$. With approximately the same size of reduced impedance matrix, a lower current error can be achieved using larger overlapping subdomains. Larger subdomain uses slightly less CBFs for the same order because fully overlapped CBFs are not included as discussed in Section 5.3.

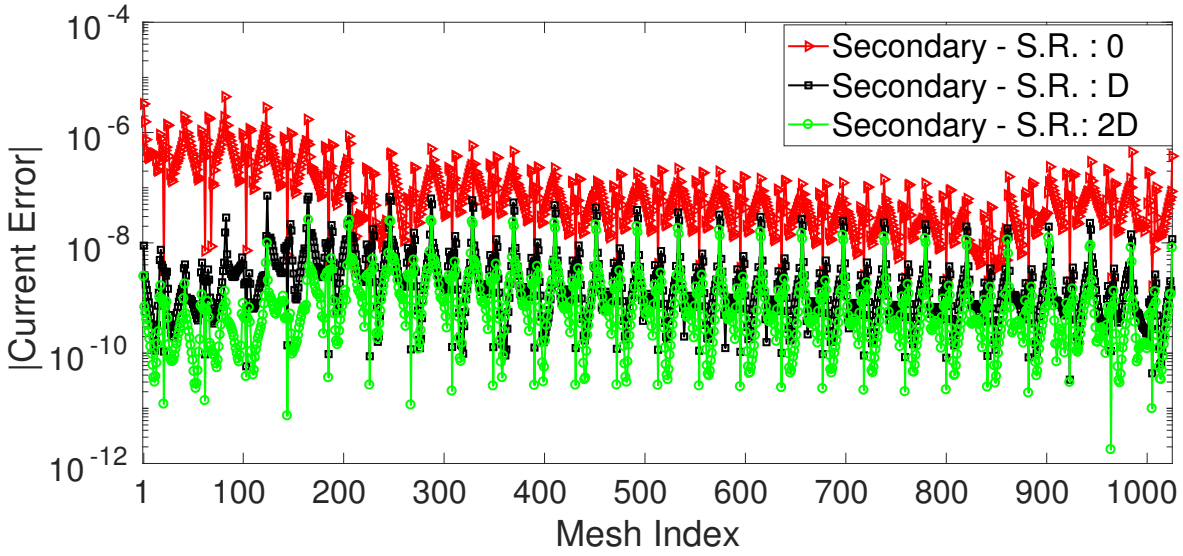

Figure 5.12: Current coefficient errors using up to secondary CBFs. Subdomain radius varies from 0 to $2D$

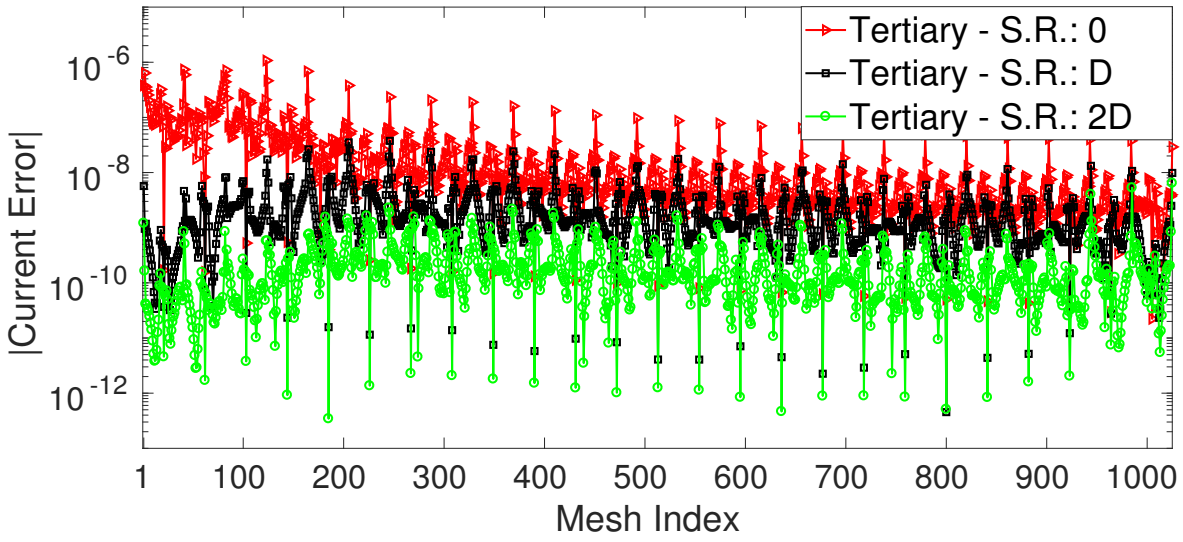

Figure 5.13: Current coefficient errors using up to tertiary CBFs. Subdomain radius varies from 0 to $2D$

5.7 Conclusion

In this chapter, the idea of using larger overlapping subdomains to generate CBFs has been explored. The numerical results show that increasing the subdomain radius improves the accuracy of the solver for roughly the same number of CBFs used. To generate higher-order CBFs, the tree-like structure has been used in the chapter. The shortcomings of the tree-like structure are to be discussed in the next chapter and solutions are proposed.

Subdomain Radius	Radius of Influence	CBF Order	Reduced Matrix Size	Current Error (ϵ)
0	D	Secondary	75	3.3461e−04
D	D	Secondary	71	8.7730e−06
$2D$	D	Secondary	69	3.6075e−06

Table 5.1: Current errors and reduced matrix sizes for varying subdomain radii using up to secondary CBFs. The dimensions of the full MoM matrix is 1025.

Subdomain Radius	Radius of Influence	CBF Order	Reduced Matrix Size	Current Error (ϵ)
0	D	Tertiary	175	8.0619e−05
D	D	Tertiary	161	4.0521e−06
$2D$	D	Tertiary	153	4.6044e−07

Table 5.2: Current errors and reduced matrix sizes for varying subdomain radii using up to tertiary CBFs. The dimensions of the full MoM matrix is 1025.

Chapter 6

Distance-Based Criterion to Generate Higher-Order CBFs

6.1 Introduction

In Chapters 4 and 5, the tree structure for generation of higher-order CBFs has been discussed. In this chapter, the shortcomings of the tree structure are outlined, and the distance-based criterion for a more efficient generation of higher-order CBFs is proposed.

6.2 Shortcomings of Tree Structure for Higher-Order CBFs

The outer tertiary CBFs in the tree structure, as shown in Figure 6.1(b), add little or no contribution to the accuracy unless the corresponding secondary CBFs are included on the same subdomains (as in Figure 6.1(c)).

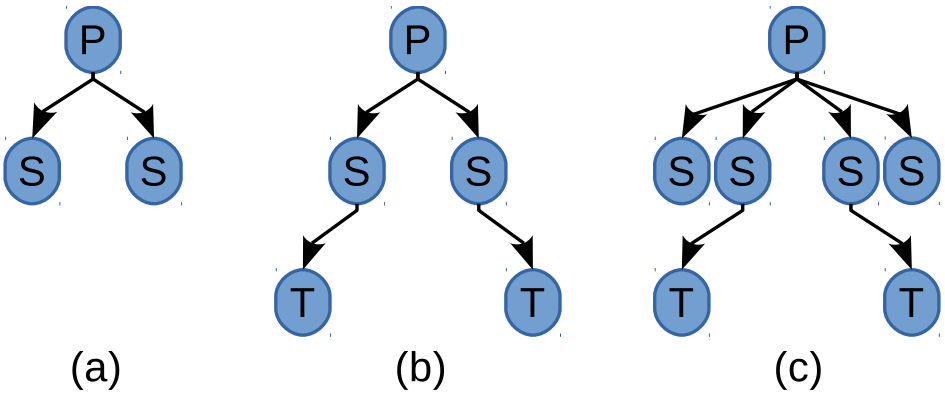

Figure 6.1: Representation of setups for test case.

To demonstrate the shortcomings of the tree structure for higher-order CBFs, current distribution for an antenna array is solved using the test cases as in Figure 6.1. In Figure 6.1(a), each domain consists of only a primary and two secondary CBFs.

Tertiary CBFs are also included in Figure 6.1(b), however, the inner tertiary CBFs in the tree structure from Figure 5.9 are not included so as only the effect of the outer higher-order CBFs can be observed. Finally, in Figure 6.1(c), secondary CBFs are included in each subdomain where outer tertiary CBFs reside. That is, a secondary CBF with a radius of influence $2D$. Only a single antenna subdomain is depicted in Figure 6.1 for visual simplicity; however the concept is also applied to subdomain radius D in Figure 6.1.

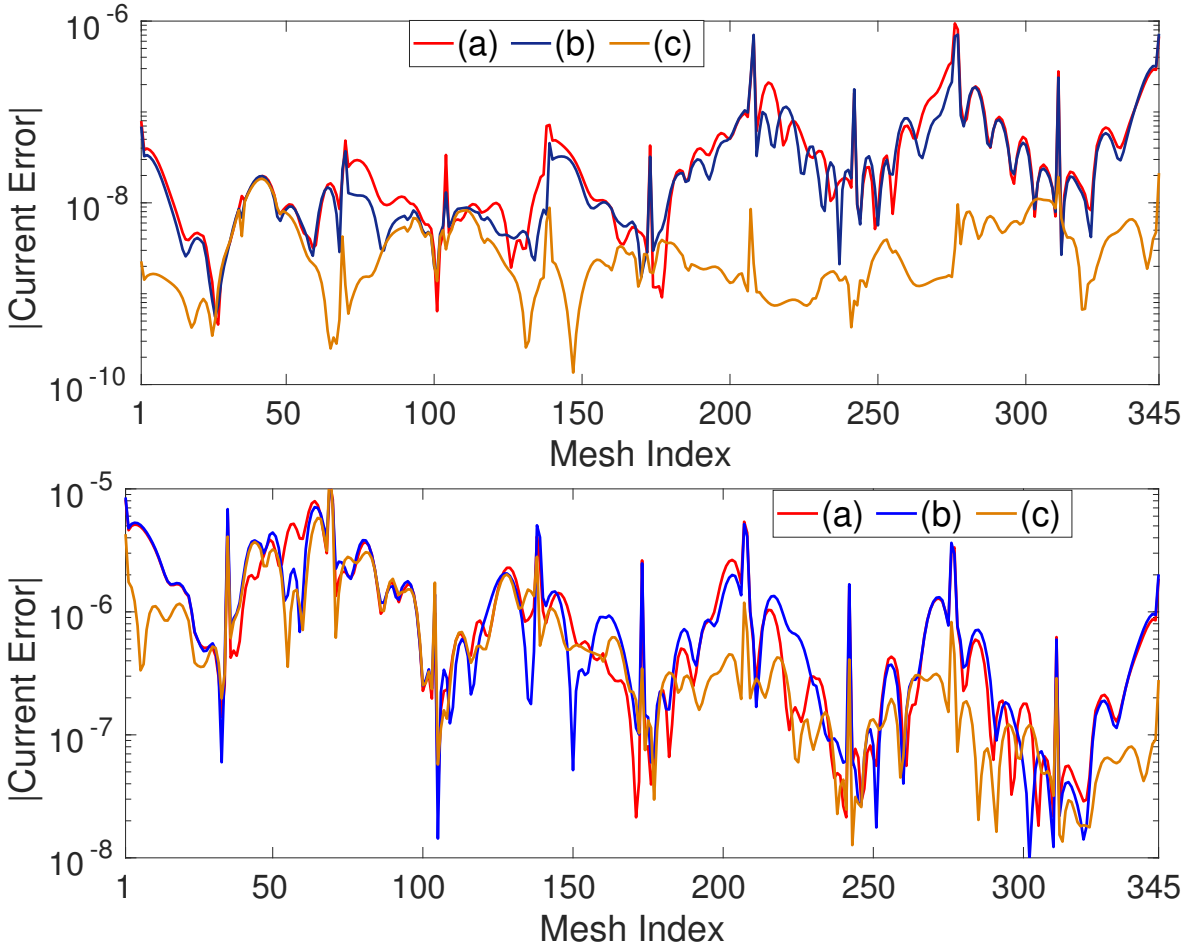

Figure 6.2: Current coefficient errors due to CBFM setups in Figure 6.1. Top Figure – Subdomain Radius: D; Bottom Figure – Subdomain Radius: 0.

The current coefficient error in a linear antenna array is depicted in Figure 6.2 due to CBFs generated per subdomain as in Figure 6.1. On the top graph, the current coefficient errors due to CBFs of subdomain radius D are shown. It can be seen that the current coefficient error using test cases (a) and (b) from Figure 6.1 are nearly identical, thus the additional outer tertiary CBFs have no contribution regarding accuracy unless the corresponding secondary CBFs are included in the domain as in test case (c). The significant difference in accuracy betweem the test case (b) and (c) explains why the tree structure for higher-order CBFs is inefficient. For the case of single antenna subdomain (on the bottom graph), the difference in accuracy between test cases (b) and (c) is

less significant. Thus the tree structure is more problematic for larger overlapping subdomains.

The inclusion of both secondary (radius of influence $2D$) and tertiary CBFs on the outer tertiary subdomains can be further supported by the results in Figure 6.3, which show the incident fields onto an outer tertiary subdomain by (a) primary CBF with distance $2D$, (b) secondary CBF with distance D, and finally (c) superposition of the primary and secondary fields. Graph (c) has a similar profile to that in Figure 5.4, that is the incident field is only directed onto the non-common antenna in the tertiary subdomain, and thus, the common antenna in the subdomain cater for the edge correction in the adjacent secondary CBF. This is not achieved when only primary or secondary field is incident onto the outer tertiary subdomain as shown in Figure 6.3.

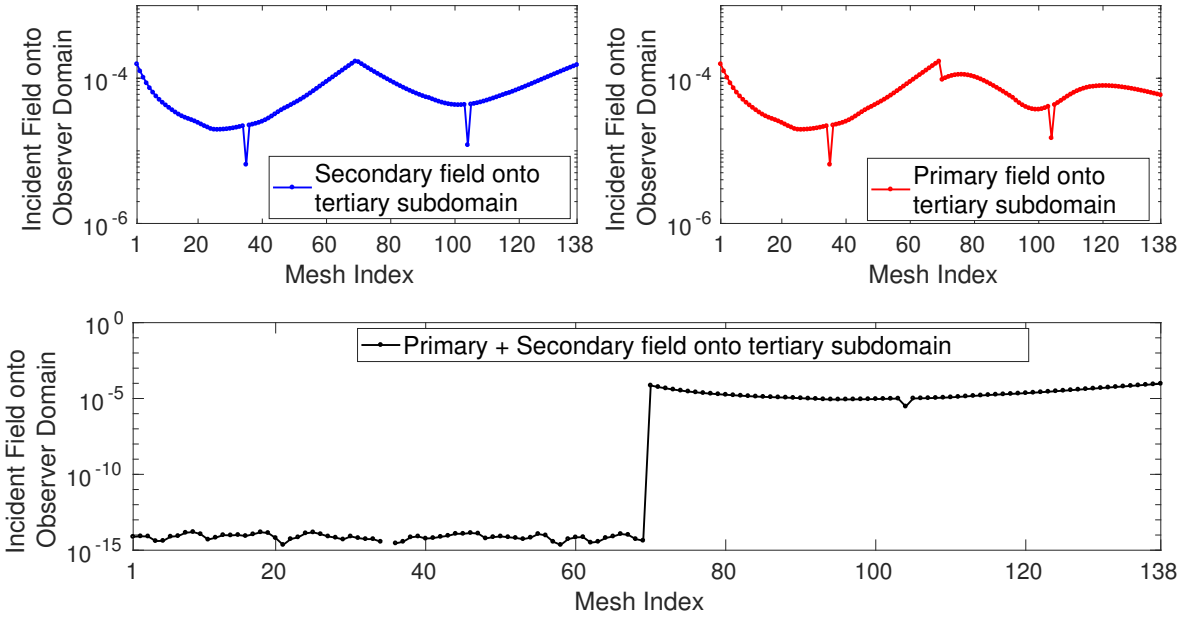

Figure 6.3: Incident fields onto a tertiary subdomain.

The test scenarios in Figure 6.1 are now considered for CBFM with subdomain radius $2D$ as shown in Figure 6.4. A larger antenna array is used compared to the one in Figure 6.2 since the subdomains span over a maximum number of 5 antennas. Similar result to that of subdomain radius D is achieved, that is the inclusion of outer tertiary CBFs does not improve the accuracy unless the corresponding secondary CBFs are included on that domain.

The incident field onto the tertiary subdomain is shown in Figure 6.5. Since the subdomain which is a distance of $2D$ from the primary CBF has a common antenna element as shown in Figure 5.7, the field is directed only onto the last two antennas in the domain.

For subdomain with a distance of $3D$ away from the primary CBF, no common antenna is present. Regarding the incident field onto the tertiary subdomain, similar observation can be made as in Figure 6.3. Individually primary and secondary fields are incident on all the antennas on the subdomain. However, the superposition of the

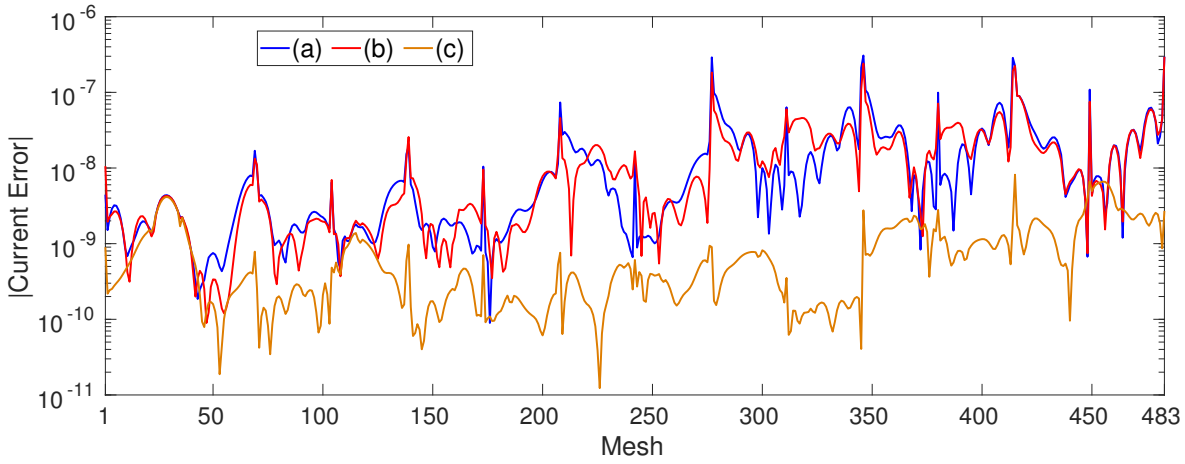

Figure 6.4: Current coefficient errors due to CBFM setup in Figure 6.1. Subdomain Radius: $2D$.

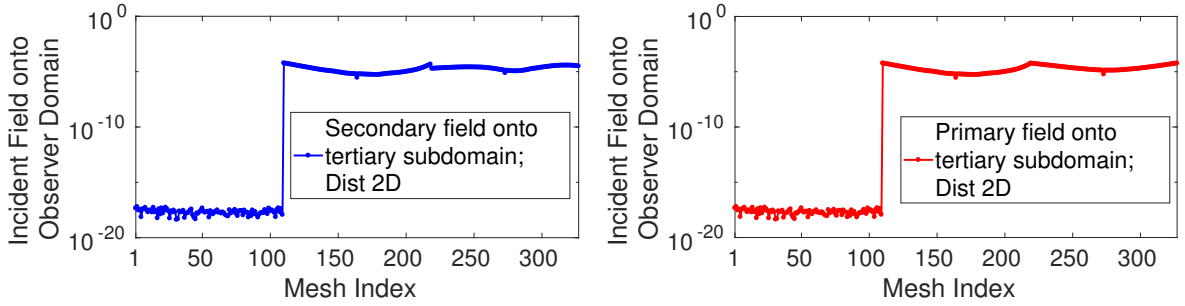

Figure 6.5: Incident field onto tertiary subdomain.

fields is directed only onto the last antenna. The two common antennas provide an edge correction to the previous subdomain.

6.3 Distance-Based Criterion to generate Higher-Order CBFs

From Section 6.2, it is evident that a secondary CBF needs to be present on the outer tertiary CBF subdomain. Figure 6.7 shows the most comprehensive interaction for generation of higher-order CBFs to approach the MoM solution within a radius of influence. Tertiary CBFs due to only one secondary CBF is shown in the diagram for visual simplicity. From Figure 6.7, it is clear that the most comprehensive interaction will lead to the generation of a large number of higher-order CBFs thus making the solver unpractical.

Alternatively, higher-order CBFs can be generated by a **distance-based criterion** procedure as in Figure 6.8.

- A **maximum radius of cumulative influence** is pre-defined, which is a radius of $3D$ for the case of Figure 6.8. Field due to the primary CBF is allowed to be radiated up the maximum cumulative influence directly or indirectly.

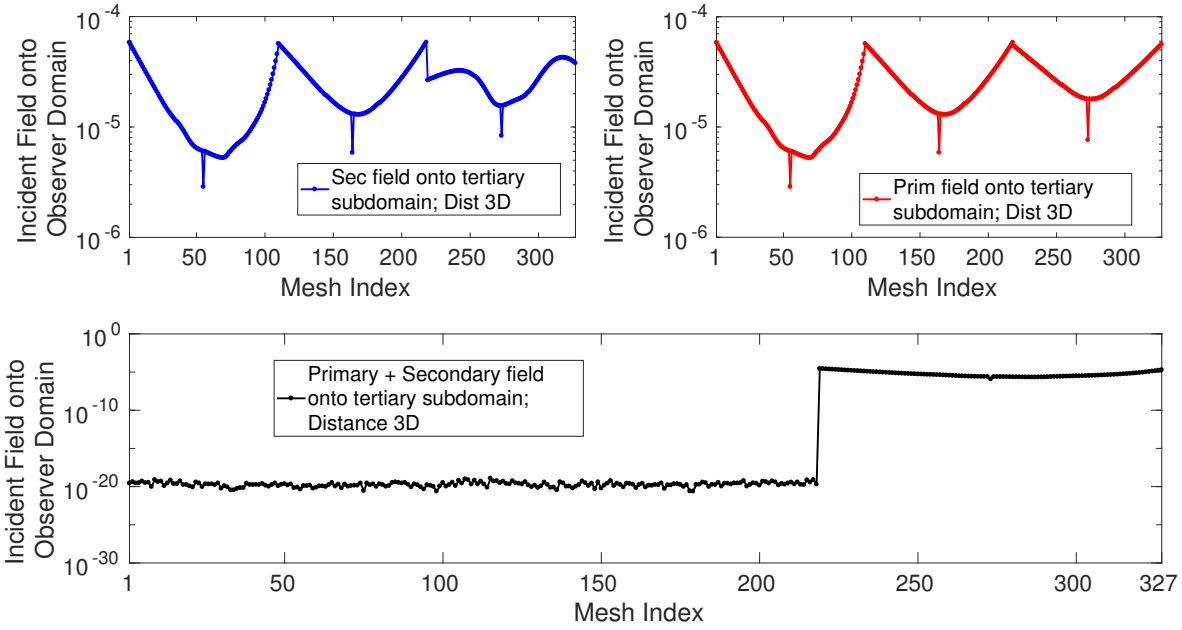

Figure 6.6: Incident field onto tertiary subdomain.

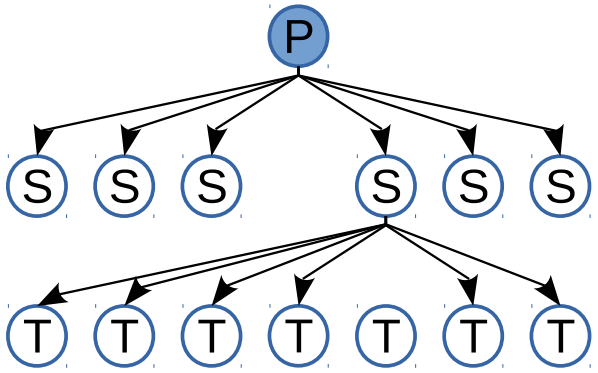

Figure 6.7: Most comprehensive interaction tree due to a secondary CBF.

- Secondary CBFs are defined up to the radius of $3D$. The secondary CBF which is at a distance $3D$ from the primary CBF (Blue arrow in Figure 6.8) cannot be radiated to produce tertiary CBFs. However, secondary CBF away from the primary domain by D and $2D$ are allowed to radiate.

- The secondary CBF which is a distance of D away from the primary CBF can further be radiated up to a maximum distance of $2D$ (Red arrows in Figure 6.8) directly to produce a tertiary CBFs or indirectly as a quaternary CBFs.

- As for the secondary CBF located at a distance of $2D$ from the primary CBF, the former can radiate to produce a tertiary CBF distance D away, as shown with the green arrow in Figure 6.8.

As the radius of influence is increased, the highest order of CBF included is also increased to accommodate all possible combinations within the cumulative radius of

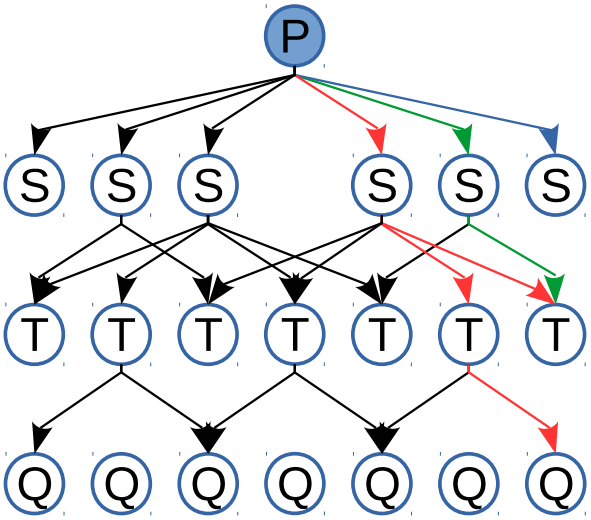

Figure 6.8: Distance-based criterion for higher-order CBFs.

influence. In this procedure, a lower order CBF is always present on the outer subdomain (e.g., Secondary CBF present on the outer tertiary subdomain) as discussed in Section 6.2.

6.4 Comparison of Single Antenna and Larger Subdomain CBFM Using Distance-Based Criterion

In this section, CBFM solvers with different subdomain radii are compared similarly as in Section 5.6, however, the distance-based criterion is used to generate tertiary CBFs instead of the tree structure.

The results from the tree structure and distance-based criterion are compared in Figure 6.9 and Table 6.1. The significant improvement in accuracy for both subdomain radii of D and $2D$ can be noticed due to the inclusion of secondary CBFs on the subdomain of outer tertiary CBFs corresponding to the discussion in Section 6.2. An insignificant improvement is obtained for the case subdomain radius 0. As shown in Figure 6.2, the tree structure for higher-order CBFs is less problematic for single antenna subdomain.

Moreover, in Table 6.1, an increase in the number of degrees of freedom is also noted while using the distance-based criterion. However, no CBF has been discarded through the SVD operation in this numerical experimentation since the aim was to demonstrate the difference compared to the tree structure by using all the generated basis functions.

The current coefficient errors for CBFM using up to quaternary CBFs generated through the distance-based criterion is shown in Figure 6.10 for subdomain radius 0 and D, where no CBF has been discarded during the SVD operation. The results are not compared to the tree structure since a very large number of CBFs would be required to have similar accuracy to that of the larger subdomains, up to quaternary CBFs solver.

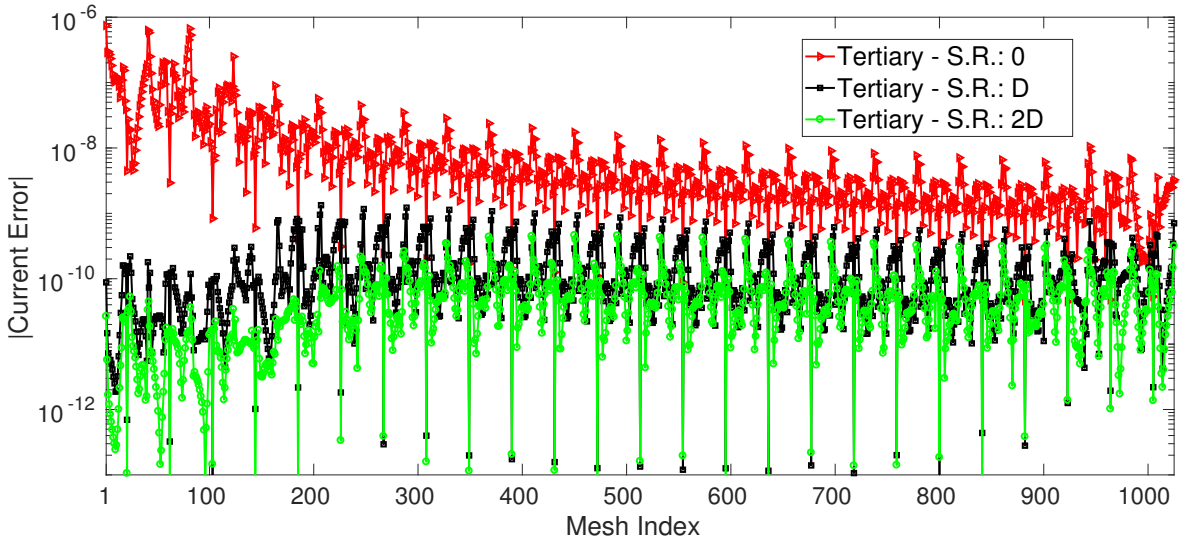

Figure 6.9: Current coefficient errors for test cases presented in Table 6.1. Higher-order CBFs are generated using distance-based criterion.

	Tree Structure Radius of Influence: D Highest Order: Tertiary		Distance-Based Criterion	
Subdomain Radius	Reduced Matrix Size	Current Error (ϵ)	Reduced Matrix Size	Current Error (ϵ)
0	175	8.0619e-05	213	5.8493e-05
D	161	4.0521e-06	205	2.4788e-07
$2D$	153	4.6044e-07	197	8.9971e-08

Table 6.1: Dimensions of reduced matrices for different subdomain radii. The dimensions of the full MoM matrix is 1025.

The sizes of the reduced matrix and the CBFM current errors are presented in Table 6.2. The results where an SVD threshold value of 1.0^{-6} is applied are also shown in Table 6.2.

Subdomain Radius	CBF Order	τ	Reduced Matrix Size	Current Error (ϵ)
0	Quaternary	-	621	2.6213e−06
D	Quaternary	-	595	2.2579e−09
0	Quaternary	1.0^{-6}	401	4.0211e−06
D	Quaternary	1.0^{-6}	467	3.1568e−09

Table 6.2: Dimensions of reduced matrices for different subdomain radii. The dimensions of the full MoM matrix is 1025.

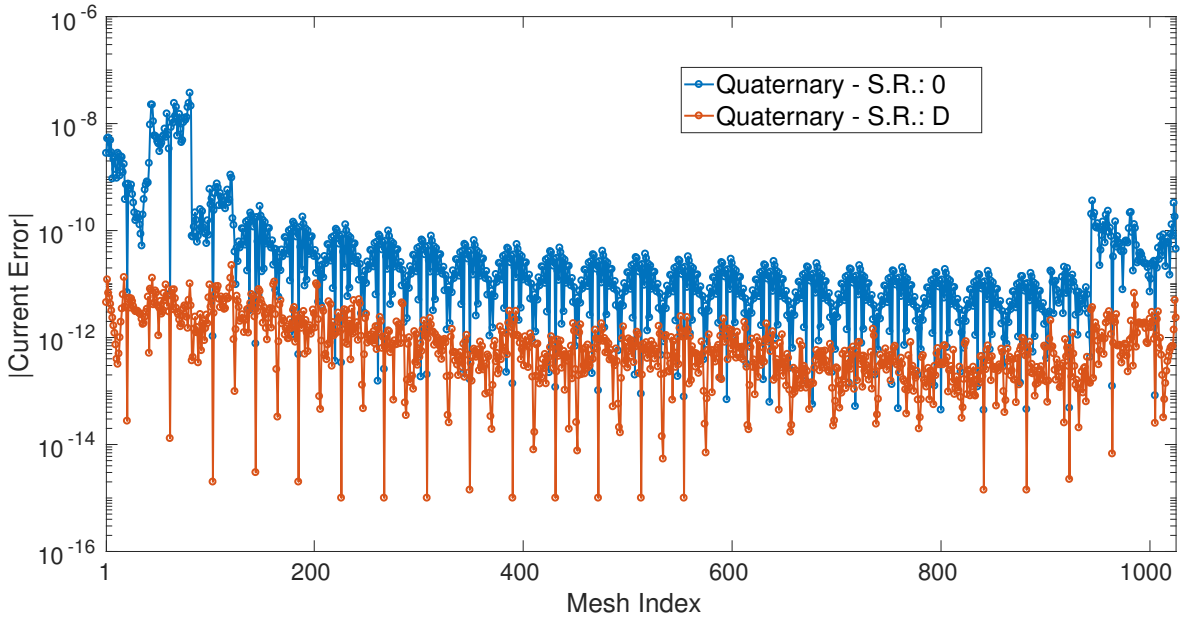

Figure 6.10: Current coefficient errors for up to quaternary CBFs using distance-based criterion

6.5 Conclusion

In this chapter, the shortcoming of the tree structure to generate higher-order CBFs has been discussed. In this respect, the distance-based criterion has been proposed as a general scheme to address the shortcoming and compared to the tree structure regarding accuracy.

Chapter 7

Numerical Results

7.1 Introduction

In this chapter, numerical results regarding the CBFM variants discussed throughout this thesis namely, single antenna subdomain, larger subdomain, tree-like structure and distanced-based criterion are presented and compared. The SVD threshold is applied to limit the number of basis functions. The radius of influence, the order of CBFs and subdomain radius are varied throughout the numerical experiments. Moreover, results are presented over a range of frequencies and the inter-element distance is also varied.

7.2 Numerical Test: 1

7.2.1 Inter-Element Distance: 0.525λ

In this numerical experiment, current over an antenna array of 25 elements where only the first element is excited is solved. The current coefficient errors graph using different techniques and parameters are as shown as in Figure 7.1. The parameters used for the three graphs are given in Table 7.1. The graphs (a) and (b) in Figure 7.1 use a subdomain radius of D and higher-order CBFs are generated using the distance-based criterion. The maximum cumulative radius of influence used for (a) and (b) are $2D$ (up to tertiary) and $3D$ (up to quaternary) respectively. Graph (c) is due to CBFM with single antenna subdomain, higher-order basis functions are generated up to quaternary CBFs within a radius of influence of $3D$ using the tree structure.

Up to quaternary CBFs and a radius of influence of $3D$ is highly unpractical to be used in a CBFM solver since the number of CBFs generated is roughly equal to the number of the low-order basis functions. However, the number of CBFs is drastically reduced after the SVD operation. That is, only the most significant CBFs are kept from all the possible order of CBFs within the sufficiency large radius of influence. Thus, this parameter has been used only for comparison sake to larger subdomain radius and not for computational efficiency.

Using larger subdomain with distance-based criterion, it is evident that a much better accuracy can be obtained with fewer number of CBFs, referring to Table 7.1.

Case (d) is added to Table 7.1, where the threshold value of case (c) is lowered from 1.0^{-5} to 1.0^{-6}. From Table 7.1, it can be seen that similar accuracy to compared to (a)

	Subdomain Radius	HO CBFs Structure	Radius of Influence	CBF Order	τ	Red. Mat. Size	Current Error (ϵ)
(a)	D	Distance Based	$2D$	Ter	1.0^{-6}	159	9.7930e−07
(b)	D	Distance Based	$3D$	Quad	1.0^{-6}	243	5.5993e−07
(c)	0	Tree Structure	$3D$	Quad	1.0^{-5}	325	8.6688e−06
(d)	0	Tree Structure	$3D$	Quad	1.0^{-6}	425	1.2331e−06

Table 7.1: Current coefficient errors and reduced matrix sizes for test cases (a) to (d). The dimension of the full MoM matrix is 1025. Inter-element space: 0.525λ

is achieved, however, at the expense of a larger reduced impedance matrix. Number of CBFs used in case (a) is 15.5% of that of the total number of low-order basis functions while being 41.4% for the case (d) to provide similar accuracy.

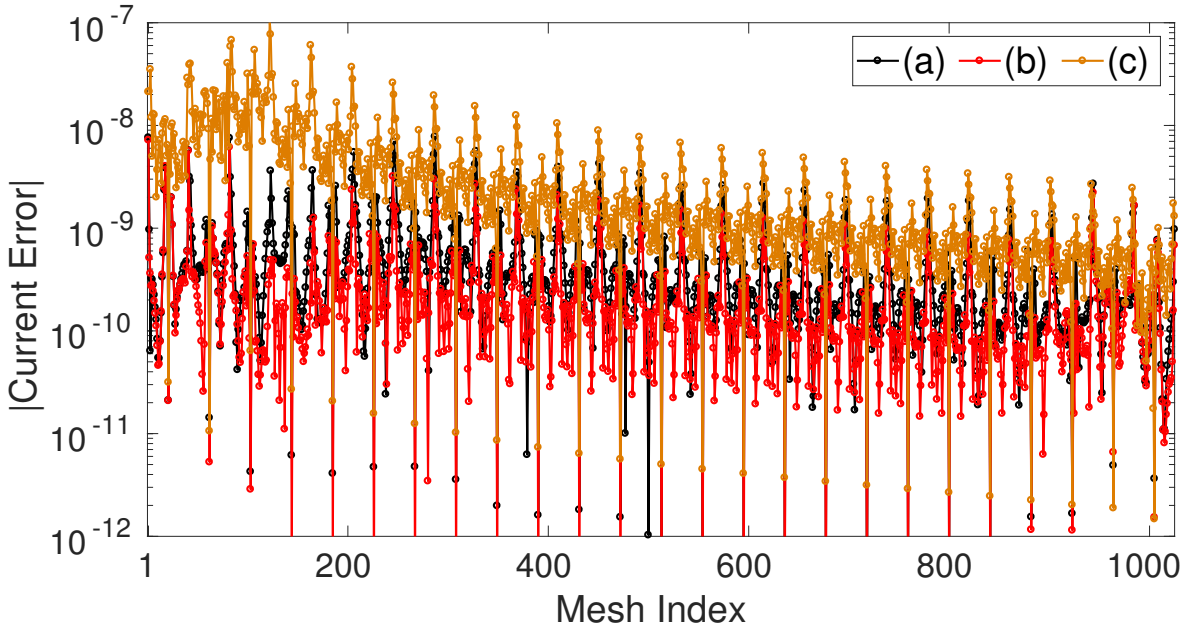

Figure 7.1: Graph of current coefficient errors for test cases (a) to (c). Parameters of test cases are given in Table 7.1.

In Tables 7.1, 7.2 and 7.3 a smaller value for SVD threshold (by one order of magnitude) is used for larger subdomain CBFM compared to that of a single antenna subdomain. Figure 7.2 shows the normalized singular value for CBFs of subdomain radius 0 and D. For both traces, up to quaternary CBFs has been generated through the distance-based criterion. It can be noticed in Figure 7.2, that the graph corresponding to a subdomain radius D has a steeper slope, thus being the reason for using a smaller value for SVD threshold.

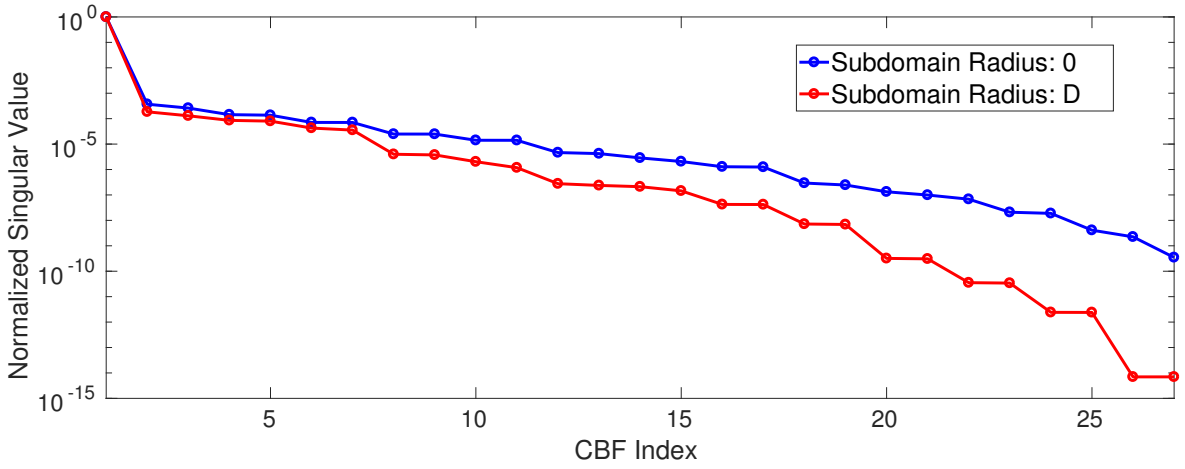

Figure 7.2: Normalized singular values of CBFs for subdomain radii 0 and D.

	Subdomain Radius	HO CBFs Structure	Radius of Influence	CBF Order	τ	Red. Mat. Size	Current Error (ϵ)
(a)	D	Distance Based	$2D$	Ter	1.0^{-5}	115	5.7512e−06
(b)	D	Distance Based	$3D$	Quad	1.0^{-5}	138	5.3893e−06
(c)	0	Tree Structure	$3D$	Quad	1.0^{-4}	100	5.4974e−05
(d)	0	Tree Structure	$3D$	Quad	1.0^{-5}	175	8.5975e−06

Table 7.2: Current coefficient errors and reduced matrix sizes for test cases (a) to (d). The dimension of the full MoM matrix is 1025. Inter-element space: 1.5λ

7.2.2 Inter-Element Distance: 1.5λ

The inter-element distance in the array is increased to 1.5λ so as mutual coupling among antenna elements is less critical. In Figure 7.3, a similar observation to that relating to Figure 7.1 can be made, that is, a higher accuracy can be obtained using larger domain CBFM. The parameters, sizes of the reduced matrix and CBFM current errors for the different test cases are presented in Table 7.2. A larger SVD threshold value has been found more appropriate to be used since the coupling among antennas is less. Referring to Table 7.2, similar accuracy can be obtained using test case (a) and (d), while the number of CBFs used are 11.2% and 17.1% respectively to that of the low-order basis functions. The reduction in the number of CBFs while using larger subdomain CBFM is less significant as the inter-element distance in the array increases.

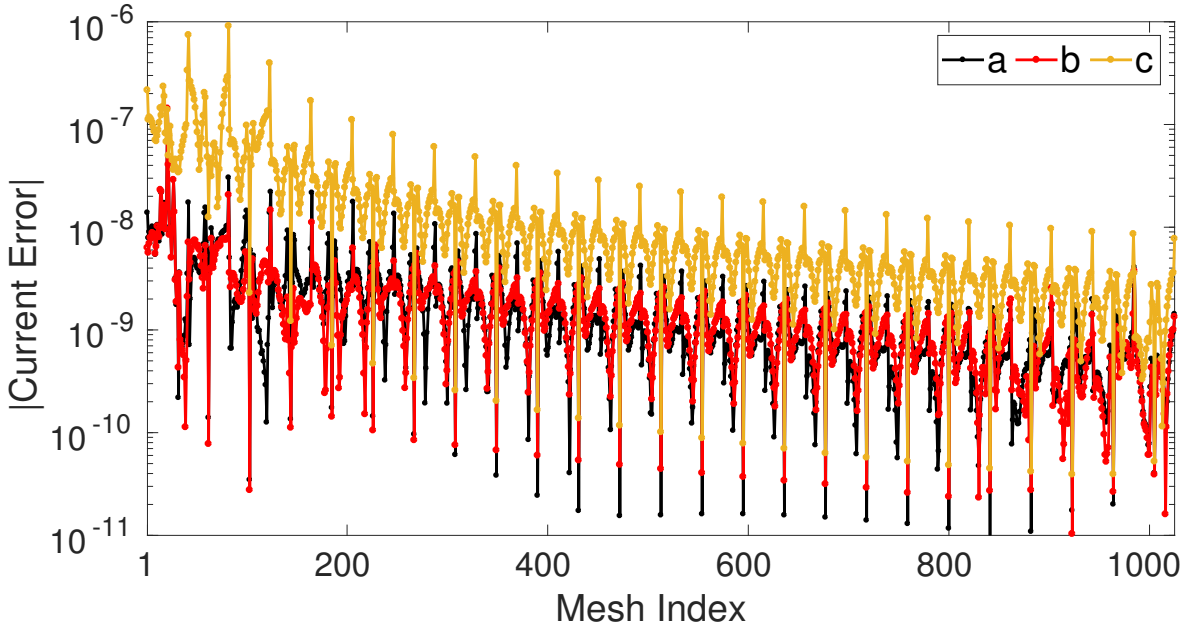

Figure 7.3: Graph of current coefficient errors for test cases (a) to (c). Parameters of test cases are given in Table 7.2.

	Subdomain Radius	HO CBFs Structure	Radius of Influence	CBF Order	τ	Red. Mat. Size	Current Error (ϵ)
(a)	D	Distance Based	$2D$	Ter	1.0^{-5}	115	8.2307e−06
(b)	D	Distance Based	$3D$	Quad	1.0^{-5}	157	7.2428e−06
(c)	0	Tree Structure	$3D$	Quad	1.0^{-4}	125	3.8874e−05
(d)	0	Tree Structure	$3D$	Quad	1.0^{-5}	225	4.8012e−06

Table 7.3: Current coefficient errors and reduced matrix sizes for test cases (a) to (d). The dimension of the full MoM matrix is 1025. Inter-element space: λ

7.2.3 Inter-Element Distance: λ

The reduced matrix sizes and CBFM current errors for different parameters are presented in Table 7.3 for inter-element distance of λ. The graph is omitted to avoid repetition since it has a similar profile to that of Figures 7.1 and 7.3. Again, similar accuracy can be obtained using larger subdomain radius. The size of the reduced matrices are 11.2% and 22.0% compared to the full MoM matrix for the test cases (a) and (d) respectively for the same level of accuracy.

	Subdomain Radius	HO CBFs Structure	Radius of Influence	CBF Order	τ	Red. Mat. Size	Current Error (ϵ)
(a)	D	Distance Based	D	Sec	–	71	8.7730e−6
(b)	0	Tree Structure	$2D$	Ter	1.0^{-4}	125	1.0103e−4

Table 7.4: Current coefficient errors and reduced matrix sizes for test cases (a) and (b). The dimension of the full MoM matrix is 1025. Inter-element space: 0.525λ

7.3 Numerical Test: 2

Larger domain CBFM (Subdomain radius: D) uses only 3 CBFs per subdomain to model an array of 25 antennas in this numerical experiment. That is, only secondary CBFs within a radius of influence of D. The result is compared to that of a single antenna subdomain using tertiary CBFs within a radius of influence of $2D$. An SVD threshold value of 1.0^{-4} is used to limit the number of CBFs. The comparison of the current coefficient errors is shown in Figure 7.4, and the two cases are labeled as (a) and (b) respectively. The parameters, sizes of the reduced matrix and current coefficient errors for both cases are presented in Table 7.4. The inter-element distance in the antenna array is 0.525λ. A good accuracy is obtained for case (a) even with a small number of CBFs per subdomain.

Thus, moderately accurate results can be expected to be achieved using only secondary CBFs with large overlapping subdomains.

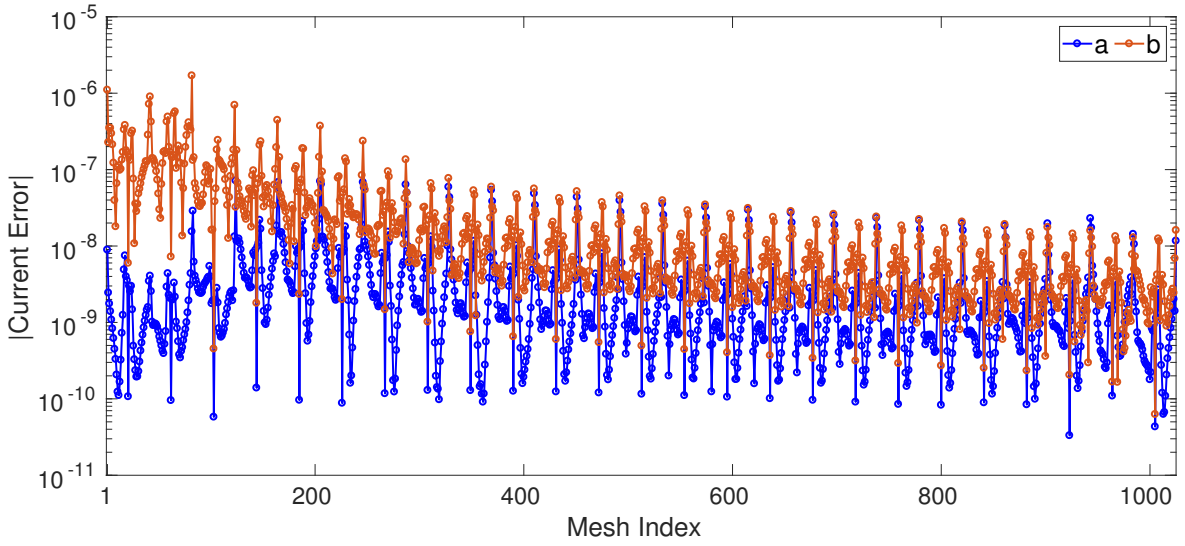

Figure 7.4: Graph of current coefficient errors for test cases (a) to (b). Parameters of test cases are given in Table 7.4.

7.4 Numerical Test: 3

The excitation frequency is varied from 300 MHz to 2000 MHz. The dimensions of the geometry are as shown in Figure 7.5. The dimensions are fixed as opposed to Figure 4.3, where the dimensions are varied with λ. The number of lower-order basis functions in the MoM solver is expected to increase with frequency. The number of antennas in the linear array is 25, and only the first antenna is active.

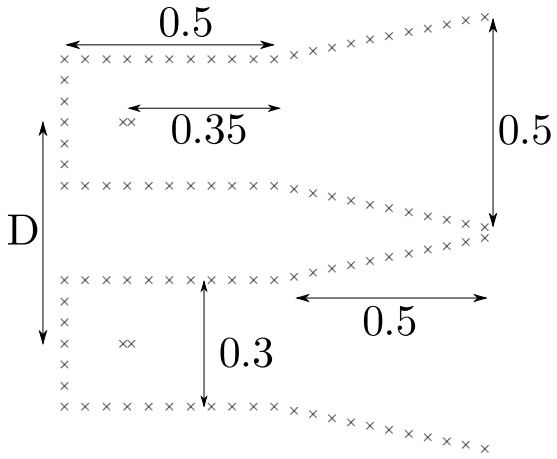

Figure 7.5: Structure of problem to be solved.

7.4.1 Inter-Element Distance: 0.525

In Figure 7.6, the ratio of the number of CBFs to lower-order basis functions is plotted against the excitation frequency for different parameters as elaborated in Table 7.5. The corresponding CBFM current errors, ϵ, across the range of frequencies are shown in Figure 7.7. Cases (a) to (c) correspond to a larger subdomain with the distance-based criterion for higher-orders CBFs whereas (d) and (e) are due to single antenna subdomain with the tree structure. The difference in compression of the reduced impedance matrix between larger and single antenna subdomain is clear in Figure 7.6. At 300MHz, case (d) has a lower number of CBFs compared to (b) (Subdomain radius: D), however, the current errors are 9.65e$-$5 and 9.79e$-$7 respectively. The benefit of CBFM for both single domain and larger domain is more significant as the number of lower-order basis functions increases. In for cases (a) and (c), only up to secondary CBFs with a radius of influence of D is used, that is, at most 3 CBFs per subdomain. Cases (a) and (c) correspond to a subdomain radius of D and $2D$ respectively, and reasonable accuracy is obtained throughout the frequency range.

The increase in reduced matrix size for cases (d) and (e) from 300 MHz to 500 MHz would not have been the case if no CBFs were discarded during the SVD operation, since the number of CBFs generated is independent of the excitation frequency. The slow decay of the normalized singular values graph for single antenna subdomain in Figure 7.2 explains the variation in reduced matrix size across frequencies.

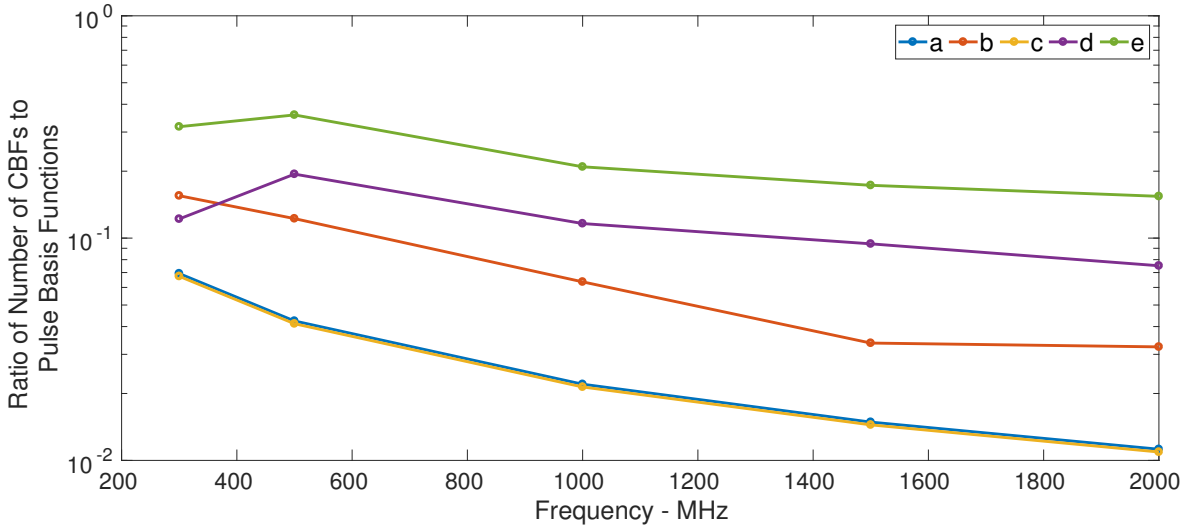

Figure 7.6: Ratio of number of CBFs to lower-order basis functions. Range of frequencies: 300 MHz to 2000 MHz. Inter-element space: 0.525

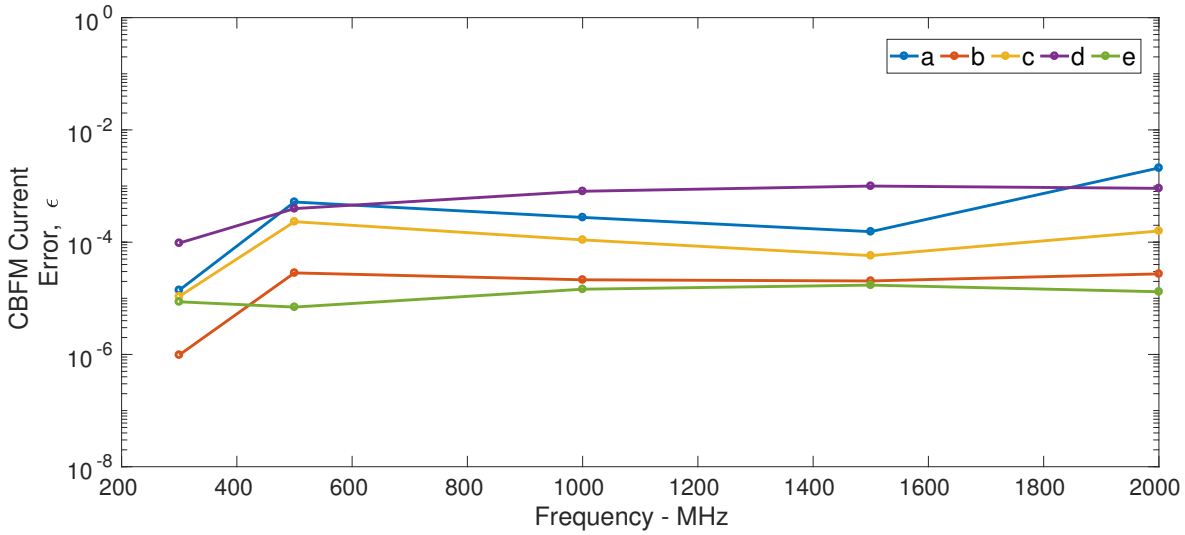

Figure 7.7: CBFM current error, ϵ. Range of frequencies: 300 MHz to 2000 MHz. Inter-element space: 0.525

7.4.2 Inter-Element Distance: 1.5

The inter-element distance is increased to 1.5, while all the parameters are unchanged. The results for compression in the number of basis functions are plotted in Figure 7.8 and the corresponding current errors are shown in Figure 7.9. A similar profile to that of Figure 7.6 is observed. However, as stated in Section 7.2, the difference in compression of impedance matrix achieved while using single antenna subdomain or larger subdomain decreases as the antenna array becomes more sparse.

The current error in both Figures 7.7 and 7.9 are bounded across frequencies, which makes CBFM even more attractive at high frequencies.

	Subdomain Radius	HO CBFs Structure	Radius of Influence	CBF Order
(a)	D	Distanced-based	D	Secondary
(b)	D	Distanced-based	$2D$	Tertiary
(c)	$2D$	Distanced-based	D	Secondary
(d)	0	Tree structure	$2D$	Tertiary
(e)	0	Tree structure	$3D$	Quaternary

Table 7.5: Parameters used for test cases (a) to (e)

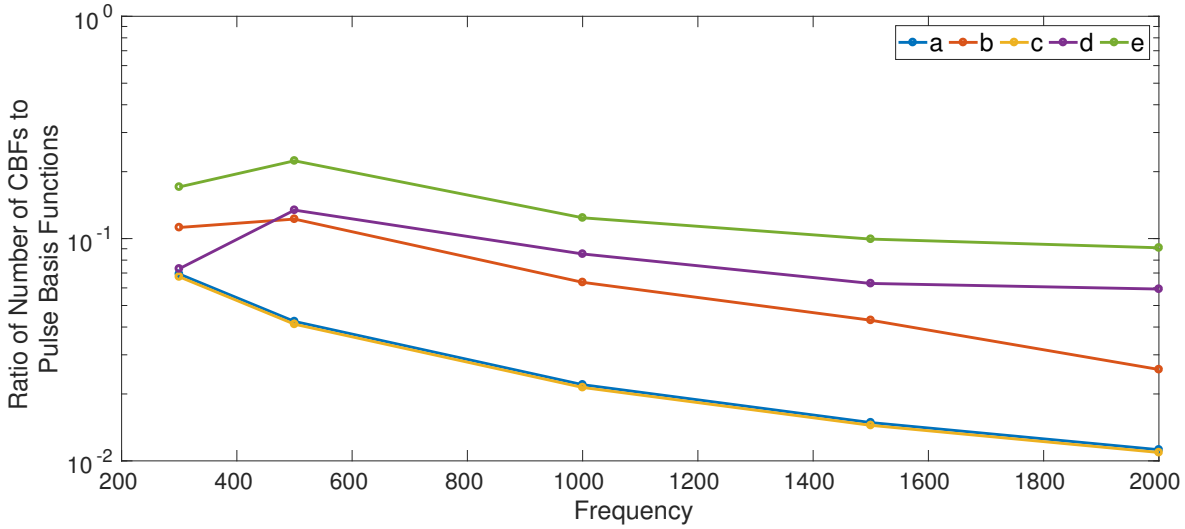

Figure 7.8: Ratio of number of CBFs to lower-order basis functions. Range of frequencies: 300 MHz to 2000 MHz. Inter-element space: 1.5

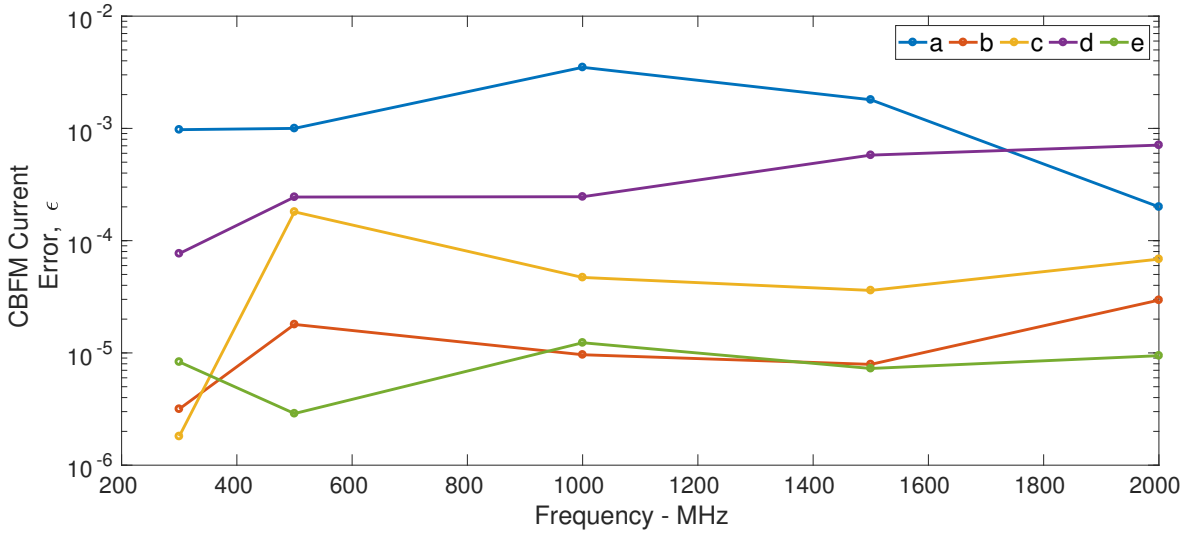

Figure 7.9: CBFM current error, ϵ. Range of frequencies: 300 MHz to 2000 MHz. Inter-element space: 1.5

7.5 Conclusion

In this chapter, larger subdomain CBFM with the distance-based criterion to generate higher-order CBFs has been compared to the conventional CBFM through 3 numerical tests. In the first numerical test, it is shown that highly accurate results can be obtained using an acceptable number of larger subdomain CBFs. If the same accuracy is required using single antenna subdomain, a small compression in the reduced matrix is achieved, thus making the solver unpractical. Moreover, for a sparse array, the use of larger subdomain CBFM is less significant since mutual coupling among elements is lower. Secondly, using a subdomain radius of D, a moderately accurate result is obtained using only 3 CBFs per subdomain. In the third numerical test, the excitation frequency is varied. It is shown that the importance of using larger subdomains increases with the frequency. That is, when the number of lower-order basis functions is large.

Chapter 8

Conclusion

8.1 General Conclusion

In this work, a CBFM solver has been implemented to solve for antenna array problems in the 2D, TM context. The aim is to reduce the number of degrees of freedom while maintaining a good accuracy. Larger overlapping CBF subdomains which span over multiple antenna elements have been proposed and implemented. To generate higher-order CBFs efficiently, a distance-based criterion has been used instead of the conventional tree structure. The motivation for using larger subdomains is that the effect of the mutual coupling among antenna elements is already captured in the primary CBF, thus leading to the inclusion of fewer secondary and higher-order CBFs to produce accurate results.

Firstly in this thesis, a MoM solver has been implemented in 2D, TM context after deriving the EFIE from first principles. The solution of the MoM solver has been compared to the commercial software FEKO and accurate results have been obtained for both a single antenna and an antenna array in the 2D context.

In the second stage, a CBFM solver has been implemented in Chapter 4, where a subdomain is considered to be an antenna element. The CBFM solver is compared to the MoM solution for accuracy. Up to quaternary CBFs have been used to solve for arrays with an inter-element distances of 0.525λ and 1.5λ. For the case of dense antenna array, a large number of CBFs is required to obtain a good accuracy. Fewer CBFs are used compared to the low-level basis function in MoM. To increase the accuracy of the CBFM solver, more degrees of freedom are required. That is, an increase in the order of CBFs, the radius of influence, or both.

The CBFM solver is extended in the third stage of this thesis to define larger overlapping subdomains, together with a distance-based criterion in Chapter 5 and 6 respectively. The number of primary subdomains is still equal to the number of antennas; thus every excitation configuration can be modeled. Procedures to generate secondary CBFs, to ensure the desired accuracy is obtained, have been discussed.

Finally, in Chapter 7, larger subdomain CBFM using distance-based criterion is compared to the conventional CBFM. It can be concluded that a smaller number of CBFs is required to provide the same accuracy when larger subdomain CBFM with the distance-based criterion is used. Numerical tests have been performed over a range of frequencies and varying inter-element distances in the array. The improvement in

compression is more significant for the case where mutual coupling is high, i.e., a dense antenna array, and also when a large number of lower-order basis functions are used, e.g., high-frequency or large arrays.

Even if the initial cost to generate larger subdomain CBFs is higher, CBFs are computed only once for the case of regular array and this cost does not increase with the size of the array. Since fewer degrees of freedom are used in larger subdomain CBFM, the solver becomes more attractive as the size of the antenna array increases, specially for cases where mutual coupling are high.

8.2 Future Work

- CBFM solver in 3D MoM using larger overlapping subdomains and a distance-based criterion to generate higher-order CBFs is to be implemented for connected, dense and sparse antenna array.
- CBFM solver needs to be extended to both regular and irregular planar antenna arrays in the 3D MoM context.
- Fast factorization techniques need to be investigated for larger subdomains and used to efficiently fill the reduced matrix entries.

Appendix A

Wave Equation

For radiation problems, an uncoupled differential equation, namely the **wave equation**, is often more practical than the coupled set of Maxwell's equation. The wave equation can be obtained using the Faraday's equation (2.1) and the Maxwell-Ampere's equation (2.2).

By taking the curl on both side of (2.1) and subsituting $\boldsymbol{H}$ by (2.2), we obtain

$$\nabla \times \nabla \times \boldsymbol{E} - w^2 \mu_0 \epsilon_0 \boldsymbol{E} = -jw\mu_0 \boldsymbol{J}. \tag{A.1}$$

Using the electric Gauss' law, $\nabla \cdot \boldsymbol{E} = \dfrac{q_e}{\epsilon_0}$, and the vector identity in (A.2),

$$\nabla \times \nabla \boldsymbol{E} = \nabla(\nabla \cdot \boldsymbol{E}) - \nabla^2 \boldsymbol{E}, \tag{A.2}$$

equation (A.1) can be simplified to

$$\nabla^2 \boldsymbol{E} + k^2 \boldsymbol{E} = jw\mu_0 \boldsymbol{J} + \frac{\nabla q_e}{\epsilon_0}. \tag{A.3}$$

The wave equation can then be obtained by substituting the continuity equation, $\nabla \cdot \boldsymbol{J} = -jwq_e$, in (A.3) as

$$\nabla^2 \boldsymbol{E} + k^2 \boldsymbol{E} = jw\mu_0 \boldsymbol{J} - \frac{1}{jw\epsilon_0} \nabla(\nabla \cdot \boldsymbol{J}). \tag{A.4}$$

The derivation of the EFIE using the wave equation is given in [6].

Appendix B

Other Explored Ideas

B.1 Characteristic Modes

Instead of using CBFs, the concept of using characteristic modes (eigenfunctions) [39] has also been briefly investigated during the course of this thesis. Characteristic modes are the eigenfunctions of the MoM impedance matrix and is formulated by the eigenvalue equation,

$$XJ_n = \lambda_n RJ_n, \tag{B.1}$$

where X and R are the real and imaginary parts of the MoM impedance matrix, such that $Z = R + jX$; λ_n is the eigenvalue and J_n is the corresponding eigenfunction.

The eigenvalue equation (B.1) has been solved using the *Harrington and Mautz's Method* [40], where the number of characteristic modes generated is controlled through the SVD operation of the real part of the impedance matrix, R [41]. After solving the eigenvalue equation for each subdomain, the characteristic modes are employed as MBFs. The advantage of using characteristic modes instead of CBFs as macro basis functions is that the former can be computed without prior knowledge of the excitation field. That is, the characteristic mode depends only on the geometry of the structure.

The reduced impedance matrix is computed similarly to as in (4.9), and the current coefficients are expanded as in (4.12).

The characteristic modes as MBFs have been applied to a scattering problem as shown in Figure B.1. The graphs of the real and imaginary part of the scattered field are shown in Figures B.2 and B.3 respectively, comparing characteristic modes as MBFs to the MoM. Accurate results can be obtained using characteristic modes. However, in this thesis the focus has been on using CBFM instead of characteristic modes. Firstly because slightly more MBFs were required compared to CBFs to obtain the same accuracy. Secondly, it is more straight-forward to extend single antenna subdomains to larger subdomains when using CBFs. The criterion to use for choosing the most important modes to include as MBFs still needs some further investigation.

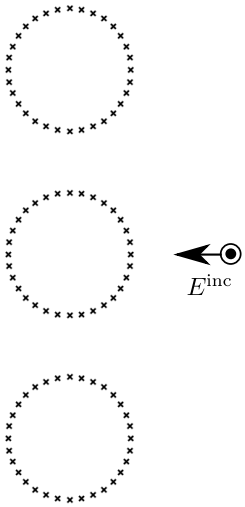

Figure B.1: Structure of problem to be solved.

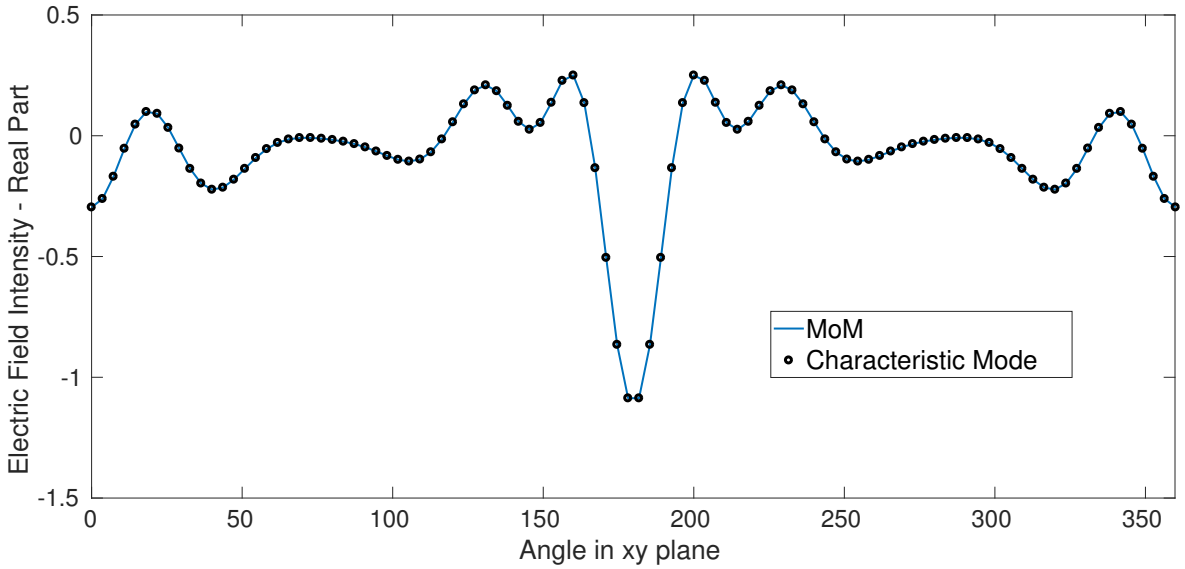

Figure B.2: Real part of scattered electric field.

B.2 Combining Primary and Secondary CBFs to Generate Tertiary CBFs

The primary and secondary CBFs for subdomain radius D have been added after zero padding is performed for each subdomain individually. The combined subdomain radiates as one unit to generate a tertiary CBF. This is possible for larger subdomain CBFM, since both CBFs have the same CBF coefficient if considered in an isolated scenario as shown in Figure B.4. The primary CBF of the first antenna element in an array is considered since a simpler derivation can be achieved because of a smaller size of the subdomain. The motivation of this section is to use even less CBFs per subdomain without any degradation in accuracy, as to be discussed below.

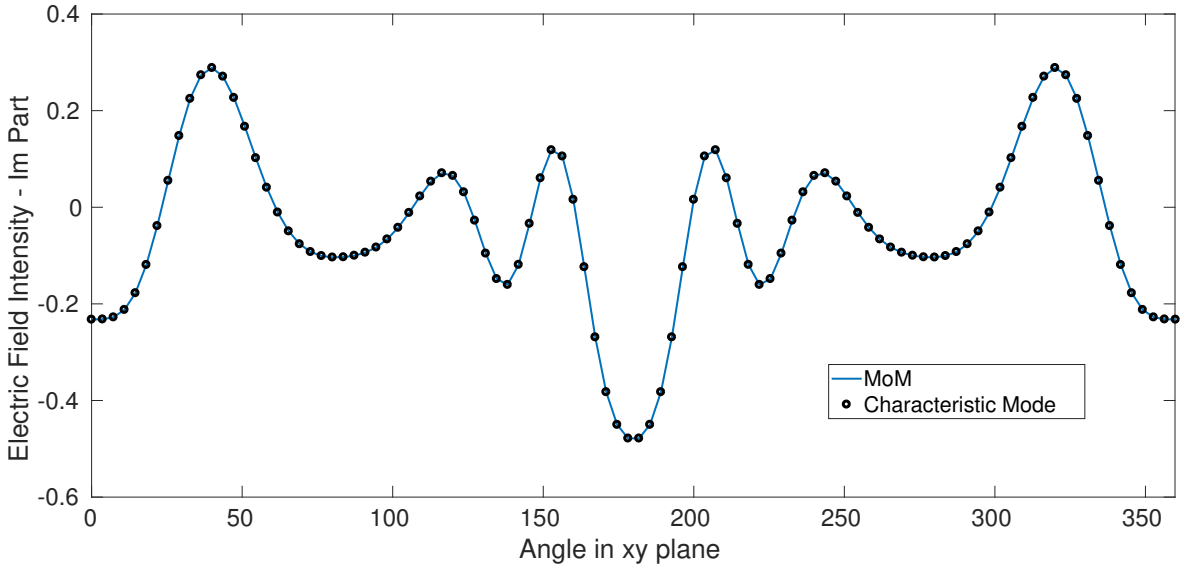

Figure B.3: Imaginary part of scattered electric field.

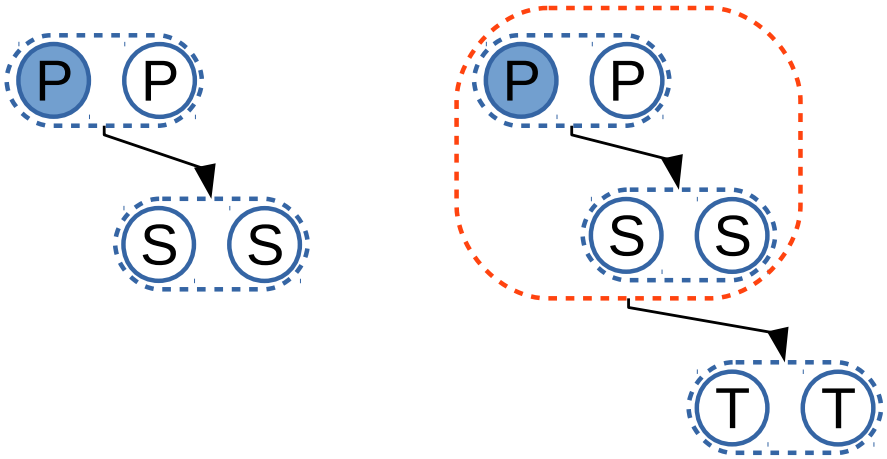

Figure B.4: Generation of a tertiary CBF from a combined primary-secondary CBF.

The reduced matrix equation for the interaction between the primary and secondary subdomain in Figure B.4 is given as

$$\begin{bmatrix} \langle {J_1}^H, Z_{aa} J_1 \rangle & \langle {J_1}^H, Z_{ab} J_2 \rangle \\ \langle {J_2}^H, Z_{ba} J_1 \rangle & \langle {J_2}^H, Z_{bb} J_2 \rangle \end{bmatrix} \begin{bmatrix} \alpha_1 \\ \alpha_2 \end{bmatrix} = \begin{bmatrix} \langle {J_1}^H, Z_{aa} J_1 \rangle \\ 0 \end{bmatrix}. \tag{B.2}$$

Z_{aa} and Z_{bb} represents the primary and secondary subdomains respectively. The CBF on the primary subdomain is denoted as J_1 and the one defined on the secondary subdomain is J_2, where α_1 and α_2 are the corresponding CBF coefficients respectively.

Following (B.2), equation (B.3) is obtained as

$$\langle {J_2}^H, \alpha_1 Z_{ba} J_1 \rangle + \langle {J_2}^H, \alpha_2 Z_{bb} J_2 \rangle = 0. \tag{B.3}$$

By expanding the inner product in (B.3), equation (B.4) is obtained as

$${J_2}^H (\alpha_1 Z_{ba} J_1) = {J_2}^H (-\alpha_2 Z_{bb} J_2). \tag{B.4}$$

Pre-multiplying (B.4) by the inverse of J_2^H gives

$$\alpha_1 Z_{ba} J_1 = -\alpha_2 Z_{bb} J_2. \tag{B.5}$$

By substituting $J_2 = -Z_{bb}^{-1} Z_{ba} J_1$ into (B.5) leads to

$$\alpha_1 Z_{ba} J_1 = \alpha_2 Z_{bb} Z_{bb}^{-1} Z_{ba} J_1, \tag{B.6}$$

and finally,

$$\alpha_1 = \alpha_2. \tag{B.7}$$

Thus, as mentioned at the beginning of this section, the two CBFs can be added since their CBF coefficients are equal.

An antenna array of 25 antenna elements where only the first antenna is active, is solved using the two cases for CBFs structures as presented in Figure B.5. A subdomain radius of D is used, however, this is not shown in Figure B.5 for visual simplicity.

The current results compared to MoM, and the current coefficient error graphs for both cases are shown in Figures B.6 and B.7. Very good accuracy and nearly identical results are obtained using both cases. This is true since adding the primary and secondary CBFs implies the superposition of the two individual radiated fields as discussed in Section 6.2.

Using the method in case (a) (Figure B.5), improves the efficiency of the solver by producing accurate results with a low number of CBFs per subdomain.

However, this method could not be proceeded any further in this thesis since a general procedure to generate CBFs in this fashion, up to any order or radius of influence could not be found.

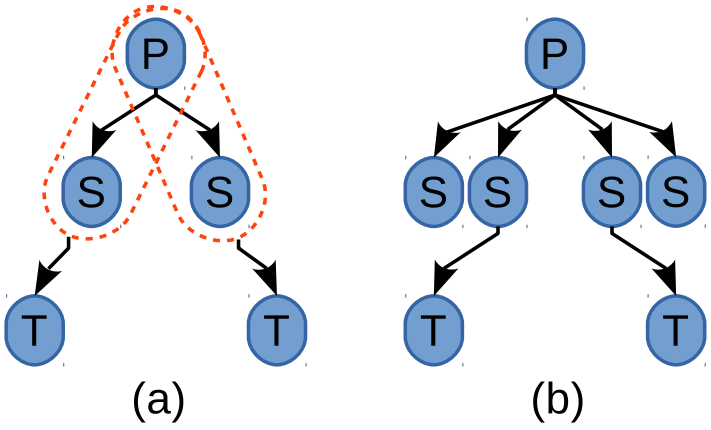

Figure B.5: Test cases for structure of CBFs to be compared in Figures B.6 and B.7.

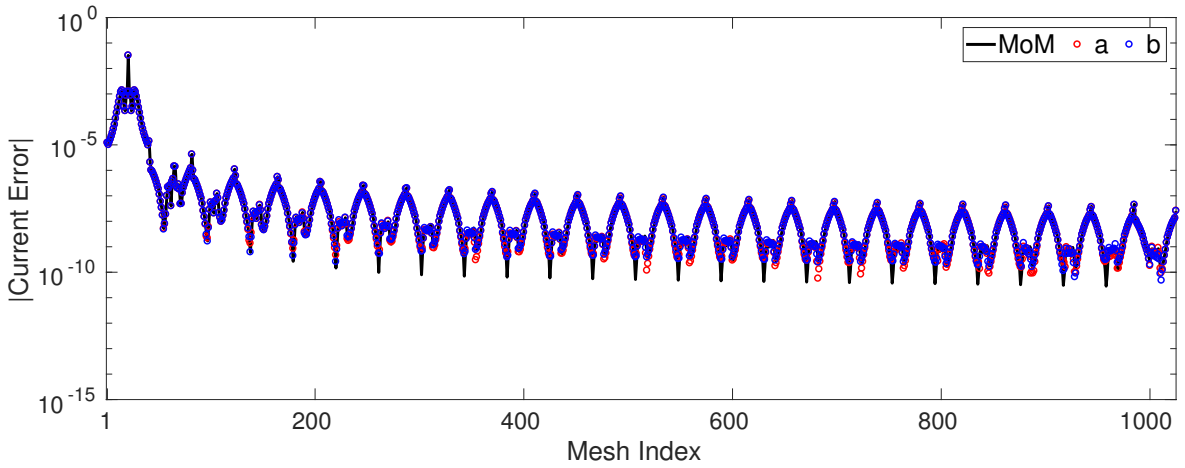

Figure B.6: Current coefficient of CBFM with cases (a) and (b) (from Figure B.5) compared to the full MoM.

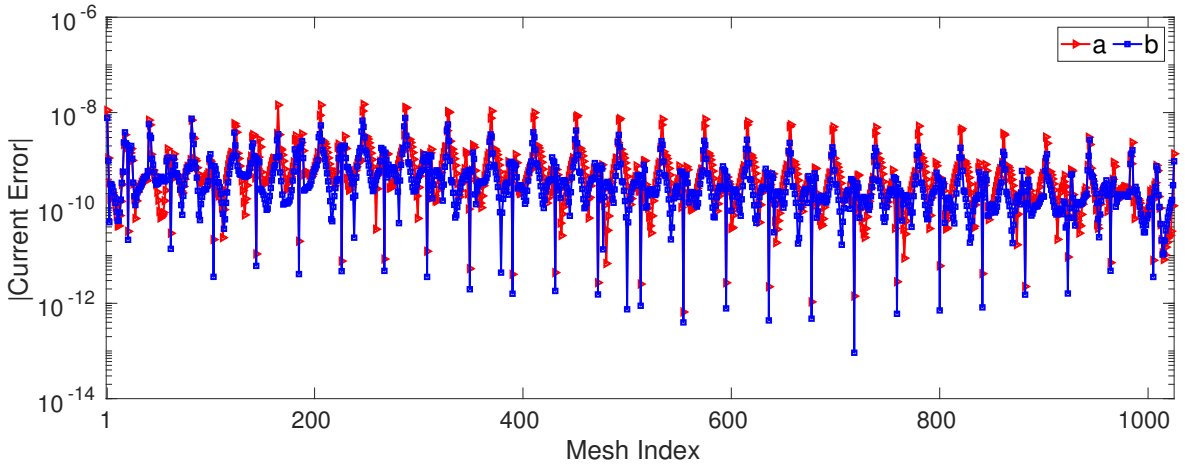

Figure B.7: Current coefficient errors of CBFM with cases (a) and (b) from Figure B.5.

List of References

[1] K. G. Jansky, "Electrical disturbances apparently of extraterrestrial origin," *Proceedings of the Institute of Radio Engineers*, vol. 21, no. 10, pp. 1387–1398, 1933.

[2] A. R. Thompson, J. M. Moran, and G. W. Swenson, "Interferometry and synthesis in radio astronomy," 2001.

[3] P. E. Dewdney, P. J. Hall, R. T. Schilizzi, and T. J. L. Lazio, "The Square Kilometre Array," *Proceedings of the IEEE*, vol. 97, no. 8, pp. 1482–1496, 2009.

[4] I. M. van Bemmel, A. van Ardenne, A. J. Faulkner, R. Morganti *et al.*, "Mid-frequency aperture arrays: the future of radio astronomy," *arXiv preprint arXiv:1208.6180*, 2012.

[5] R. F. Harrington and J. L. Harrington, *Field computation by moment methods*. Oxford University Press, 1996.

[6] W. C. Gibson, *The method of moments in electromagnetics*. CRC press, 2014.

[7] J.-M. Jin, *The finite element method in electromagnetics*. John Wiley & Sons, 2015.

[8] A. Taflove and S. C. Hagness, *Computational electrodynamics: the finite-difference time-domain method*. Artech house, 2005.

[9] E. Suter and J. R. Mosig, "A subdomain multilevel approach for the efficient MoM analysis of large planar antennas," *Microwave and Optical Technology Letters*, vol. 26, no. 4, pp. 270–277, 2000.

[10] V. Prakash and R. Mittra, "Characteristic basis function method: A new technique for efficient solution of method of moments matrix equations," *Microwave and Optical Technology Letters*, vol. 36, no. 2, pp. 95–100, 2003.

[11] H. Bui-Van, C. Craeye, and E. d. L. Acedo, "Main beam modeling for large irregular arrays: The SKA1-LOW telescope case," *arXiv preprint arXiv:1705.10084*, 2017.

[12] R. Maaskant, R. Mittra, and A. Tijhuis, "Multi-level characteristic basis function method (mlcbfm) for the anaylsis of large antenna arrays," *Radio Science Bulletin*, vol. 336, no. 3, pp. 23–34, 2011.

[13] E. FEKO, "Simulation software," 2015.

[14] C. A. Balanis, *Advanced engineering electromagnetics*. John Wiley & Sons, 1999.

[15] C.-T. Tai, *Dyadic Green functions in electromagnetic theory*. Institute of Electrical & Electronics Engineers (IEEE), 1994.

[16] P. J. Davis and P. Rabinowitz, *Methods of numerical integration*. Courier Corporation, 2007.

[17] M. R. Spiegel, *Schaum's outline of theory and problems of Fourier analysis: with applications to boundary value problems*. McGraw-Hill, 1974.

[18] E. R. Pike and P. C. Sabatier, *Scattering, Two-Volume Set: Scattering and inverse scattering in Pure and Applied Science*. Academic press, 2001.

[19] J.-M. Jin, *Theory and computation of electromagnetic fields*. John Wiley & Sons, 2011.

[20] M. M. Botha, "Study course: Mom 813 - The method of moments for electromagnetic analysis," *Stellenbosch University*, 2016.

[21] J. Song, C.-C. Lu, and W. C. Chew, "Multilevel fast multipole algorithm for electromagnetic scattering by large complex objects," *IEEE Transactions on Antennas and Propagation*, vol. 45, no. 10, pp. 1488–1493, 1997.

[22] R. Mittra and K. Du, "Characteristic basis function method for iteration-free solution of large method of moments problems," *Progress In Electromagnetics Research B*, vol. 6, pp. 307–336, 2008.

[23] L. Matekovits, V. A. Laza, and G. Vecchi, "Analysis of large complex structures with the synthetic-functions approach," *IEEE Transactions on Antennas and Propagation*, vol. 55, no. 9, pp. 2509–2521, 2007.

[24] D. J. Bekers, S. J. van Eijndhoven, and A. G. Tijhuis, "An eigencurrent approach for the analysis of finite antenna arrays," *IEEE Transactions on Antennas and Propagation*, vol. 57, no. 12, pp. 3772–3782, 2009.

[25] W. B. Lu, T. J. Cui, Z. G. Qian, X. X. Yin, and W. Hong, "Accurate analysis of large-scale periodic structures using an efficient sub-entire-domain basis function method," *IEEE transactions on antennas and propagation*, vol. 52, no. 11, pp. 3078–3085, 2004.

[26] R. Maaskant, R. Mittra, and A. Tijhuis, "Fast analysis of large antenna arrays using the characteristic basis function method and the adaptive cross approximation algorithm," *IEEE Transactions on Antennas and Propagation*, vol. 56, no. 11, pp. 3440–3451, 2008.

[27] S. Hay, J. O'Sullivan, and R. Mittra, "Analysis of connected patch arrays using the characteristic basis function method," in *Antennas and Propagation Society International Symposium, 2008. AP-S 2008. IEEE*. IEEE, 2008, pp. 1–4.

[28] D. J. Ludick, M. M. Botha, R. Maaskant, and D. B. Davidson, "The CBFM-enhanced jacobi method for efficient finite antenna array analysis," *IEEE Antennas and Wireless Propagation Letters*, vol. 16, pp. 2700–2703, 2017.

[29] C. Craeye, J. Laviada, R. Maaskant, and R. Mittra, "Macro basis function framework for solving Maxwell's equations in surface integral equation form," *The FERMAT Journal*, vol. 3, pp. 1–16, 2014.

[30] C. Delgado, M. F. Catedra, and R. Mittra, "Efficient multilevel approach for the generation of characteristic basis functions for large scatters," *IEEE Transactions on Antennas and Propagation*, vol. 56, pp. 2134–2137, 2008.

[31] J. Laviada, F. Las-Heras, M. R. Pino, and R. Mittra, "Solution of electrically large problems with multilevel characteristic basis functions," *IEEE Transactions on Antennas and Propagation*, vol. 57, no. 10, pp. 3189–3198, 2009.

[32] K. Sewraj and M. M. Botha, "Higher-order characteristic basis functions for antenna array analysis with the MoM in 2D," in *AFRICON, 2017 IEEE.* IEEE, 2017, pp. 625–629.

[33] S. G. Hay, J. D. O'Sullivan, and R. Mittra, "Connected patch array analysis using the characteristic basis function method," *IEEE Transactions on Antennas and Propagation*, vol. 59, no. 6, pp. 1828–1837, 2011.

[34] G. Bianconi, C. Pelletti, and R. Mittra, "A high-order characteristic basis function algorithm for an efficient analysis of printed microwave circuits and antennas etched on layered media," *IEEE Antennas and Wireless Propagation Letters*, vol. 12, pp. 543–446, 2013.

[35] G. H. Golub and C. Reinsch, "Singular value decomposition and least squares solutions," *Numerische mathematik*, vol. 14, no. 5, pp. 403–420, 1970.

[36] K. Sewraj and M. M. Botha, "Generalized characteristic basis function definitions for efficient antenna array analysis in 2D," in *Electromagnetics in Advanced Applications (ICEAA), 2017 International Conference on.* IEEE, 2017, pp. 984–987.

[37] T.-T. Lu and S.-H. Shiou, "Inverses of 2× 2 block matrices," *Computers & Mathematics with Applications*, vol. 43, no. 1-2, pp. 119–129, 2002.

[38] K. Zhao, M. N. Vouvakis, and J.-F. Lee, "The adaptive cross approximation algorithm for accelerated method of moments computations of EMC problems," *IEEE transactions on electromagnetic compatibility*, vol. 47, no. 4, pp. 763–773, 2005.

[39] R. Harrington and J. Mautz, "Theory of characteristic modes for conducting bodies," *IEEE Transactions on Antennas and Propagation*, vol. 19, no. 5, pp. 622–628, 1971.

[40] ——, "Computation of characteristic modes for conducting bodies," *IEEE Transactions on Antennas and Propagation*, vol. 19, no. 5, pp. 629–639, 1971.

[41] Y. Chen and C.-F. Wang, *Characteristic modes: Theory and applications in antenna engineering.* John Wiley & Sons, 2015.